ABSTRACT

Title of Dissertation: ON-CHIP PHOTONIC CIRCUITS FOR ATOM-LIGHT INTERACTION IN QUANTUM INFORMATION AND INTEGRATED OPTICAL SPECTROMETER FOR ASTROPHOTONICS

Yang Meng, Doctor of Philosophy, 2017

Dissertation directed by: Professor, Mario Dagenais,

Department of Electrical & Computer Engineering

Photonic circuits are becoming very promising in various applications. Here we propose two on-chip photonic circuits: one is for atom-light interaction in quantum information, and the other is for an optical spectrometer in astronomy.

Part I

In our work, we propose a nanowaveguide platform for collective atom-light interaction through the evanescent optical field coupling. We have demonstrated a centimeter-long silicon nitride nanowaveguide that has a sub-micrometer mode area and high fiber-to-waveguide coupling efficiencies for near-infrared wavelengths, working as evanescent field atom trapping/probing of an ensemble of ^{87}Rb atoms. Inverse tapers are

made at both ends of the waveguide that adiabatically transfer the weakly guided fiber-coupled mode to a strongly guided mode with an evanescent field for a better fiber-waveguide coupling efficiency. The coupling efficiency improves from around 2% to around 80% for both wavelengths. Trapping atoms by nanowaveguide modes is challenging because the small mode area generates high heat flux at the waveguide in an ultra-high vacuum. This platform has good thermal conductance and could transfer high enough optical powers to trap atoms in an ultra-high vacuum compared to a standalone photonic crystal waveguide with no substrate or an evanescent field coupled with a nanofiber. We have experimentally measured the optical absorption of thermal ^{87}Rb atoms through the guided waveguide mode. We have also demonstrated an atom-chip mirror MOT with the same dimension of the platform that can be transferred to the proximity of the surface by magnetic field controls.

Part II

We present an echelle grating which is based on an on-chip spectrometer that covers the near infrared wavelength range from 1.45um to 1.7um, and we use optical waveguides as the input and output channels. We have successfully achieved a reliable fabrication process to make the on-chip echelle-grating spectrometer. We have also achieved high fiber-waveguide coupling efficiency (94% per facet at 1550nm) and low propagation loss (-0.975dB/cm at 1550nm) for the input and output waveguides. In addition, we have characterized the bending loss of the waveguide. Finally, we have successfully measured the output spectrum of the echelle grating we designed and found it to be in good agreement with our simulation.

On-Chip Photonic Circuits for Atom-Light Interaction in Quantum Information and Integrated Optical Spectrometer for Astrophotonics

By

Yang Meng

Dissertation submitted to the Faculty of the Graduate School of the University of Maryland, College Park, in partial fulfillment of the requirements for the degree of

Doctor of Philosophy

2017

Advisory Committee:
Professor Mario Dagenais, Chair
Professor Sylvain Veilleux
Professor Christopher C. Davis
Professor Martin Peckerar
Professor Miao Yu

Preface

This dissertation is submitted for the degree of Doctor of Philosophy at University of Maryland, College Park. The research described in this dissertation was conducted under the supervision of Professor Mario Dagenais in the Department of Electrical and Computer Engineering, University of Maryland, College Park, between September 2011 and May 2017.

The work described in the first part of this dissertation, nano-optical waveguide for light-atom interaction, was funded by the ARO Atomtronics MURI project. This project is in collaboration with Dr. Jongmin Lee and Professor Steve Rolston from Department of Physics and Joint Quantum Institution (JQI) at the University of Maryland, College Park. In this work, we demonstrated an on-chip nanowaveguide platform for collective atom-light interaction through the optical evanescent field coupling, which can be potentially used in applications such as quantum computing and communication, and atomic sensors.

The work described in the second part of the dissertation, is an echelle-grating spectrometer for use in the near infrared wavelength range for astrophotonics. This is funded by a KECK Foundation grant. This project is in collaboration with Professor Sylvain Veilleux from Department of Astronomy and Joint Space-Science Institute in University of Maryland, College Park. In this work, we designed, fabricated and demonstrated an on-chip echelle-grating spectrometer that will be potentially used for astronomical spectra analysis in the near infrared wavelength range.

Part of the work in the Part I has been presented in the following publications:

[1] **Y. Meng,** J. Lee, M. Dagenais, S. L. Rolston, "A nanowaveguide platform for collective atom-light interaction." Appl. Phys. Lett. 107, 091110 (2015)

[2] J. Lee, **Y. Meng**, D. H. Park, M. Dagenais, and S. L. Rolston, "A nanophotonic atom trap toward collective atom-light interactions and the design of a novel protection layer for superconducting circuits toward a hybrid quantum system", *DAMOP14 Meeting of The American Physical Society,* (June 2-6 2014)

For the work described in the Part II, we are currently preparing a paper for publication of our recent results.

Yang Meng

May 2017

Dedication

To my parents,

Li-Min Meng and Guo-Fen Zhao

Acknowledgements

First of all, I would like to thank my father, Limin Meng, and my mother, Guofen Zhao, for their everlasting love and support. They always encourage and support me to pursue my dreams.

I would like to express my greatest gratitude to my academic and research advisor, Professor Mario Dagenais, for his constant guidance, motivation and support during the last 6 years, without which I would not have achieved my goals. He is very kind and knowledgeable. It is my great pleasure working with him and I learned a lot from him. I would also like to thank Professor Sylvain Veilleux for his great support and bringing me into a new world of astrophotonics that I am very interested in.

I would like to express my sincere appreciation to the other members of my dissertation committee, Professor Christopher C. Davis, Professor Martin Peckerar and Professor Miao Yu, for their time, effort and suggestions.

I would like to thank Dr. Jongmin Lee, who is not only a good collaborator in research but also a great friend in life.

I also wish to express my thanks to Tom Loughran, Mark Lecates, John Abrahams, Jonathan A. Hummel and Jim O'Connor who are the staffs of the Fablab where I spent most of my time during research. They are very kind and helpful.

Finally, I would like to thank my wife Dr. Tian Li. Thanks for loving and supporting me all the time.

Table of Contents

List of Abbreviations

AWG	Arrayed Waveguide Grating
BOE	Buffered Oxide Etch
CCD	Charge – Coupled Device
EBL	Electron Beam Lithography
ELT	Extremely Large Telescope
FBMS	Fixed Beam Moving Stage
FP	Fabry – Perot
FSR	Free Spectral Range
FWHM	Full Width at Half Maximum
ICP	Inductively Coupled Plasma
IR	Infrared
LPCVD	Low Pressure Chemical Vapor Deposition
MMF	Multi – Mode fiber
MOT	Magneto – Optical Trap
NA	Numerical Aperture
OPD	Optical Path Difference
PCF	Photonic Crystal Fiber
PECVD	Plasma Enhanced Chemical Vapor Deposition
PM	Polarization Maintaining
SEM	Scanning Electron Microscope
SMF	Single – Mode Fiber
ULI	Ultrafast Laser Inscription
UV	Ultraviolet

List of Figures

Part I

Nano-Optical Waveguide for Light-Atom Interaction

Chapter 1 : Background and Introduction

Atom-light interactions can be harnessed for a number of quantum-based applications, such as quantum information processing[1-4] and atomic sensing[5]. Enhancing the atom-light interaction with small mode areas has been demonstrated in several platforms such as hollow-core fibers[6, 7], hollow-core waveguides[8, 9], tapered fibers[10, 11] and a nanowaveguide[12]. An array of a few micrometer-square free-space optical spots in a trench from an optical waveguide array were also recently used to interrogate ultra-cold atoms formed by a mirror magneto-optical trap (MOT) above the trench[13]. In contrast to thermal alkali vapors[6-12] or a free-space mode from an optical waveguide array[13], laser-cooled ultra-cold atoms trapped in the evanescent field of a waveguide can exhibit much stronger coupling between the atoms and photons due to good overlap of the atoms with the small optical mode, and the lack of Doppler broadening. In addition, cold trapped atoms have a longer residence time in the field and thus a longer coherence time. All-optical switching with optically trapped atoms has previously been implemented in a hollow fiber[14], and nano-fiber based optical lattices for ^{133}Cs and ^{87}Rb atoms were also demonstrated[15, 16.] Although nanofiber atom traps create strong atom-light interactions, they are not easily scalable to realize complex photonic circuits, while an integrated optics approach with waveguides enjoys both strong interactions and the potential for scalability.

Here we present a potentially scalable nanowaveguide platform, which can operate as the atom-light interface between an evanescent field probe and cold neutral atoms. An open-window in the middle of the waveguide is used to trap and probe atoms through the evanescent field. Atoms loaded from an atom-chip mirror MOT will be optically trapped

with a two-color evanescent field atom trap provided by a red-detuned counter-propagating guided field and a blue-detuned traveling guided field acting together with van der Waals potential from the surface.

Instead of using a nanofiber[15, 16] or a nano-photonic crystal waveguide[17, 18], we consider an integrated design of a nanowaveguide and an atom chip mirror MOT. Compared to the fragile nanofiber and the nano-photonic crystal waveguide, our design is an on-chip design and includes the substrate. Therefore, our design is more robust and has better heat dissipation and scalability. In order to achieve this, we designed a waveguide with inversed tapers at both ends which offers high fiber-to-waveguide coupling efficiency (around 80%) for the three wavelengths. These three wavelengths are used for trapping (blue-detuned 760nm and red detuned 1064nm) and probing (780nm) the ^{87}Rb atoms. We also designed a gold mirror MOT to address the MOT atoms right near the waveguide. A packaging technique is also achieved to make the whole platform as an atomic cell. Currently, we have detected the photon-atom interaction by measuring the absorption of thermal Rb atoms through the nanowaveguide evanescent field.

Chapter 2 : Simulation, Design and Theoretical Calculation

2.1 Waveguide Mode Simulation

The optical waveguide is designed for efficient atom trapping with low insertion and propagation loss at both trapping wavelengths (760nm and 1064nm for ^{87}Rb) and probing wavelength (780nm for ^{87}Rb). Also, in order to achieve small mode size but a reasonable large evanescent field area, Si_3N_4 waveguides on SiO_2 on Si substrate are selected, as compared to using Si or GaAs waveguides.

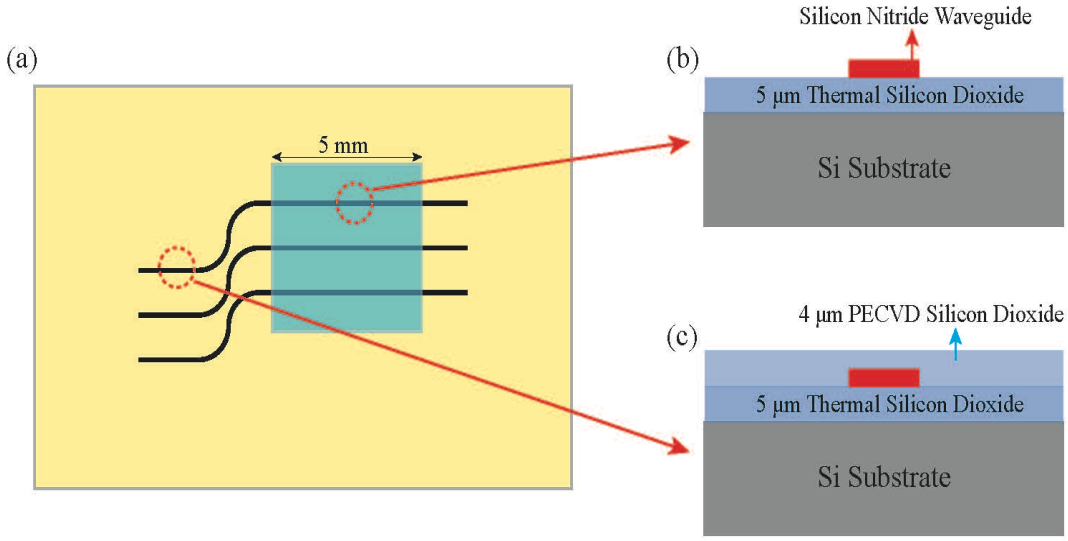

Figure 2-1: (a) schematic top view of the photonic chip we designed, (b) schematic cross-section view of the yellow area, (c) schematic cross-section view of the blue area

The waveguide is constructed with a silicon nitride core (Si_3N_4, n_{core}=2) and a silicon oxide substrate (SiO_2, n_{sub}=1.46). Fig. 2-1 (a) is the top view of the on-chip Si_3N_4 nanowaveguide. The waveguide is 13mm in length, and the bending radius for both

quarter circles is 1mm. The yellow area is covered with 4μm PECVD (Plasma Enhanced Chemical Vapor Deposition) SiO_2, and the blue area is open to air as the trapping area.

Fig. 2-1 (b) shows the cross section of the nanowaveguide in the open-window area. The substrate is 500μm p-type {100} single crystal silicon on which 5μm thermal silicon dioxide is deposited. This thick oxide layer not only works as the waveguide cladding but also prevents the optical waveguide mode from leaking into the Si substrate underneath. In addition, the thermal silicon dioxide layer offers better chemical stability in the subsequent fabrication steps compared to PECVD silicon dioxide or other types of deposited oxide films. The nanowaveguide is made by PECVD or LPCVD (Low Pressure Chemical Vapor Deposition) Si_3N_4, which is 800nm in width and 300nm in thickness. Fig. 2-1 (c) shows the cross section of the nanowaveguide in the yellow area, the only difference from the open-window area is that the nanowaveguides are covered with another layer of 4μm-thick PECVD SiO_2. This additional SiO_2 layer is used to create a symmetric cladding to the Si_3N_4 waveguide core which will lead to better coupling efficiency. It can also protect the nanowaveguide from being damaged during cleaving and coupling. When the waveguide is made by PECVD Si_3N_4, the open window is made by using a shadow mask through which the PECVD SiO_2 is deposited. However, since the LPCVD Si_3N_4 has an extremely low etching rate in BOE compared to PECVD SiO_2, we first deposit a plain layer of PECVD SiO_2 and then pattern it by photolithography for BOE etching.

In order to achieve a large optical depth, a small mode area with a comparatively large optical evanescent field is desired. Besides, since our waveguide chip has both SiO_2

covered and uncovered areas (which are shown as the yellow and blue areas in Fig. 1), the mode mismatching between these two areas needs to be designed as small as possible.

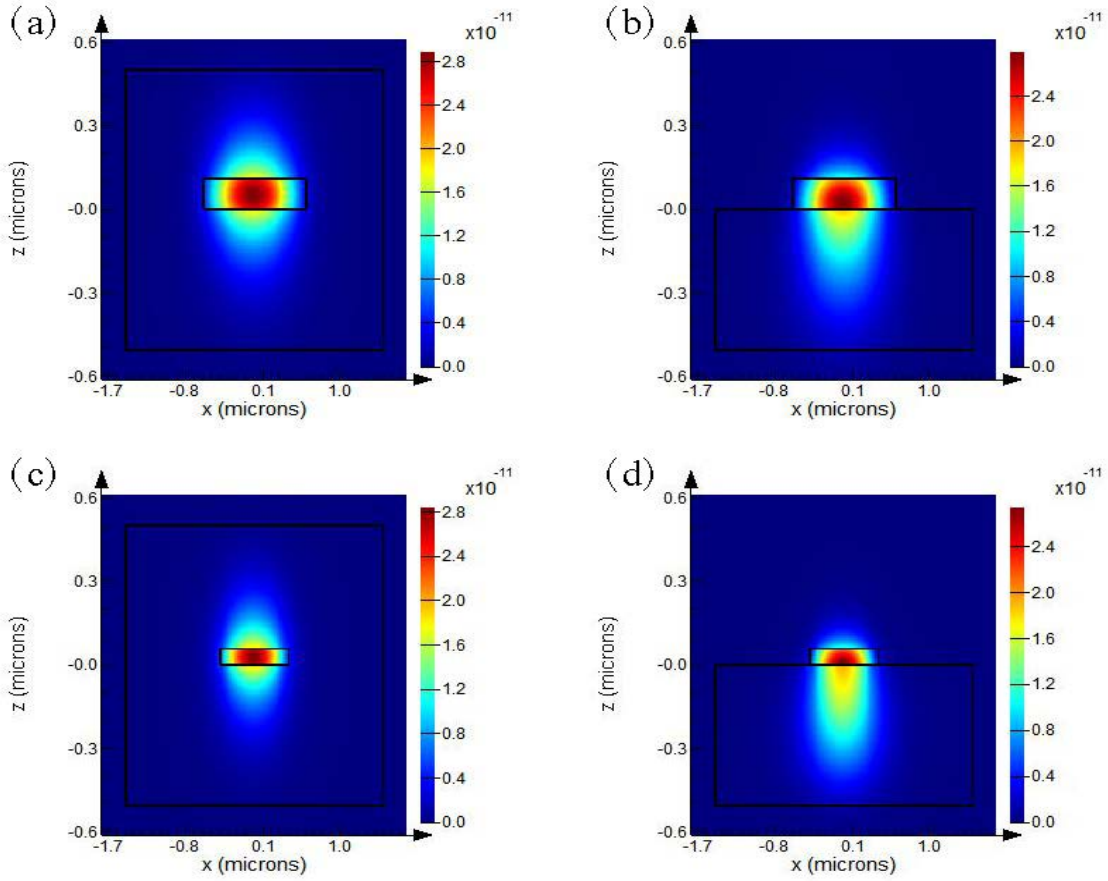

Figure 2-2: weakly guided mode of waveguide with symmetric cladding at 1064nm wavelength (a) and 760nm wavelength (c), weakly guided mode of waveguide without a upper cladding at 1064nm wavelength (b) and 760nm wavelength (d)

Fig. 2-2 (a) shows the TE mode for a typical weakly guided mode at 1064nm wavelength. The waveguide core is Si_3N_4 and it has a symmetric SiO_2 cladding. The waveguide is 1.2μm in width and 110nm in thickness. It has a single TE mode, and its evanescent field carries 71% of its power. This kind of weakly guided mode is usually used for high fiber-waveguide coupling efficiency since it offers much larger mode size

than its physical size. Fig. 2-2 (b) shows this TE mode when there is no SiO_2 covered on the top.

Similarly, Fig. 2-2 (c) and (d) shows the weakly guided mode at 760nm wavelength. When there is a symmetric cladding, the evanescent field takes 82.9% of its power. However, when it goes to the open-window area, the evanescent field in the air will suddenly drops down to 0.56%. As shown in the image, the mode has largely moved towards the SiO_2 because the cladding is no longer symmetric and the SiO_2 underneath has a larger refractive index compared to the air on the top. This will dramatically reduce the optical depth and also introduce a great optical loss due to the large mode mismatch. Therefore, a strongly confined mode is needed in our case rather than a weakly guided mode.

The mode size of a commercial single mode fiber is usually several micrometers in radius, while the mode size for our nanowaveguide is only several hundred nanometers. Considering the mode match between an optical fiber and our nanowaveguide, having the waveguide mode to be as small as possible is not necessarily better. By careful simulation, we finally choose our nanowaveguide structure as 800nm in width and 300nm in thickness. This waveguide is single TE mode for 1064nm wavelength, and not only offers a reasonably large mode size but also a good optical depth.

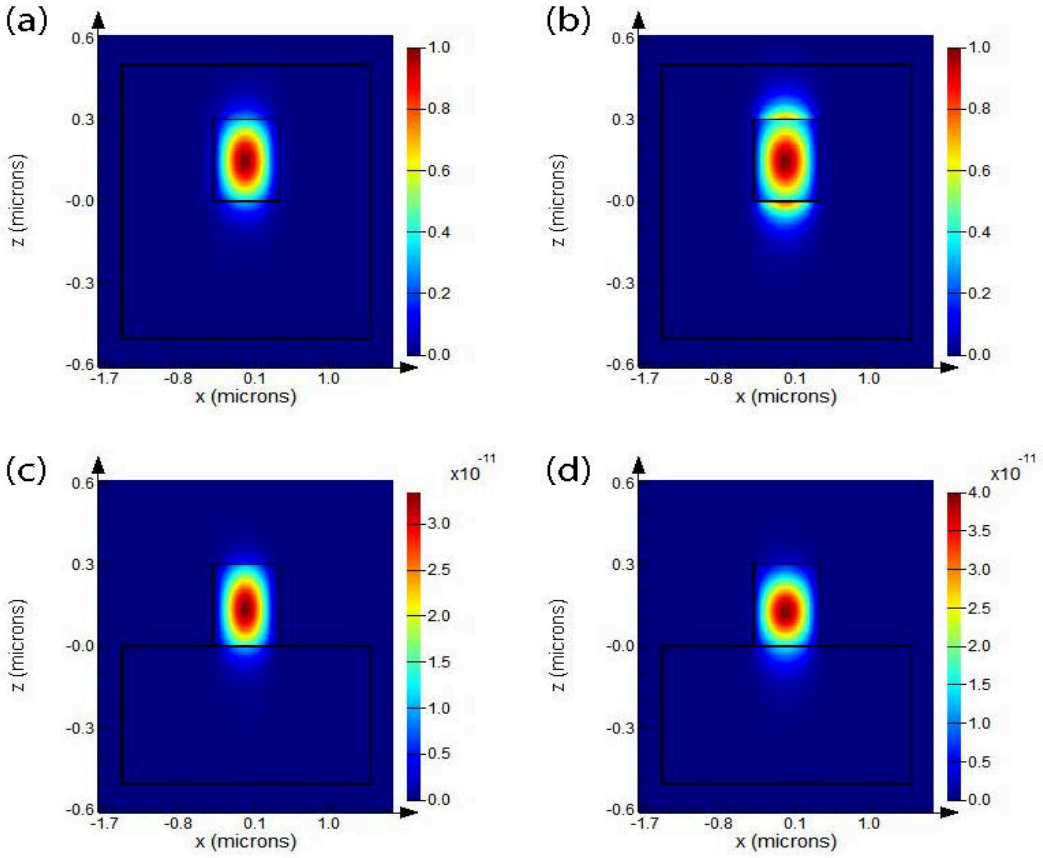

Figure 2-3: TE mode (a) and TM mode (b) of the designed waveguide with symmetric cladding at 760nm wavelength, TE mode (c) and TM mode (d) of the designed waveguide without a upper cladding at 760nm wavelength

Fig. 2-3 (a) and (b) are the TE and TM mode for this nanowaveguide at 760nm wavelength when the waveguide is covered with 4μm SiO_2, while Fig. 2-3 (c) and (d) are these TE and TM modes at the open-window area. As we can see in the images, the two TE modes are almost exactly the same. The mode matching between these two modes are more than 95% in power according to the equation:

$$\eta_{12} = \frac{\left|\iint E_1(x,y) \cdot E_2^*(x,y)\, dx\, dy\right|^2}{\iint |E_1(x,y)|^2 dx\, dy \cdot \iint |E_2(x,y)|^2 dx\, dy} \quad (1)$$

where the η_{12} means mode matching ratio or coupling efficiency between mode1 and mode2, and the E(x,y) describes the electric field for each mode. As shown in Fig. 2-3 (b), the TM mode has a discontinuity at the waveguide surface along the z direction. However, a continuous potential is needed for trapping, so we only consider the TE mode and we will eliminate the TM mode by polarization control during the experiment.

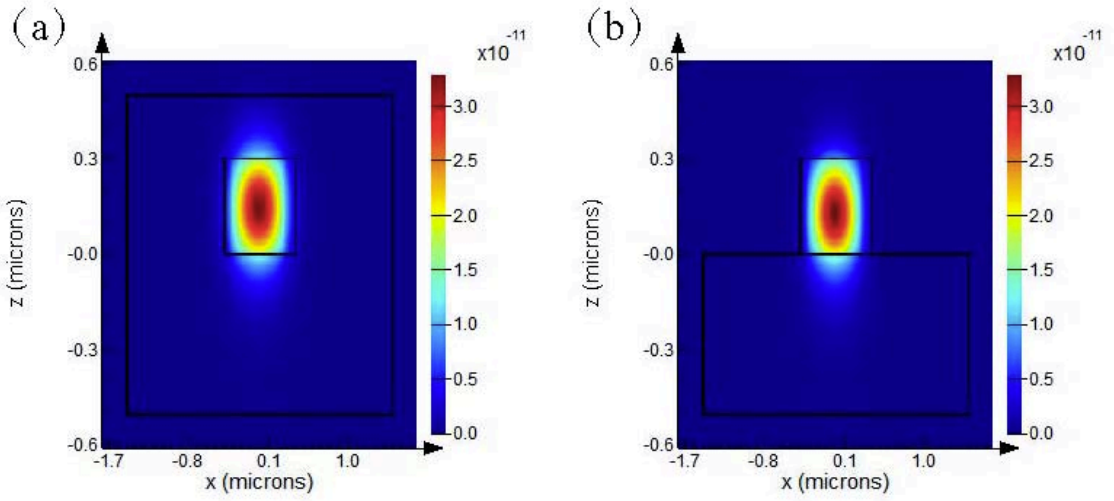

Figure 2-4: (a) TE mode of this designed waveguide with a symmetric cladding at 1064nm wavelength, (b) TE mode of this designed waveguide without the upper cladding at 1064nm wavelength

Similarly, Fig. 2-4 (a) and (b) shows the TE modes for 760nm wavelength at the SiO_2-covered and open-window areas. As a result, these two TE modes also have very high mode matching ratio. Therefore, we use this 800nm wide and 300nm thick Si_3N_4 as our waveguide.

2.2 Inversed Taper Simulation

According to waveguide mode simulation, the TE mode size at 760nm wavelength is 703nm in x direction and 377nm in z direction; and the TE mode size at 1064nm is 765nm in x direction and 474nm in z direction (full width at $1/e^2$ of power). We use

Fibercore SM750 (core diameter = 3.82 μm, cladding diameter = 125μm, NA = 0.14) fiber, with mode-field diameters of 4.32 μm at 760nm (n_{core} = 1.46077, n_{clad} = 1.45405) and 5.4 μm at 1064nm (n_{core} = 1.45635, n_{clad} = 1.44963). Fig. 2-5 shows the TE like modes for this SM750 single-mode fiber at 760nm and 1064nm wavelengths.

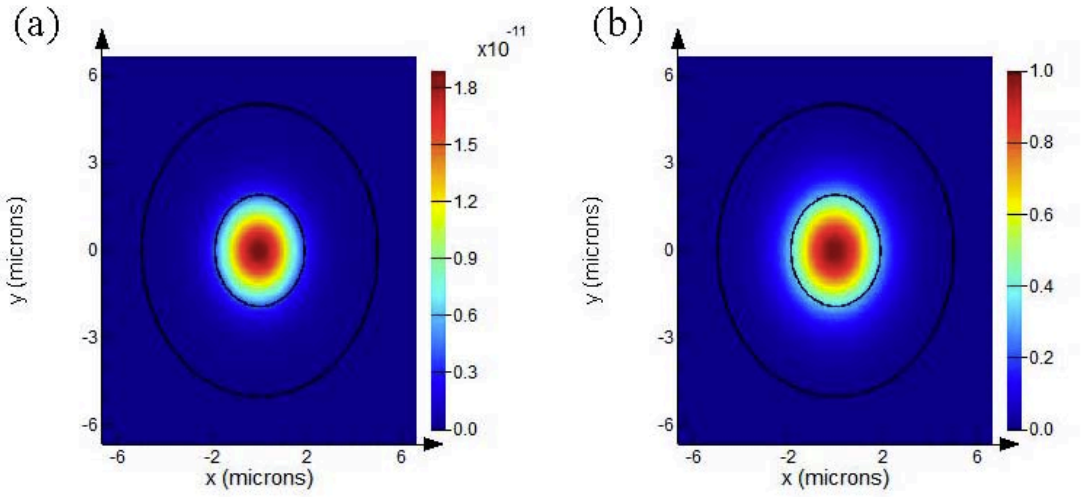

Figure 2-5: TE (a) and TM (b) like modes of SM750 fiber

If we treat these modes as Gaussian modes, then the TE nanowaveguide mode at 760nm can be represented as $E_{wg\_760} = A_1 \exp\left(-\left(\frac{x^2}{2*0.351^2} + \frac{y^2}{2*0.188^2}\right)\right)$, the nanowaveguide mode at 1064nm can be represented as $E_{wg\_1064} = A_2 \exp\left(-\left(\frac{x^2}{2*0.382^2} + \frac{y^2}{2*0.237^2}\right)\right)$, the fiber mode at 760nm can be represented as $E_{fb\_760} = A_3 \exp\left(-\left(\frac{x^2+y^2}{2*2.16^2}\right)\right)$, and the fiber mode at 1064nm can be represented as $E_{fb\_1064} = A_4 \exp\left(-\left(\frac{x^2+y^2}{2*2.7^2}\right)\right)$. By substituting these equations back into equation 1, we can numerically calculate the coupling efficiency between the fiber and the nanowaveguide which is 5.3% at 760nm and 4.8% at 1064nm. And experimentally we measured a coupling efficiency about 1% ~ 2%. Since the atom trapping needs at least tens of milliwatts of the laser power and our

laser setup only has a power around 130 milliwatts, this coupling efficiency is far from enough. Therefore, we need to find a way to increase the coupling efficiency.

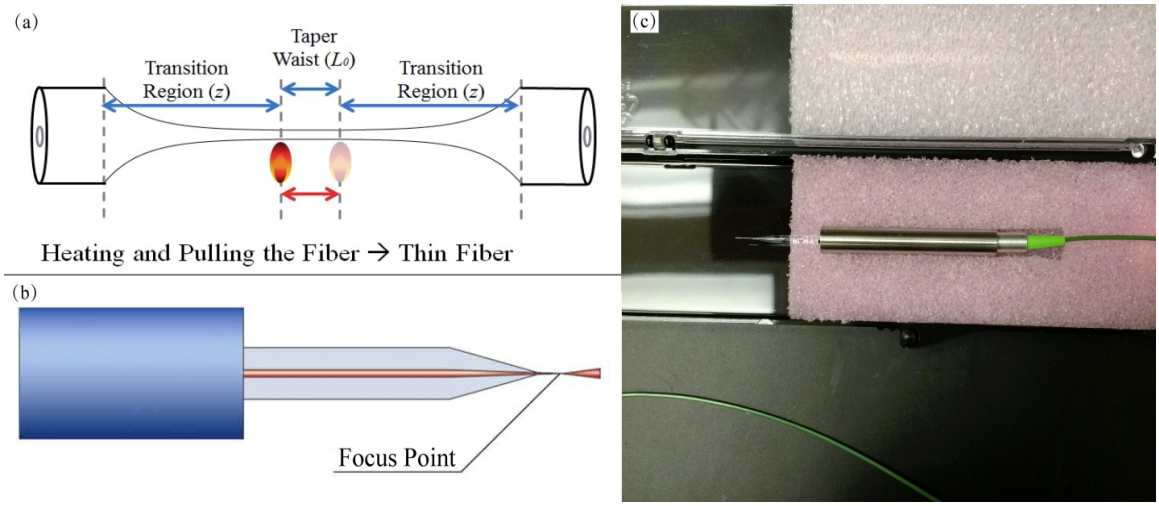

Figure 2-6: (a) schematic of a tapered fiber, (b) schematic of a lensed fiber, (c) image of our lensed fiber

There are various ways to increase the coupling efficiency between a comparatively large optical fiber mode and a small nanowaveguide mode. Some of the common methods are using a lensed fiber, tapered fiber, or using a tapered waveguide for the mode matching. Our goal is to achieve a reliable high coupling efficiency between a fiber and a waveguide, and to fix the fiber to the chip, i.e. using glue, to make a portable atomic cell.

Fig. 2-6 (a) shows the schematic image of a common tapered fiber. The basic idea to make a tapered fiber is to gradually reduce the physical size of the fiber core and cladding and then reduce the fiber mode size. To achieve this, people usually first remove the buffer jacket of the fiber and heat the core and cladding to make them soft, and then pull the fiber to make it thinner. As shown in Fig. 2-6 (a), a cleaving will be made at the taper waist position to create the tapered fiber facet. This method can achieve a small

mode size from several micrometers to several hundred nanometers. However, the tapered fibers are usually too fragile due to their very thin sizes, which makes it unreliable for fiber-waveguide coupling.

Fig. 2-6 (b) and (c) are the images for a lensed fiber. Unlike the tapered fiber, the lensed fiber has an embedded lens at the fiber tip to focus the light to a smaller mode size. According to our requirement, there are mainly two disadvantages of lensed fibers. First, since it has an embedded lens inside, the size of the lensed fiber is usually much larger than a normal fiber which is too bulky to use with the atomic cell. Fig. 2-6 (c) shows the real size of a commercial lensed fiber, the tip is small but the major part of the fiber is 6.4mm in diameter. Second, as shown in Fig. 2-6 (b), the focus point of the lensed fiber is located at a distance from the fiber tip. In order to achieve the best coupling efficiency, the waveguide facet (waveguide edge) should be exactly at this focused point. In this way, we cannot glue the fiber to the waveguide chip since the best coupling efficiency does not happen at the end of the fiber tip. Considering these disadvantages of the tapered fiber and lensed fiber, we chose to design an inversed taper at the end of the waveguide to improve the coupling efficiency.

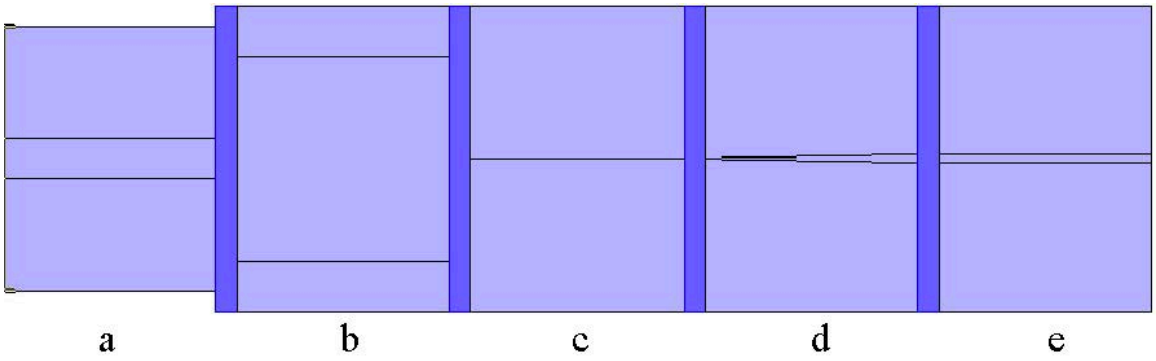

Figure 2-7: Simulation structure in FimmProp

Inversed tapers with optical waveguide have been widely used as an optical mode converter to increase the coupling efficiency. The basic idea of the inversed tapers is to gradually change a weakly guided mode at the taper end to a stronger guided mode in the largest part of the waveguide. Since the weakly guided mode usually has a large mode size, it can offer a much better mode match to the optical fiber mode then leading to a better coupling efficiency. Some previous work have demonstrated good performance of this kind of inversed tapers at telecom wavelengths [19], but its advantages and applicability have seldom been reported at near-infrared wavelengths in situations where many wavelengths are used between 750nm and 1100 nm, which is the typical situation used in atomic physics and in nonlinear optics. And our goal is to design an inversed taper that can achieve high fiber-waveguide coupling efficiency for this wide near-infrared wavelength range, since our focused wavelengths are 760nm, 780nm and 1064nm.

One of the advantages of this kind of inversed tapers is the taper part and waveguide part can be designed separately. In this way, we can maintain the waveguide design discussed in the previous section, and only focus on designing a low loss and good mode-matching inversed taper. In order to do this, we are using the software, FimmProp from Photon Design, to simulate the inversed taper structure. Fig. 2-7 shows the simulated structure. From left to right, it contains five parts: “a” is the optical fiber part; “b” is a 1μm long empty space with the refractive index of the glue we are using to simulate the coupling efficiency after gluing; “c” is a thin rectangle waveguide which has the same width as the taper end, this part is used to make up for the cleaving inaccuracy; “d” is the inversed taper and taper ends at the left side; “e” is the majority part of the

optical waveguide we discussed in the last section. The “c”, “d” and “e” part has the same thickness which is 300nm, and the light is from the left so this is the input part. Since the waveguide has a symmetrical structure and we are using the same fiber at the input and output, so the coupling efficiency should be the same at both ends. Therefore, we only simulate one side here to save the simulation time. The glue we are using is an UV-epoxy (Epotek OG 116-31) with a refractive index of 1.56.

The inverse taper will adiabatically change a larger weakly guided mode to a smaller stronger guided mode. To ensure this adiabatic changing does not cause much extra optical loss, the width of the inversed taper should be slowly and gradually changing in its geometric size. Therefore, we choose 500μm to be our taper length at the beginning. Fig. 2-8 (c) shows the simulation result of the fiber-waveguide coupling efficiency (TE mode) versus taper end width. As shown in the image, the coupling efficiency will reach its maximum for both 760nm and 1064nn when the taper tip width is around 70nm, which is around 80% for both wavelengths. This simulation is based on the waveguide structure which is 800nm in width and 300nm in thickness; and the inversed taper is 500μm in length to ensure the adiabatic condition; the extra rectangle which is shown as the “c” part in Fig. 2-7 is 50μm long to make up for the cleaving inaccuracy.

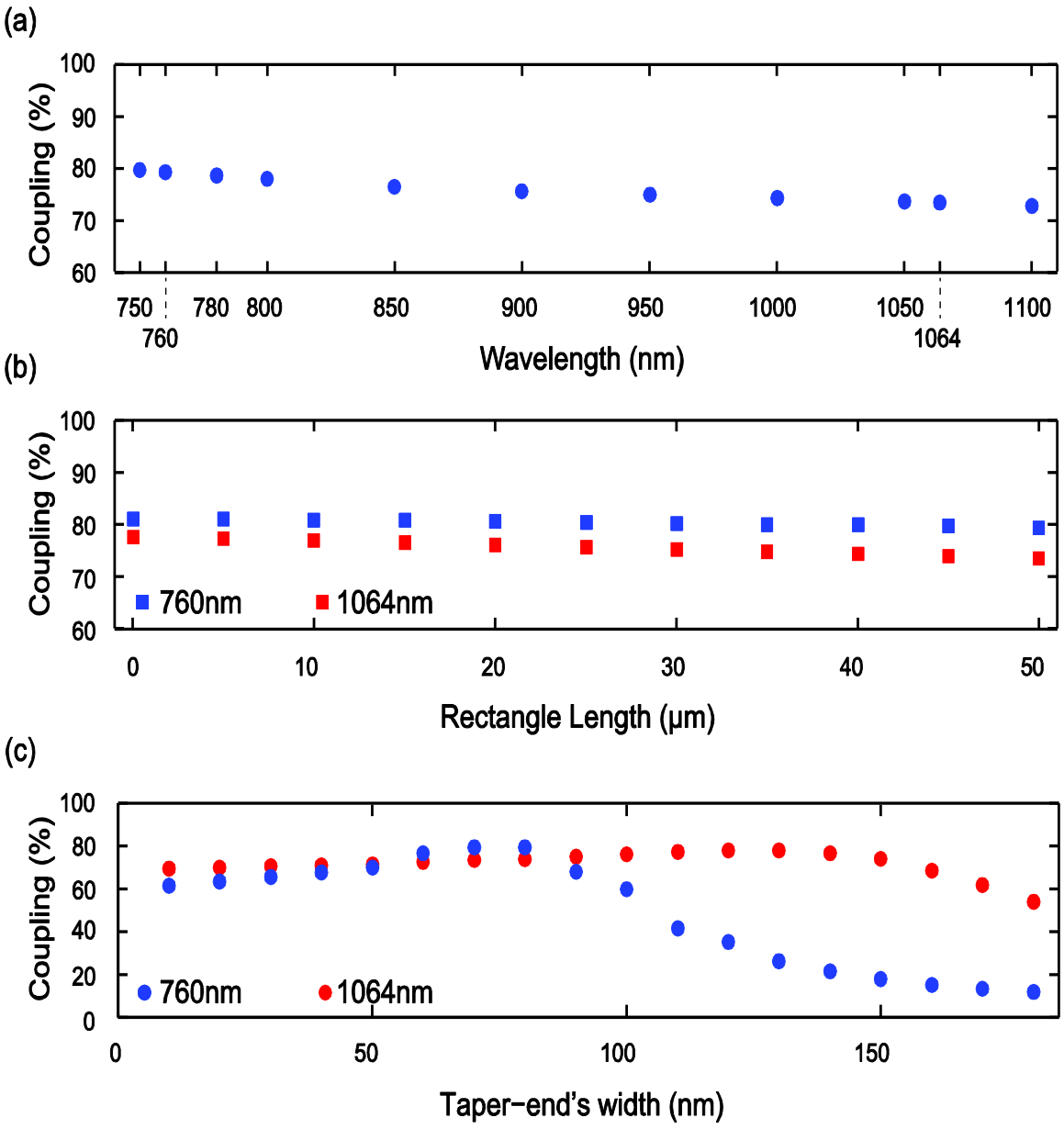

Figure 2-8: (a) fiber-waveguide coupling efficiency for wavelengths from 750nm to 1100nm by using the designed inversed taper, (b) fiber-waveguide coupling efficiency for 760nm and 1064nm wavelengths by adding an extra rectangle at end of the designed inversed taper with different lengths, (c) fiber-waveguide coupling efficiency for 760nm and 1064nm wavelengths by using an inversed taper with different taper-end widths

The simulation shows that the coupling efficiency is very sensitive to the taper end width especially for 760nm wavelength. However, our current cleaving technique has an

accuracy about plus/minus 20μm. If we cleave 40μm inside the taper, the real taper end width will be about 128nm instead of 70nm as designed. According to Fig. 2-8 (c), the coupling efficiency will drop from 79% to around 25% for a 760nm wavelength when the taper end width changes from 70nm to 128nm. Therefore, we have to introduce an extra rectangle at the end of the inverse taper to ensure that the tip width always remains the same after the cleaving. Fig. 2-8 (b) shows the simulation of fiber-waveguide coupling efficiency versus the length of that extra rectangle. As shown in the image, an extra 50μm-long rectangle only decreases the coupling efficiency by about 3%. As a result, this extra rectangle makes it possible for us to experimentally achieve high coupling efficiency reliably by using our current cleaving technique.

In addition, we also simulate the fiber-waveguide coupling efficiency based on our waveguide and taper design. Fig. 2-8 (a) shows that we can achieve a high coupling efficiency which is more than 75% for a wide near-infrared wavelength range from 750nm to 1100nm. This is quite meaningful since this wavelength range is widely used in many different fields such as quantum photonics and bio-sensing. This high coupling efficiency may potentially make it possible to transfer some complicated and large optical setup to a miniature on-chip design like a lab on a chip.

In summary, the taper we select is 500μm in length, 300nm in thickness and the taper end is 70nm in width, connected with a 50μm long 70nm wide rectangle for reliable cleaving. This taper can achieve high fiber-to-waveguide coupling efficiency for a wide range of wavelengths from 750nm to 1100nm, and the coupling efficiency for 760nm and 1064nm is expected to be about 80%.

2.3 Theoretical Calculation for Nanowaveguide Evanescent Field Trapping

In order to trap cold atoms, we first need to cool down the atoms since the atoms have too much kinetic energy at room temperature. According to our calculation, we need to cool down the atoms to less than 1mK (see Fig. 11). In order to achieve this, we need to use a Magneto-Optical Trap (MOT) to cool down the atoms as our first step.

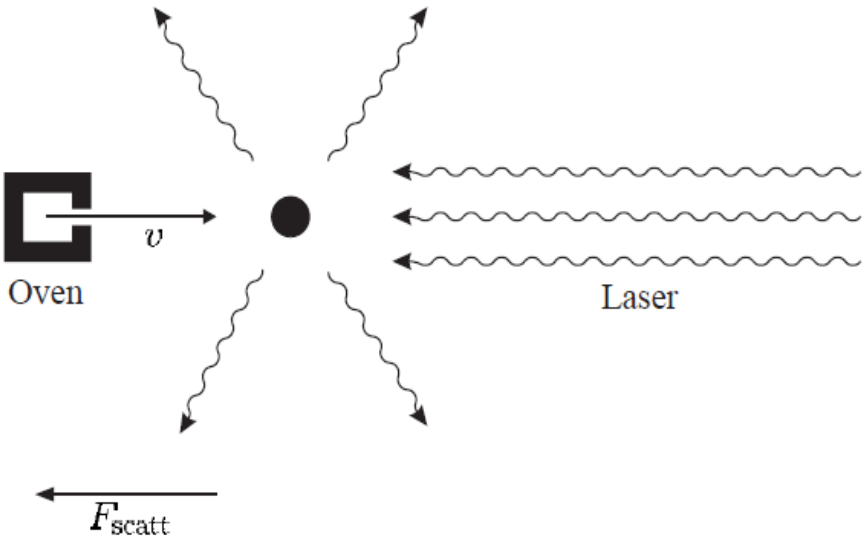

Figure 2-9: Schematic of scattering force of laser on an atom

Magneto-Optical Trap is based on the optical molasses concept. As shown in Fig. 2-9 [20], for an atom moving towards the laser, each absorbed photon gives the atom a kick in the direction opposite to its motion, and the scattered photons go in random directions, resulting in a force that slows down the atoms which can be described as the scattering force F_{scatt}. In this way, we use laser to cool down the atoms by slowing down their speed. This is the one-dimensional case, however, the atoms are moving randomly in all direction in reality. Therefore, laser cooling in all directions is required to reduce the

atom temperature and three pairs of counter-propagating laser beams along the Cartesian axes can achieve that.

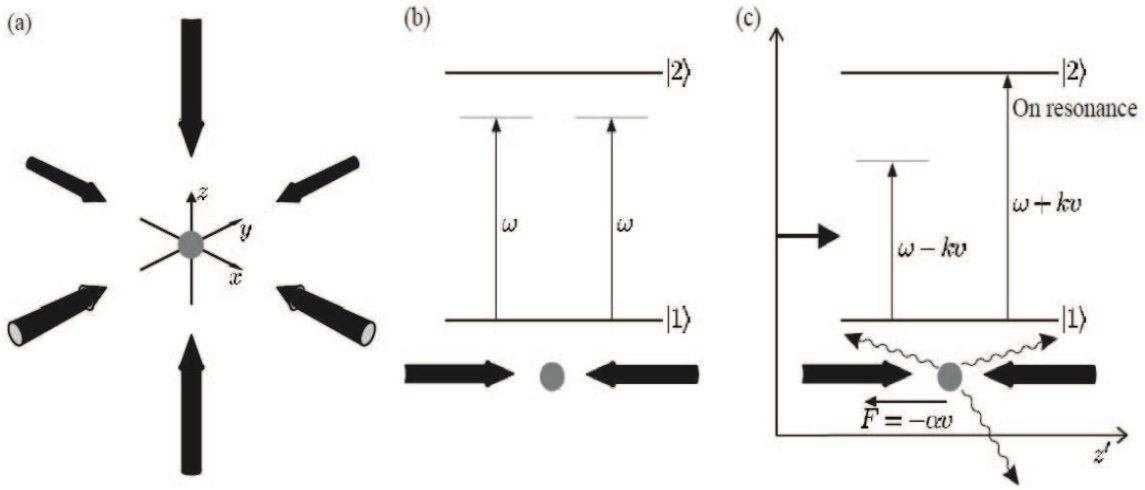

Figure 2-10: "Optical Molasses" technique is a laser cooling technique that uses the configuration of three orthogonal pairs of counter-propagating laser beams along the Cartesian axes shown in (a), a stationary atom in a pair of counter-propagating laser beams, as in (b), experiences no resultant force because the scattering is the same for each laser beam, but for a moving atom, as in (c), the Doppler effect leads to more scattering of the light propagating in the direction opposite to the atom's velocity

Fig. 2-10 [20] (a) shows this configuration where all of the laser beams are of the same frequency and are slightly below the transition frequency of the atom. If we only consider the atom as a two-level system with 2 energy states |1> and |2>, the relationship between a stationary atom and a pair of counter-propagating beam is shown in Fig. 2-10 (b). As a result, an atom at rest experiences no net force because the scattering force is the same in each direction. However, if the atom is moving towards the right with a speed of v, the atom will feel the two laser beams differently according to the Doppler Effect. For the laser beam coming from the right, the atom feels its frequency as ω+kv. For the other laser beam, the atom feels its frequency as ω-kv. Since the laser frequency is

slightly below the atomic transition frequency ω_0, the ω+kv is closer to ω_t than the ω-kv. Therefore, the atom will absorb more photons from the right laser beam which will result in a net force pointing to the left (shown in Fig. 2-10 (c)). This imbalance in the force arising from the Doppler shift can be written as [20]:

$$\begin{aligned} F_{molasses} &= F_{scatt}(\omega - \omega_0 - kv) - F_{scatt}(\omega - \omega_0 + kv) \\ &\cong F_{scatt}(\omega - \omega_0) - kv\frac{\partial F}{\partial \omega} - \left[F_{scatt}(\omega - \omega_0) + kv\frac{\partial F}{\partial \omega}\right] \\ &\cong -2\frac{\partial F}{\partial \omega}kv \cong -\alpha v \end{aligned}$$

According to the mathematical expression above, the atom experiences a damping force in the presence of light just like a particle in a viscous liquid. In this way, Steven Chu and other scientists first demonstrated this effect and called it the "Optical Molasses Techniques".

Compared to the optical molasses technique, the magneto-optical trap (MOT) has an extra quadrupole magnetic field which causes an imbalance in the scattering force of the laser beams and confines the atoms more strongly. Fig. 2-11 [20] (a) shows the configuration of the MOT, and in addition to the three pairs of the counter-propagating laser beams which have circular polarization, there is another pair of coils with current in the opposite direction of each other (Anti-Helmholtz coils) producing a quadrupole magnetic field. This field is zero at the center of the coils and its magnitude increases linearly in every direction from the zero point. As shown in Fig. 2-11 (b), for a simple J=0 to J=1 transition, the Zeeman Effect makes the J=1 level split into 3 different sub-levels (M_J=0, ±1) and causes their energy to vary linearly with the atom's position. For an atom moving to the right, the selection rules lead to σ^- transition between J=0 level

and M_J=-1 level of J=1. As the atom moves farther away from the center, the σ^- transition frequency becomes smaller and closer to the laser frequency, and then the imbalance of scattering force which push the atom back to the trapping center is stronger. For an atom moving to the left, the σ^+ transition between J=0 level and M_J=1 level of J=1 will similarly cause the imbalance of scattering force that also push the atom back to the center. In this way, the MOT can confine the atoms better and cool them to a colder temperature than simply the optical molasses technique, and we use these MOT cold atoms for the next step, which is the optical waveguide dipole trap.

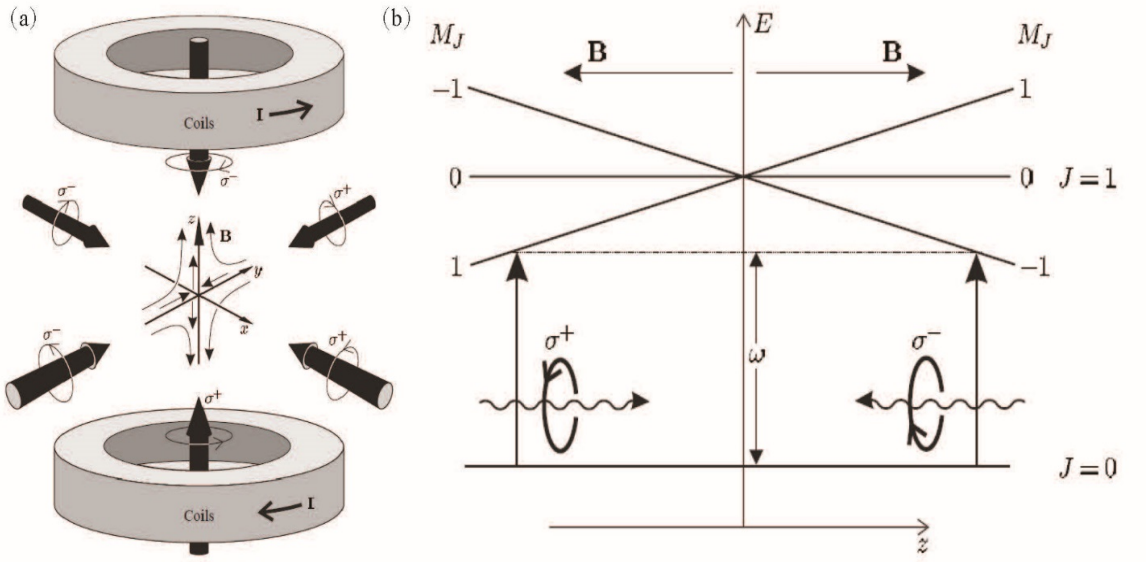

Figure 2-11: Schematic of Magneto-Optical Trap, (a) A magneto optical trap is formed from three orthogonal pairs of laser beams that have the requisite circular polarization states and intersect at the center of a pair of coils with opposite currents. The small arrows indicate the direction of the quadrupole magnetic field produced by the coils. (b) The split energy states of an atom in the quadrupole magnetic field according to Zeeman effect. Two counter-propagating beams of circularly-polarized light illuminate the atom and the selection rules for transitions between the Zeeman states lead to an imbalance in the radiative force from the laser beams that pushes the atom back towards the center of the trap.

In addition to the scattering force, there is another radiation force which is known as the dipole force (also known as the gradient force), which arises from the refraction of light. A simple example is a dielectric sphere in a laser beam of non-uniform intensity, a Gaussian distribution of light intensity for example. As shown in Fig. 2-12 [20](a), for a Gaussian laser beam propagating to the right, the dielectric sphere here acts as a converging lens with a short focal length. We consider two ray propagating through the sphere, and ray A has a higher intensity than ray B. Each ray will give the sphere a force which can be mathematically written as:

$$F = \left(\frac{IA}{c}\right) 2sin\left(\frac{\theta}{2}\right),$$

where I is the radiation intensity, A is the cross-sectional area, θ is the angle between the input and output direction of the ray.

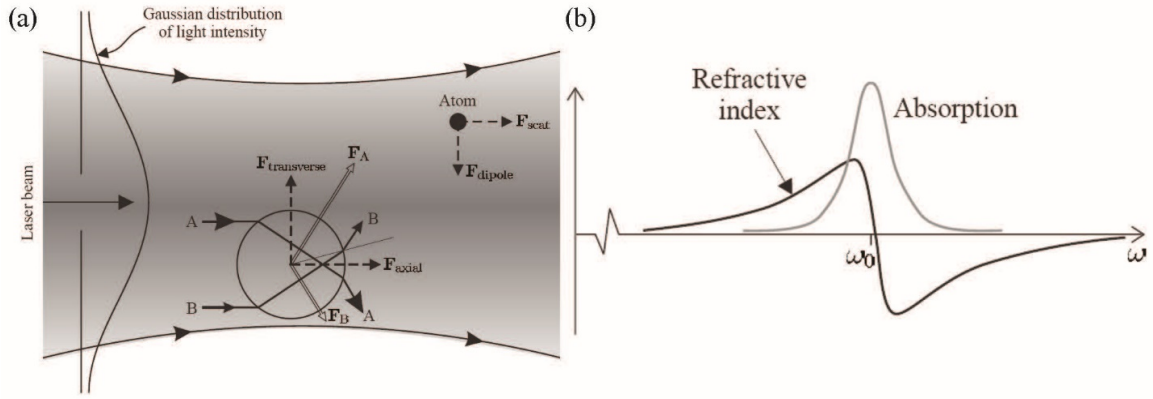

Figure 2-12: (a) dipole force of a dielectric sphere in a Gaussian laser beam; (b) frequency-dependent refractive index of material

Since the intensity of these two rays are different, the sphere will then feel an imbalanced force. If the sphere has a higher refractive index than the surrounding medium, the force will in the direction of the increasing intensity which attracts the sphere to the high intensity area; on the contrary, if the sphere has a lower refractive

index, the force will push the sphere away from the high intensity area. Fig. 2-12 (b) shows the refractive index dependence on frequency. ω_0 is the transition frequency of the atom, the x-axis is the frequency ω of the laser beam, the y-axis is the refractive index of the dielectric sphere. Therefore, when the laser frequency is lower than the atomic transition frequency (red detuned), the dipole force will attract the atoms to the high-intensity region; otherwise, it the laser is blue detuned, the atoms will be pushed away. This dipole force theory is the basic idea of our two-color waveguide evanescent field trap.

According to the dipole trapping theory as we discussed above, we use two laser beams of different frequencies to trap the atoms, one is red detuned with the wavelength of 1064nm, and the other is blue detuned with the wavelength of 760nm. For a large detuning ($\Delta=\omega-\omega_0$), the dipole potential can be written as:

$$U_{dip}(r) = \frac{3\pi c^2}{2\omega_0^3}\frac{\Gamma}{\Delta}I(r),$$

where $I(r)$ is the laser intensity, Γ is the spontaneous decay rate of the excited state. Therefore, a blue-detuned laser beam creates a repulsive potential ($\Delta_{blue}>0$); while a red-detuned laser beam creates an attractive potential ($\Delta_{red}<0$). Fig. 2-13 shows the surface potential of our optical nanowaveguide. The blue solid line is the potential of the blue-detuned laser beam (760nm), the red solid line is the potential of the red-detuned laser beam (1064nm), the red-dash line is the Van Der Waals potential of the waveguide, and the black line is the total potential of the waveguide surface which can be written as:

$$\begin{aligned} U_{tot} &= U_{blue} + U_{red} + U_{VDW} \\ &= \frac{3\pi c^2}{2\omega_0^3}\frac{\Gamma}{\Delta_{blue}}I_{blue}(r) + \frac{3\pi c^2}{2\omega_0^3}\frac{\Gamma}{\Delta_{red}}I_{red}(r) - \frac{C_{VDW}}{y^3}. \end{aligned}$$

As we can see from the plot, after cooling the atoms down to a temperature less than 1mK, the atoms can be trapped around 140nm above the waveguide surface.

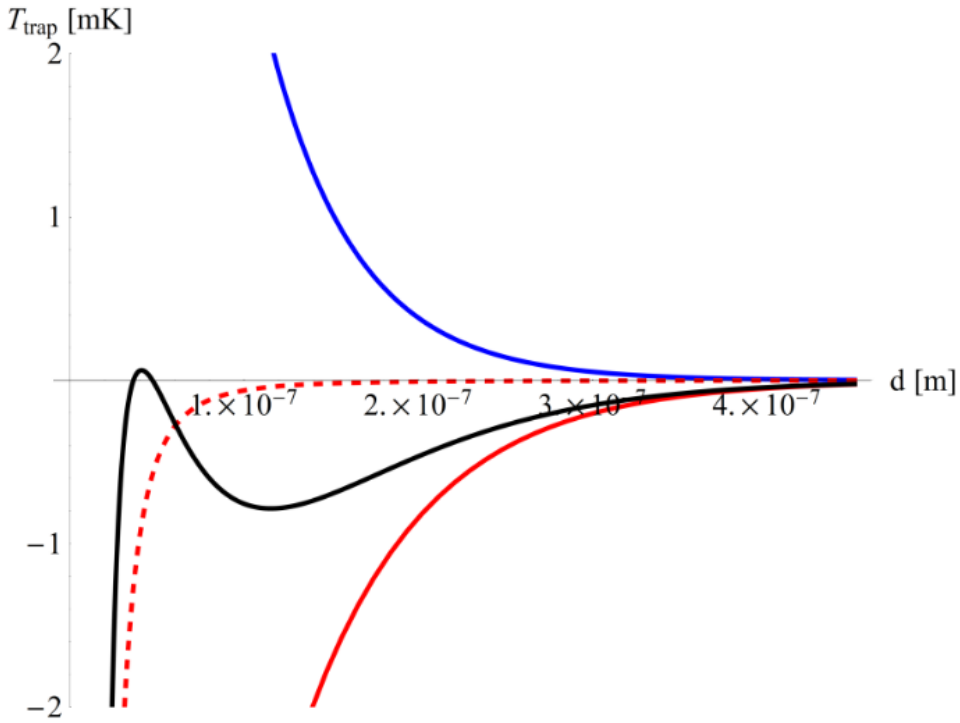

Figure 2-13: Trapping potential of the optical nanowaveguide

Chapter 3 : Experiments and Results

3.1 Waveguide and Inversed Taper Fabrication

We start the fabrication by depositing 300nm LPCVD Si_3N_4 on a 5μm thermal silicon dioxide coated (100) silicon wafer. After the deposition, the wafer was diced into many small rectangle samples with 18mm in length and 12mm in width, and then they were bathed in piranha solution for 30 minutes and rinsed in DI water for 5 minutes.

The next step is to pattern the waveguide and create an inverse taper structure by electron beam lithography (EBL). We are using PMMA 495 A4 as our ebeam resist. Since we have a 5μm thermal silicon dioxide and 300nm Si_3N_4 at the top which are both insulating layers, there is a severe charging effect during the EBL, which will prevent us from seeing the sample clearly and write very small structures. This may also cause stitching errors. Therefore, we spin a layer of Aquasave which is a conducting liquid polymer to reduce the charging effect. During the EBL, the FBMS (Fixed Beam Moving Stage) technique is applied to get rid of the stitching error. After the EBL and developing the sample properly, we deposit 20nm Cr on the sample by E-beam evaporation deposition and then we do the metal liftoff in hot acetone. Then we etch the Si_3N_4 down around 280nm to 290nm by using ICP (Inductively Coupled Plasma) etcher and using Cr as the etching mask. After this, we use Cr etchant to etch away the remaining Cr, and we deposit another 4μm SiO_2 by PECVD (Plasma Enhanced Chemical Vapor Deposition) for better coupling and future packaging.

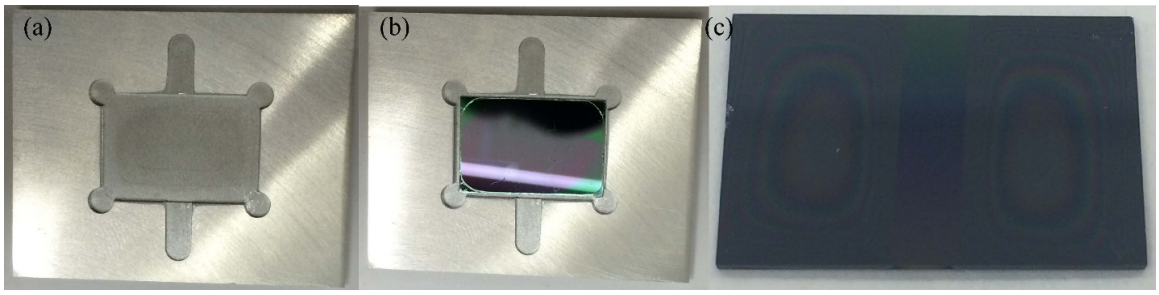

Figure 3-1: (a) shadow mask for PECVD SiO_2 deposition, (b) sample in the shadow mask, the center slot is for placing a narrow rectangle bar to block the PECVD deposition, (c) sample after PECVD SiO_2 deposition in this way

Since we need an open-window area for the atom trap, we must make the central area of the sample without SiO_2. We have tried two ways to achieve this. The first method is to make a shadow mask when we make the PECVD SiO_2 deposition. Fig. 3-1 (a) shows the sample holder I made. It has two separate slots. The bigger rectangle slot with 4 round corners is for placing the 18mm by 12mm sample, which is shown in Fig. 3-1 (b). The thinner slot across the center of the first slot is for placing a glass shadow mask. This smaller slot is 4mm in width and is about 450μm shallower than the bigger one since the sample is 500μm in thickness, we want the shadow mask to slightly touch the sample surface. Fig. 3-1 (c) is the deposition result after this technique, we can see that the deposition thickness is nonuniform on both sides since the PECVD SiO_2 deposition rate is different at the edge area. Besides, since the shadow mask is after all touching the sample, there are several scratches on the sample surface and sometimes on the waveguides unfortunately.

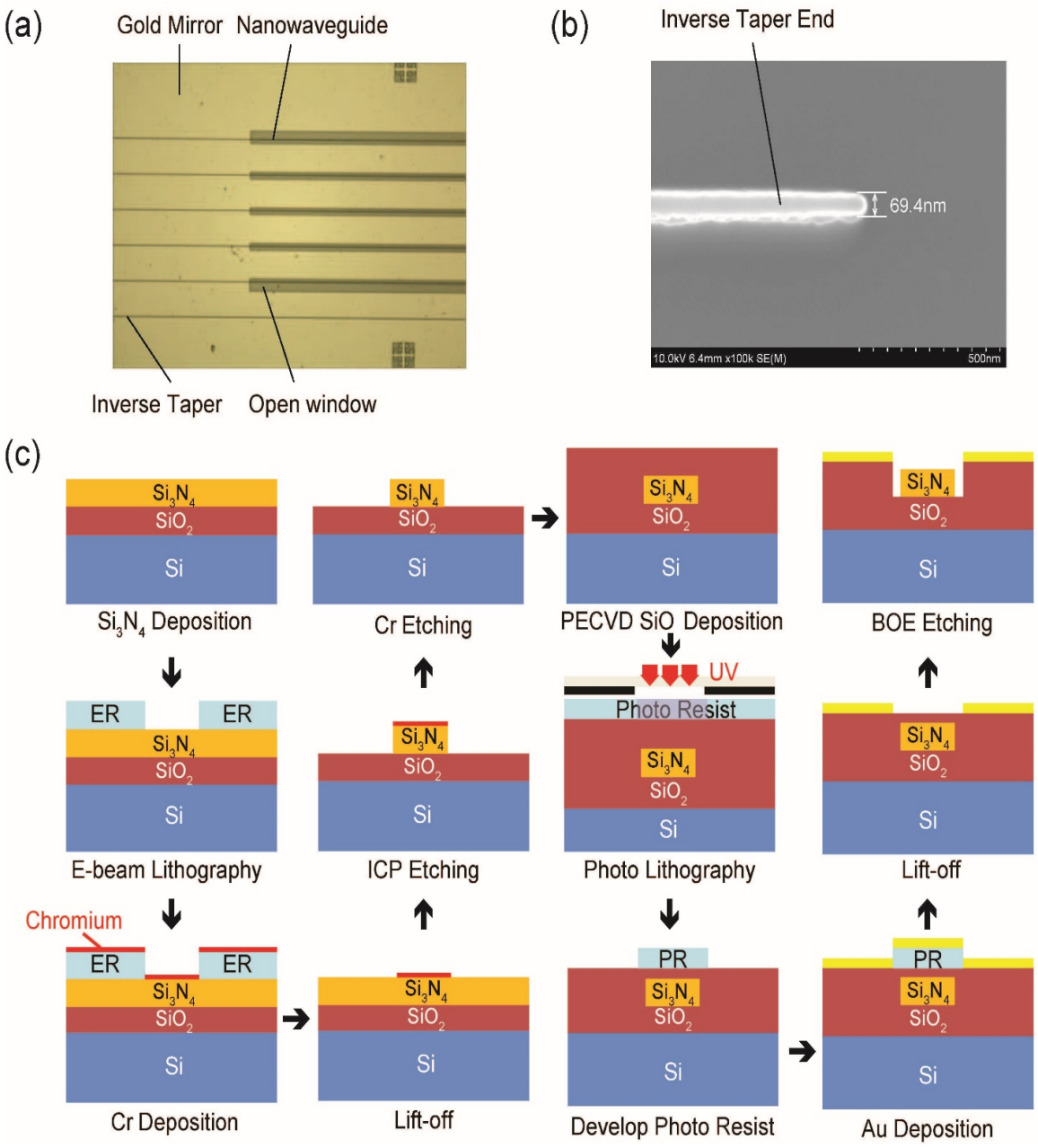

Figure 3-2: (a) optical microscopic image of the waveguide chip we fabricated, (b) SEM image of the inversed taper end, (c) schematic of the entire fabrication process

In the second method, we first deposit a plain layer of PECVD SiO_2 everywhere on the sample, then use photolithography to pattern the open-window structure, and at last, we etch away the PECVD SiO_2 on the patterned area by Buffered Oxide Etching (BOE). Since LPCVD Si_3N_4 has a very low etching rate under BOE compared to PECVD SiO_2,

the LPCVD Si_3N_4 acts as a stopping layer for this SiO_2 etching and that is why we leave 10nm to 20nm Si_3N_4 unetched at the beginning. Compared to the first method, this method can make very thin open window since we want the gold mirror to be very close to the waveguide. And we are now making 10μm and 20μm wide open window which makes the gold mirror very large and is only 5μm from the waveguide. Also, this method does not create any scratch on the sample surface. The last step is to deposit the gold mirror, using the benefit of the second method to make open window. We can deposit gold after the photolithography step and do the gold liftoff. Then the gold acts as the etching mask for PECVD SiO2 BOE etching.

Fig. 3-2 (a) shows the optical-microscope image of the waveguide chip. The yellow part is the gold mirror and the dark trenches are the open windows which are 20μm in width. The lines are the waveguides with inversed tapers at both ends. The simulation has shown that a taper with around 70nm in width will achieve best coupling efficiency for both 1064nm and 760nm wavelengths. Fig. 3-2 (b) shows the SEM image of the taper we made which is 69.4nm in width, in agreement with what we expected. Fig. 3-2 (c) briefly shows the whole fabrication procedure.

3.2 Cleaving and Polishing Technique for Fiber-Waveguide Coupling

After the fabrication, the sample needs to be cleaved for coupling. We have tried three different ways to cleave the sample.

The first method is the backside polishing and cleaving. The sample is originally 500μm in thickness. The backside of the sample is polished down to 100um to ensure ease of cleaving. The front side of the sample is glued to a piece of 200μm thick glass slide for protection. After the polishing, the sample is removed from the glass slide by

soaking into acetone for several hours. A deep scratch is made at the position under the optical microscope by a diamond scriber where a cleaving mark was written by EBL. The cleaving marks were written right under the end of the tapers close to the sample edge (as shown in Fig. 3-3 (a)). Then the sample is sandwiched by two plastic papers to be cleaved on a razor blade by applying a force on both sides of the razor blade. Fig. 3-3 (b) shows the side view of this cleaving. The red rectangle is the sample and the two green lines are the two plastic papers. The razor blade should touch the backside of the cleaving mark and be along the y direction, as shown in Fig. 3-3 (a). Since the sample has a substrate with (100) single-crystal silicon plane and the edges of the samples are diced to be along <110> crystal line, the sample will break along the y direction (<110> crystal line) at the cleaving mark position. Therefore, the taper can be precisely cleaved and a perfect mirror-like cleaving facet is obtained (shown in Fig. 3-4 (a) and (b)). This technique can achieve an accuracy in cleaving position around ±20μm in the x direction.

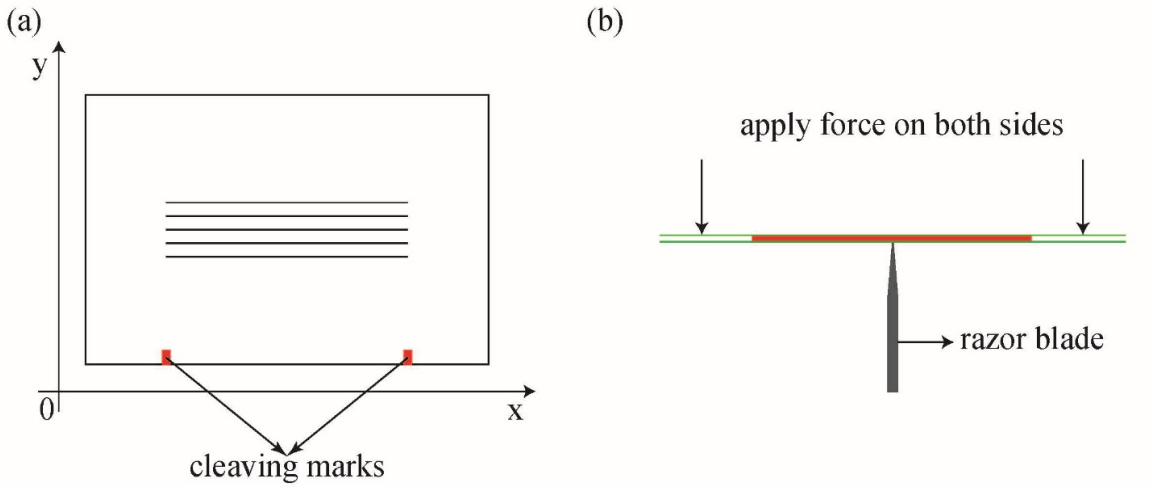

Figure 3-3: First cleaving technique, (a) schematic of the cleaving marks on the chip, (b) schematic of the way how we cleave the chip

The second method is dicing and side polishing. We first dice the waveguide chip by using a dicing saw. The taper end is about 1mm from the dicing edge and the diced facet is rough. Then we side polish the waveguide facet gradually starting from comparatively rough sand paper and progressively going down to 0.3 um grind-size sand paper. The polishing depth is well controlled by an integrated micrometer in self-made polishing holder (shown in Fig. 3-5 (a)). Although we can control very precisely the polishing depth, the smoothness of the facet is bad (shown in Fig. 3-4 (c) and (d)), especially for the top SiO_2 part which is much softer than the single-crystal silicon underneath because of the deposition quality. Since our waveguides are imbedded in this SiO_2 layer, this method cannot provide a good facet for waveguide-fiber coupling.

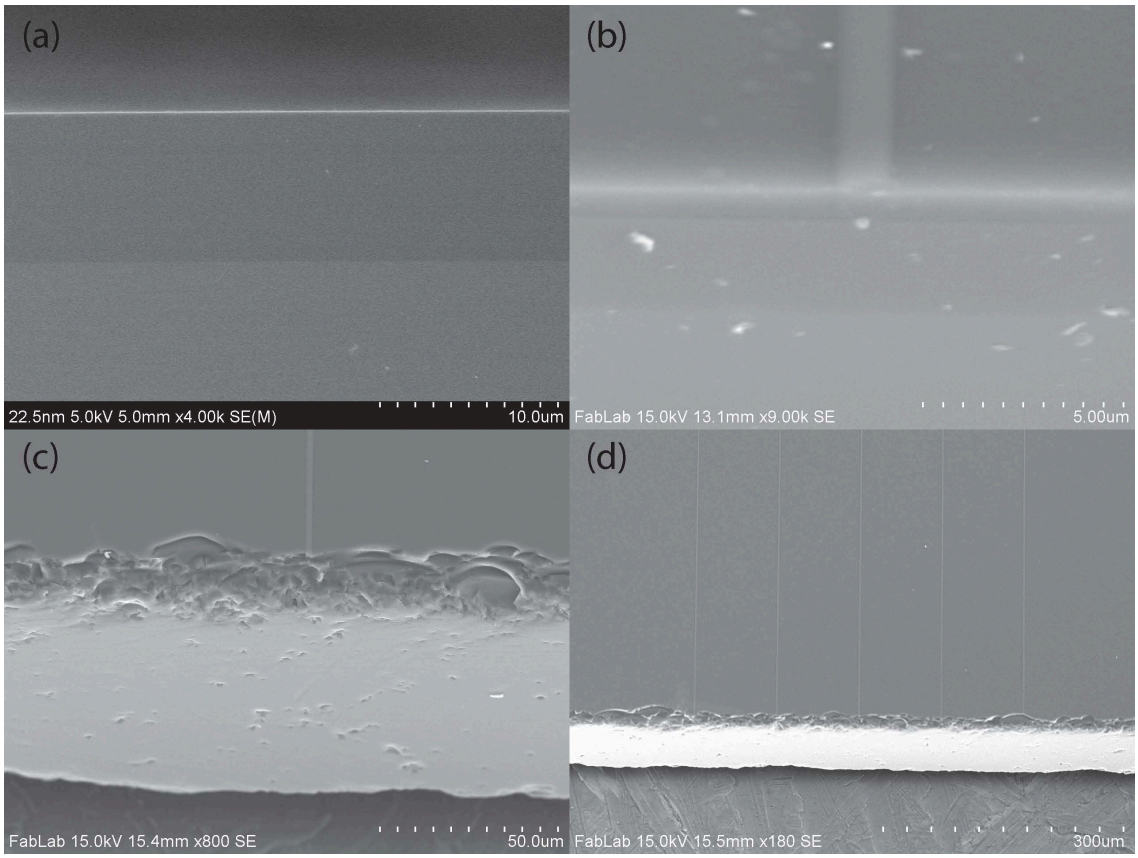

Figure 3-4: SEM images of the cleaved waveguide facets by direct cleaving (a & b) and sidewall polishing (c & d)

Since we need to deposit 100nm gold on the surface of our waveguide chip acting as a reflection mirror to achieve a mirror MOT, the sample surface has to be flat or it will have a diverging or a converging effect on the reflected laser beam. However, after using the first method for cleaving, it was found that the sample is slightly bending itself leading to a divergence of the reflected beam (as shown in Fig. 3-5 (b)). This is because the sample is too thin and the large surface stress from the 5μm thermal silicon dioxide and 4μm PECVD silicon dioxide on the front side of the chip leads to an imbalanced force that bends the sample.

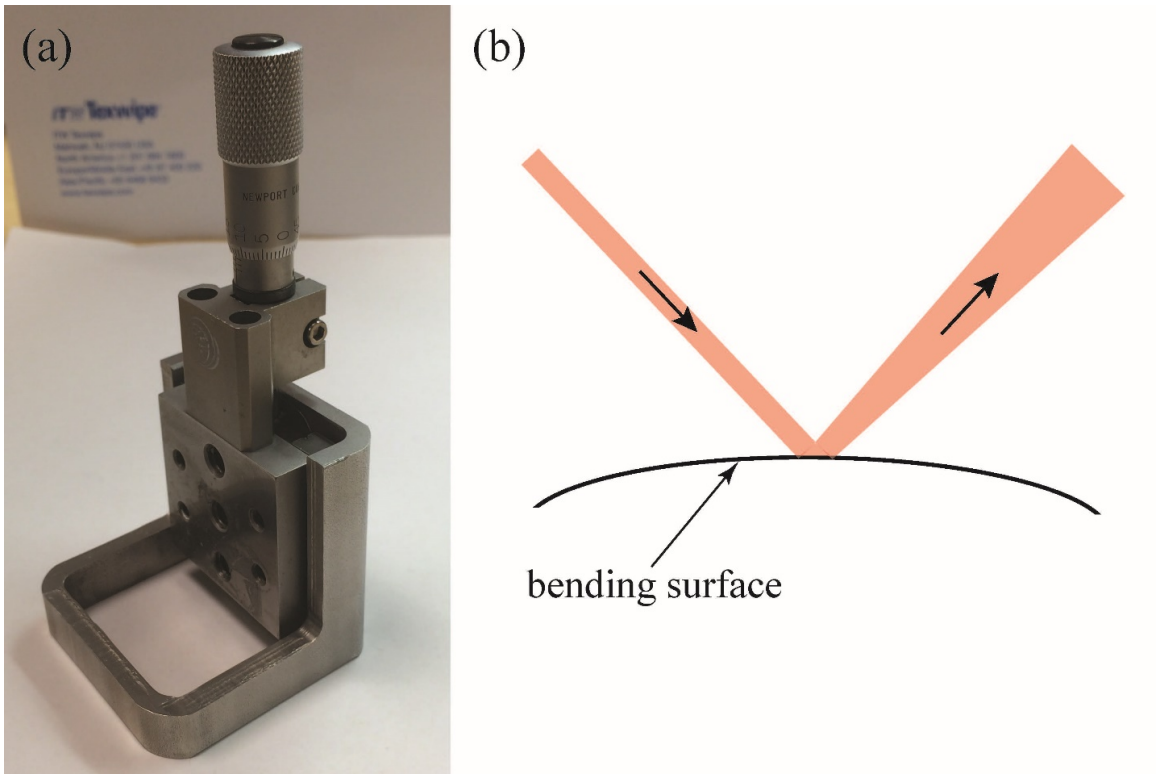

Figure 3-5: (a) self-made side polishing holder integrated with a micrometer translation stage, (b) Self-bending waveguide chip after backside polishing

The third method is a modification from the first method. The only difference is there is no backside polishing anymore. Instead, we make a much deeper scratch at the cleaving mark position and cleave it directly. In this way, since the chip is double-side coated with 5μm thermal silicon dioxide, the majority of the surface stress can be balanced. Besides, the sample is 500μm in thickness which is much thicker compared to 100μm, the surface stress of the 4μm PECVD silicon dioxide is weak and makes it hard to bend the chip again. Consequently, we finally choose the third method to be our standard cleaving technique.

3.3 Coupling Efficiency and Propagation Loss Measurement

We couple the fiber mode into the waveguide by gently attaching the fiber tip to the waveguide facet. In order to find the coupling position of the fiber precisely, two different methods are used to achieve the coupling. Fig. 3-6 shows the coupling setup we are using. The left part is a 5-axis translation stage for the input fiber with 3 computer controlled automatic axis and 2 manual axis; the middle part is a 2-axis translation stage for the waveguide chip; the right part is another 3-axis translation stage for the output fiber. Also, there are two cameras which give a side view and a top view of the coupling process.

For the first coupling method, we first need to align the input and output fibers with the waveguide in y direction and move the fiber tip close to the waveguide facet in the z direction. Then both fibers are moved in the x direction until they are only around tens of micrometers above the chip surface. Since the waveguide is about 1cm in length, the output fiber can detect about -30dB of the input at this time when both of the fibers are above the surface. Afterwards, we slowly move the input fiber downward until there is

only -50dB of the input light that can be detected at the output, which means the majority of the fiber mode is below the waveguide surface. Since the waveguide is only 4μm, we know the fiber mode is approximately near the waveguide facet, and part of the light is coupled into the waveguide. Then we slowly move the output along the –x direction until we see a sudden increase of the detected light power, and this is because the coupled light in the waveguide has been coupled into the output waveguide again. At this time, the fiber-waveguide-fiber coupling has been first established but the coupling has not been optimized yet. Therefore, several adjustments of the positions of input and output fibers need to be done until we detect the most laser power which is marked as P_{out}. We also need to do a fiber-fiber coupling to check how much laser power comes out of the input fiber. This is a reference point for our input power (P_{in}).

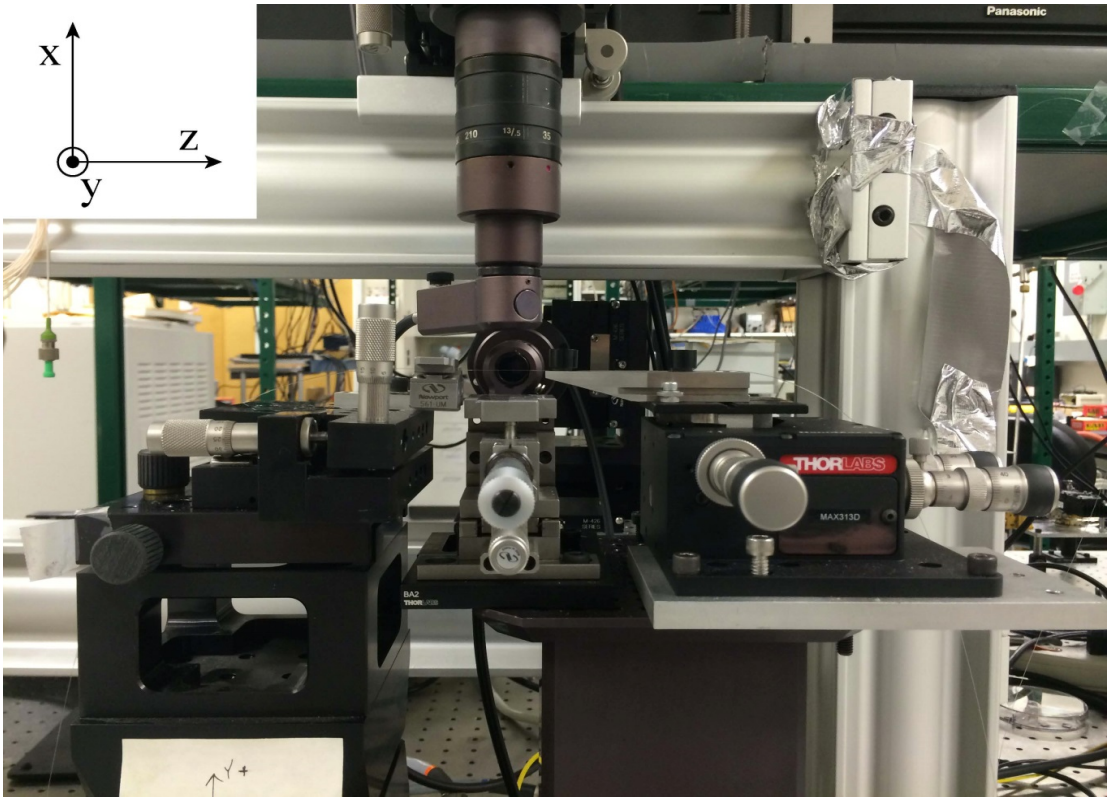

Figure 3-6: Setup for fiber – waveguide coupling

The first method can make the coupling very precise. However, since this method is based on the fiber-waveguide-fiber coupling which needs to achieve input coupling and output coupling at the same time. This is difficult and it usually takes a long time. The second method allows to do the input and output coupling one by one. Since we are trying to couple 760nm and 1064nm laser and both of them can be clearly seen by IR viewer. Therefore, if the waveguide is coupled, the waveguide itself will be lighted since there will be a large amount of scattering happening on the waveguide surface. In this way, we can simply only adjust the position of the input fiber until we see a lighted waveguide through the IR viewer, then we adjust the output fiber to find the output coupling. Several minor optimizations at both sides are also needed to find the best coupling. This method is much easier compared to the first one, and Fig. 3-7 shows the image of the light waveguide through the IR viewer.

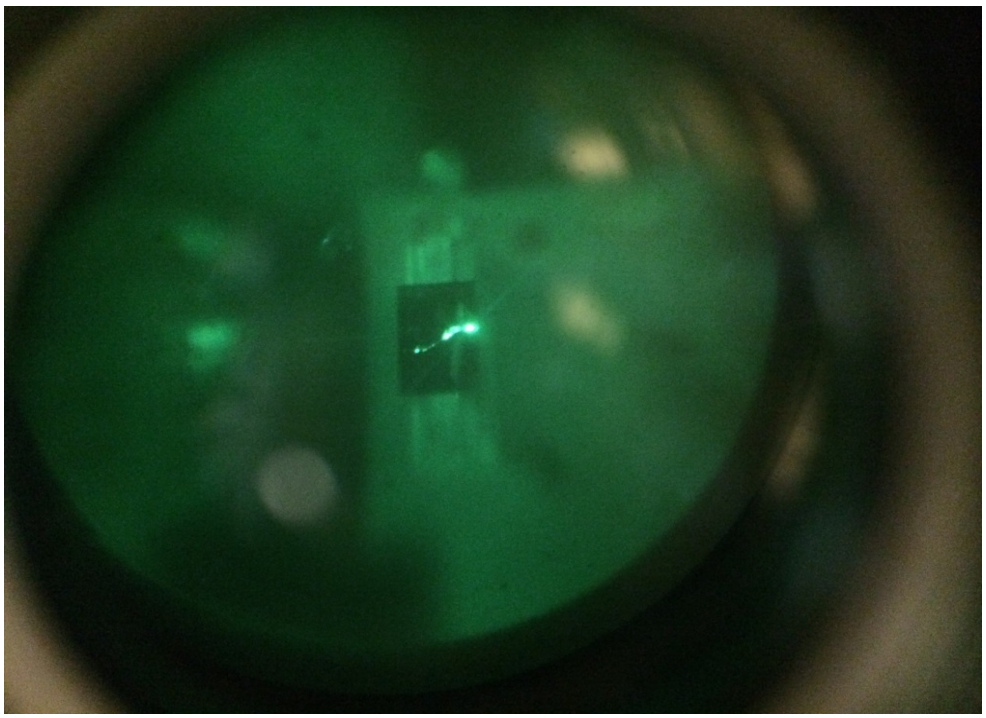

Figure 3-7: Shining waveguide seen through the IR viewer, the light is coupled into the waveguide from the right edge of the chip, and the waveguide is curved

The total loss, P_{loss}, equals to the input power from the input fiber P_{in} minus the output power in the output fiber P_{out} ($P_{loss}=P_{in}-P_{out}$). This loss includes the input coupling loss, output coupling loss and the propagation loss. Since the input fiber and the output fiber are exactly the same, and the taper structure at both end of the waveguide are also the same, the fiber-waveguide coupling efficiency at the input and output side should be the same. Therefore, the total loss P_{loss} equals two times the coupling loss per facet P_{closs} and the propagation loss P_{ploss} ($P_{loss}=2\times P_{closs}+P_{ploss}$). To better estimate the coupling efficiency, the propagation loss of the waveguide is also measured.

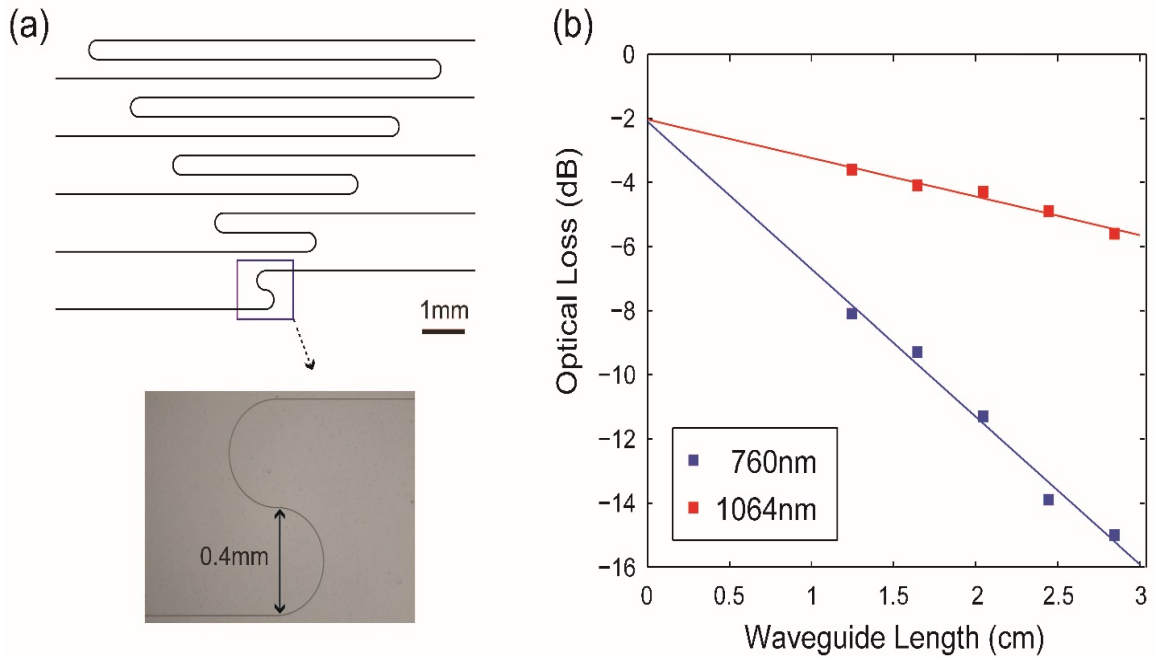

Figure 3-8: Propagation loss and coupling loss measurement. (a) E-beam lithography pattern for measuring the propagation loss and coupling loss, (b) experimentally measured insertion losses of the waveguides written by the patterns in (a)

The cut-back technique has been widely used for waveguide propagation loss measurements, but the accuracy of this measurement is highly dependent on the cleave quality. A small difference in the cleaving position and facet quality will result in big

changes in the coupling loss. This will make the propagation loss measurement unreliable since the cut-back technique is based on a precondition that the coupling loss after each "cut back" should be the same. Considering that our waveguide is short (1 cm in length), which can be hardly cleaved for too many times, and that our taper structure is very sensitive to the cleaving position, the traditional cut-back technique is not a good method for us. So we propose a new method to measure the propagation loss without cleaving the waveguide chip more than twice.

Instead of cleaving the single waveguide for many times, we cleave many waveguides of different lengths just in one time. Fig. 3-8 (a) shows the pattern of our design for this propagation measurement. We have five waveguides on chip with exactly the same width and thickness, each waveguide is 4mm different in length with the neighboring waveguides, and each waveguide contains two half-circle bends which are 400μm in diameter. Since our waveguide mode is strongly confined and the bends are very short compared to the 1cm waveguide, we assume that the extra bending loss is negligible and that the propagation loss is the same through the bending areas.

Fig. 3-8 (b) shows the measurement results. By cleaving just once, we have waveguides with five different lengths which are 1.2457, 1.6457, 2.0457, 2.4457 and 2.8457 in cm. The red squares are the experimentally measured total loss P_{loss} of these five waveguides for 1064nm wavelength, and similarly the blue squares are for the 760nm wavelength. The red and blue lines are the linear fit to these experimental results. The slope of the fitting line represents the propagation loss per centimeter, and the point of intersection at the y axis of the fitting line represents the coupling loss. Therefore, the estimated propagation losses from these fitting lines are -4.6dB/cm at 760nm and -

1.2dB/cm at 1064nm, and the total coupling losses from the y axis intersection points are -2.11dB at 760nm and -2.044dB at 1064nm. Since we consider the two facet have the same coupling loss, so the coupling efficiency per facet is 78.3% at 760nm (-1.055dB coupling loss) and 79% at 1064nm (-1.022 dB coupling loss). These experimental results are well matched with our simulation result shown in Fig. 8.

3.4 Packaging for an Atomic Cell

The atom trap requires a vacuum environment. To achieve this, we package the waveguide chip along with the fibers in a glass cell to make a portable atomic cell for the atom trap. Fig. 3-9 shows the packaging process to make this cell.

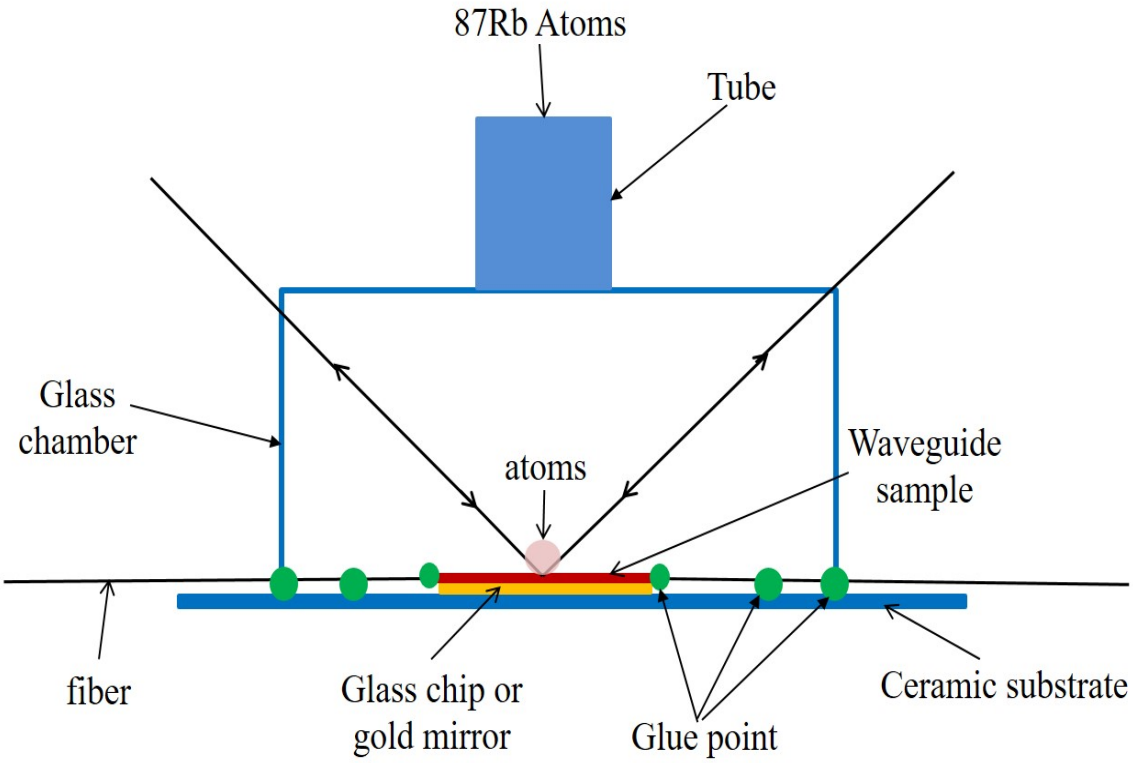

Figure 3-9: Packaging process for atomic cell

Here we use an UV-epoxy (Epotek OG 116-31) with a refractive index of 1.56 to glue the fiber to the waveguide chip, the waveguide chip to the substrate and the glass

cell to the substrate. Since we only shine UV light from the top side, the curing of the epoxy has different speed in different direction according to different exposure rate, the fiber will be pushed to direction with slower curing speed. In order to maintain the high coupling efficiency while curing the UV epoxy, we first only apply very little amount of epoxy at the fiber tips as shown in the figure. Also we need to do some adjustment of the fiber position during the epoxy curing to keep the best coupling efficiency. After we glue the input and output fiber to the waveguide chip one by one, we apply a comparatively large amount of epoxy several millimeters away from the fiber tip to glue the fiber to the ceramic substrate, which make the glue strong enough under different situations. After that, we seal the glass chamber to the ceramic substrate and glue a glass tube to the top of the glass chamber. The tube will be connected to the atom source and the pumping system. Fig. 3-10 shows the packaged atomic cell.

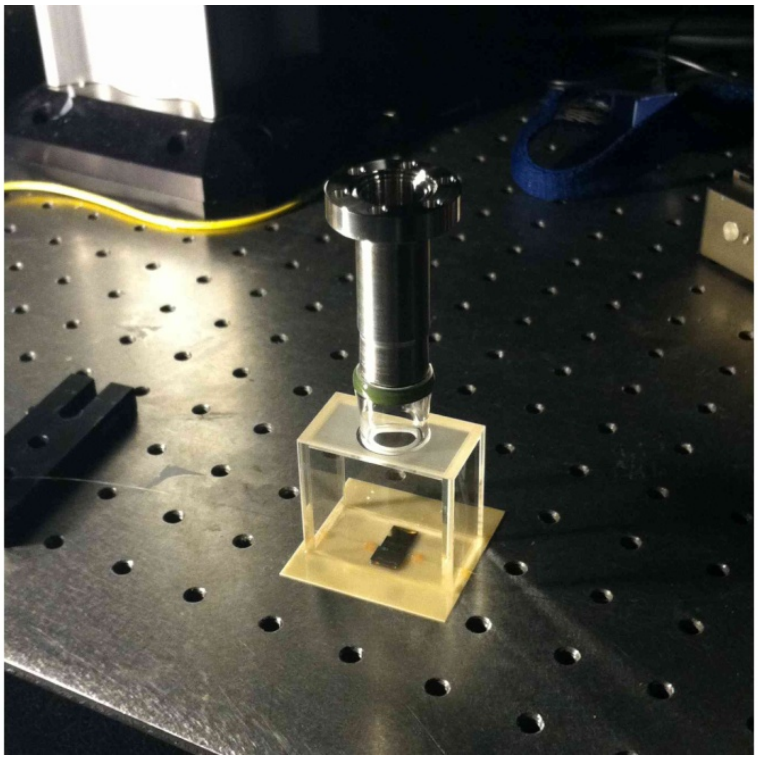

Figure 3-10: Packaged atomic cell

3.5 Integrated Gold Mirror MOT

Since the waveguide chip is not transparent to 1064nm laser, we cannot achieve a MOT by simply applying 3 pairs of counter-propagating cooling laser beams as shown in Fig. 2-11 (a). Instead, we use a gold mirror to achieve the MOT by only using two laser beams. One beam shines onto the gold mirror with a 45^{o} angle to the surface and is reflected by the gold mirror, then the reflected laser beam is normally reflected by another mirror to come back along its incident path and then reflected by the gold mirror again at the same position. Another laser beam shines through the interaction point of the four other laser beams along the direction perpendicular to the plane formed by those beams. The MOT atoms will be at the intersection point of all these beams and are very close to the gold mirror surface, as shown in Fig. 3-11.

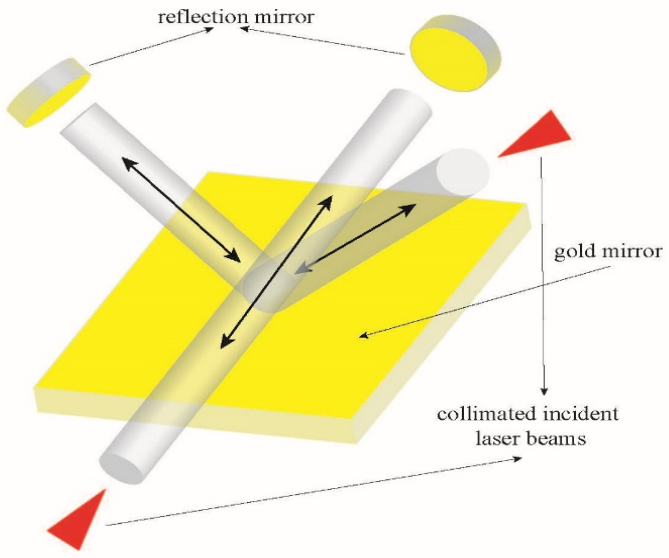

Figure 3-11: Schematic of the mirror MOT

In order to integrate this gold mirror MOT with our waveguides, we designed two methods to achieve this. The first method is to make the gold mirror and the waveguides on two different chips, as shown in Fig. 3-12. We first make a cleaving just near to the

waveguide and polish the edge until about 100μm from the waveguide. Then the waveguide chip is glued onto the gold mirror. We can achieve the mirror MOT near the edge of the chip and part of the MOT atoms will overlap with the waveguide for the waveguide atom trap. Fig. 3-12 (a) and (c) show the schematic image of this gold mirror MOT design, and Fig. 3-12 (b) shows the real image of our fabricated integrated mirror MOT with waveguide chip under this design. This design is comparatively easy to fabricate. However, since it is dangerous to polish the edge too close to the waveguide without hurting it and the overlapping area between the MOT atoms and the waveguide is limited, it is better to move the center of the MOT atom cloud closer to the waveguide. Our second design of the integrated mirror MOT was used to solve this problem.

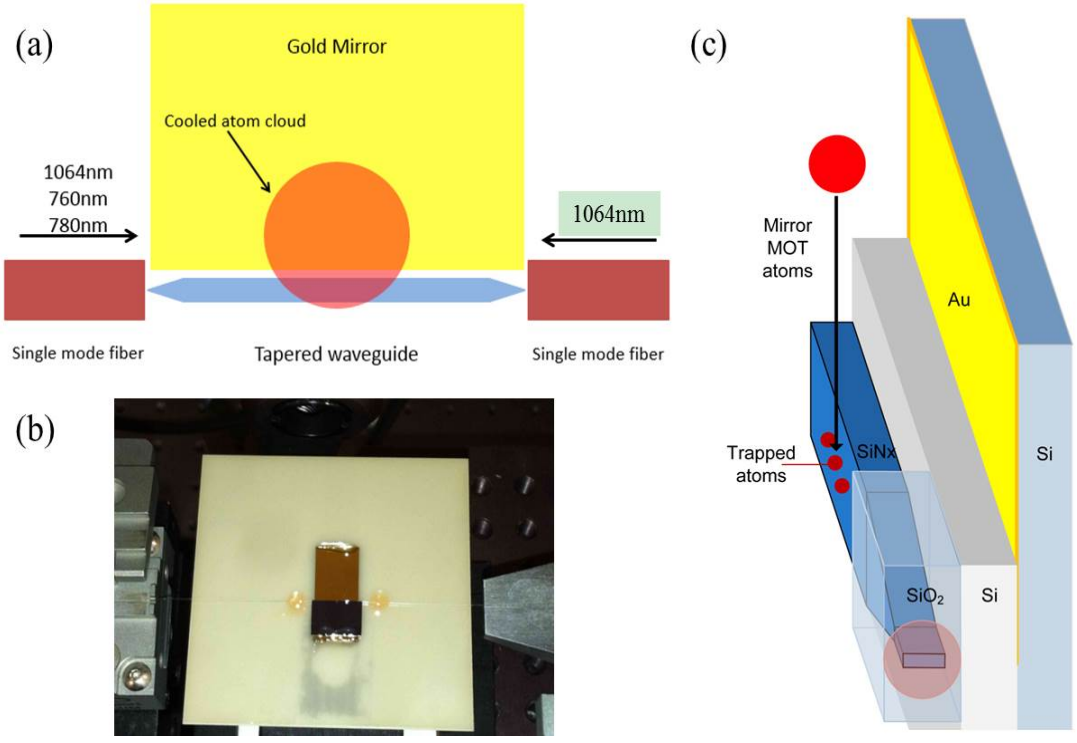

Figure 3-12: First design of the integrated gold mirror MOT. (a) & (c) schematic of this mirror MOT design, (b) image of the mirror MOT of this design we built

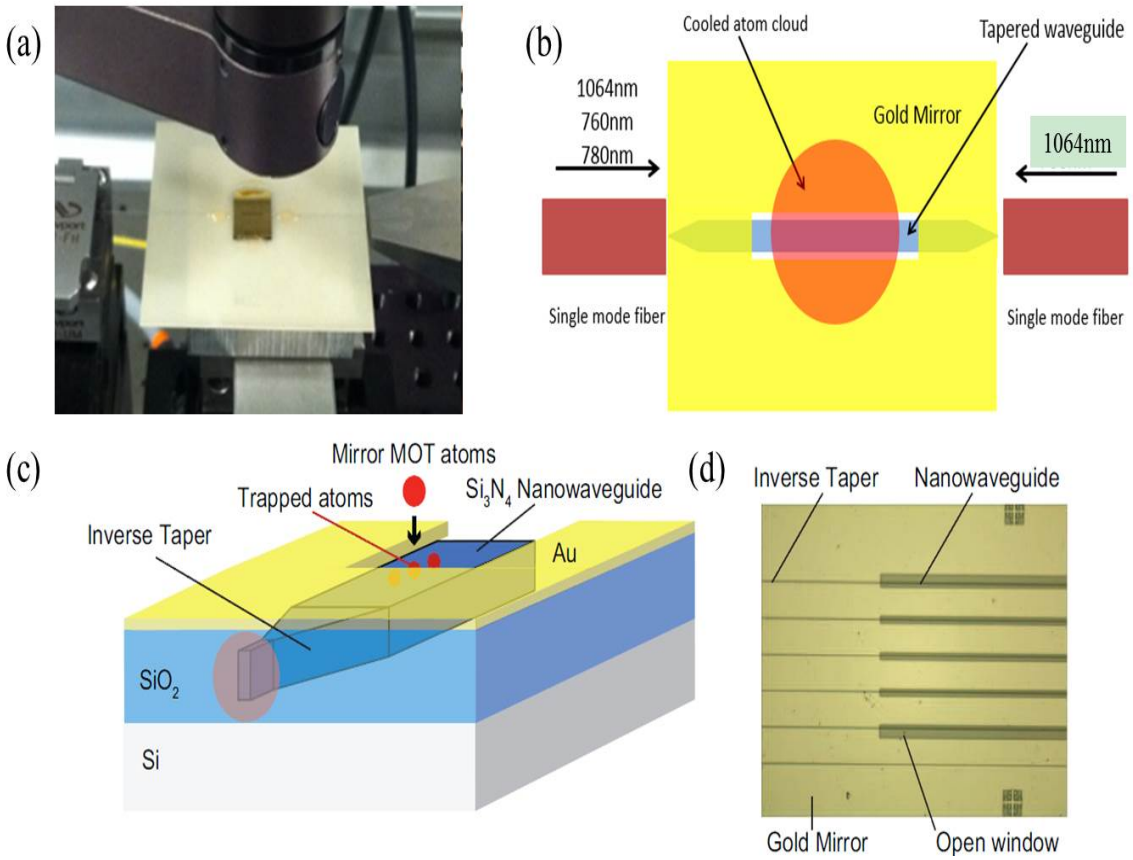

Figure 3-13: Second design of the integrated mirror MOT. (a) image of the mirror MOT of this design we built, (b) & (c) schematic of this mirror MOT design, (d) optical microscopic image of the waveguide chip of this design

Instead of fabricating the gold mirror and the waveguide onto two separate chips, the second design enables putting them together on the same chip by depositing gold on the top of the waveguide which is shown in Fig. 3-13. After depositing 4μm SiO_2 on the waveguide by PECVD, an open window structure is patterned by photolithography, followed by a 100nm gold deposition by E-beam evaporation deposition and liftoff. Then the chip is soaked in the BOE solution to etch away the SiO2 in the open-window area while the gold mirror acts as an etching mask. Compared to the first design, this design enables the center of the MOT atom cloud to be just on top of the waveguide, which allows stronger photon-atom interaction. Besides, since the open-window structure is

patterned by photolithography, the window can be as small as 5μm in width and currently we make it as 20μm in width. Such a small open window will not affect reflection on the gold mirror to achieve the mirror MOT. Fig. 3-13 (b) and (c) shows the schematic images of this integrated mirror MOT, and Fig. 3-13 (a) and (d) shows its real image on the coupling stage and under the optical microscope.

Fig. 3-14 (a) shows the mirror MOT we achieved experimentally, which is the white spot on the middle of the chip. And Fig. 3-14 (b) shows the laser setup configuration we used for this mirror MOT. As shown in this image, we can see the atomic cell, two anti-Helmholtz coils, laser sources and the reflectors.

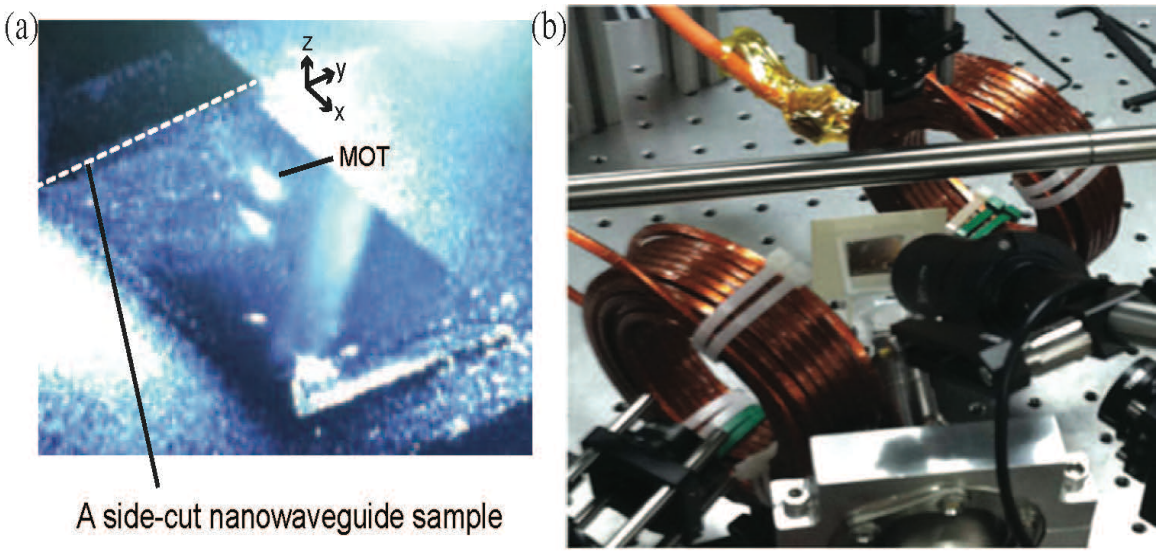

Figure 3-14: (a) Experimentally achieved gold mirror MOT; (b) setup for trapping atoms

3.6 Photon-atom interaction measurement: Thermal atom absorption

Before trapping the MOT atoms by our optical nanowaveguide, we first tested the platform by measuring the photon interaction with thermal atoms. We first pump the atomic cell to an ultra-high vacuum of about 1×10^{-9} mbar, and gradually excite the atoms into the glass chamber until we can see strong atomic fluorescence in the chamber and

heat the chamber to about 90°C to increase the atom density. We also measured the absorption signal of thermal atoms near the waveguide chip surface from a free-space collimated probing laser beam to act as a reference for estimating the absorption signal through the nanowaveguide.

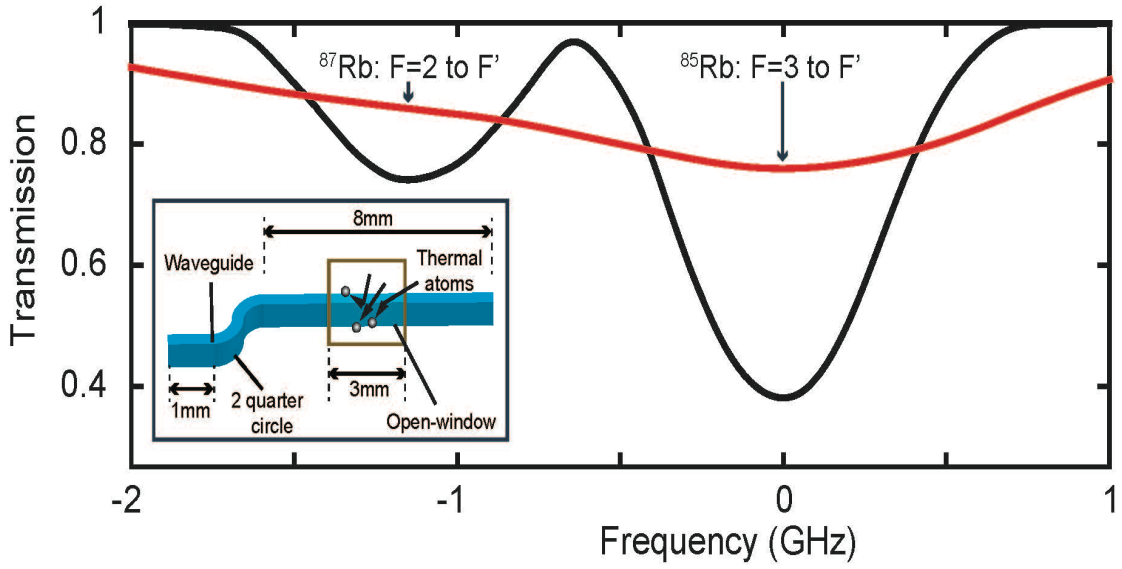

Figure 3-15: Absorption profile of thermal atoms with L-shaped nanowaveguide

Fig. 3-15 [21] shows the absorption signal of thermal ^{87}Rb atoms from a free-space collimated laser beam (black line) and through a nanowaveguide probe (red line). The profile shows the ^{85}Rb and ^{87}Rb D2 transitions (from the 5S1/2 ground state to the 5P3/2 excited state). The probing laser has the power of 2μW and the proportion of the evanescent field in optical power of the probing laser is 3.2%. As shown in the low-left corner of Fig. 3-15, an L-shaped waveguide is used to eliminate the uncoupled light and increase the signal-to-noise ratio. The open window is 3mm in length and the two quarter circles are 1mm in radius. The total measured broadening is $2\pi \times$ 765MHz (FWHM) including the Doppler broadening and transit-time broadening. The black line

shows a strong absorption of thermal Rb atoms from the free-space laser beam. The absorption of thermal atoms through the probe in the nanowaveguide is shown as the red line. It has the expected behavior but with a lower absorption rate. This is because the probing power is much higher than the saturation power. The saturation power is determined by the atom density, a higher atom density will contribute more optical absorption and a deeper absorption peak can be observed. If the saturation power is too low compared to the probing power, the absorbed photons are very few compared to all the probing photons and then makes the absorption peak very unobvious. This can be improved by increasing the atomic density or by reducing the probe power. Currently, our chamber is comparatively large so it is difficult for us to increase the atom density too much, and our photo detector cannot measure the laser power precisely when it is lower than 100nW. With a smaller chamber for higher atom density and better photo detector, we can see a deeper absorption peak from the optical evanescent field.

Chapter 4 : Conclusions

In our work, we proposed a nanowaveguide platform for collective atom-light interaction through an optical nanowaveguide evanescent field coupling technique. We have designed, fabricated and demonstrated an on-chip photonic circuit with centimeter-long Si_3N_4 nanowaveguide for trapping and probing the collective thermal and laser cooling ^{87}Rb atoms.

The nanowaveguide has a sub-micrometer mode size and high coupling efficiencies for a wide near-infrared wavelength range from 750nm to 1100nm. We have demonstrated the trapping and probing ability of the on-chip nanowaveguide by characterizing the mode profile and calculating the combined trapping potential near the waveguide surface. We have also designed and fabricated the inverse tapers at both ends of the waveguides that adiabatically transfer the weakly guided fiber-coupled mode to a strongly guided waveguide mode for a much better fiber-waveguide coupling efficiency. The coupling efficiency has been successfully improved from around 2% to around 80% for both wavelengths (760nm, and 1064nm) experimentally. We have also experimentally achieved a comparatively low propagation loss of the nanowaveguide that will contribute to a more stable trapping potential along the waveguide.

Trapping atoms usually needs high optical power, so the small mode (sub-micrometer) size of the nanowaveguide will generate very high heat flux in an ultra-high vacuum system. Compared to other types of atom traps that use the evanescent field of tapered fibers or a stand-alone photonic crystal waveguide with no substrate, our platform

has much better thermal conductance and is able to transfer high enough optical powers into the waveguide to trap atoms in an ultra-high vacuum environment.

We have also successfully realized an efficient packaging method to build a compact atomic cell (shown in Fig. 3-9 and Fig. 3-10). We have used an UV epoxy to glue the fiber with the waveguide facet that almost does not introduce any extra coupling loss. The atomic cell is also sealed with a mechanically strong ceramic substrate and can achieve an ultra-high vacuum that is lower than 10^{-9} mbar.

We have experimentally measured the optical absorption of thermal ^{87}Rb through the guided waveguide mode. We have also demonstrated an atom-chip mirror MOT with the same dimension of the platform that can be transferred in proximity to the waveguide surface by magnetic field controls.

Part II

Echelle-Grating Spectrometer in Near Infrared Wavelength Range for Astrophotonics

Chapter 5 : Theories and Introduction

5.1 Astronomical Spectroscopy and the Rise of Astrophotonics

In astronomical applications, wavelength analysis is very important especially for the wavelength selecting and filtering. Here we focus on the wavelength range from 1μm to 1.7μm. There are many valuable applications that make this near infrared wavelength range so important. For example, the Lyman-alpha line of hydrogen is a very important spectral line for us to understand the origin and creation of the universe. Since the universe has expanded for more than 10 billion years after the big bang, the Lyman-alpha line of hydrogen has redshifted from 121.5nm to the 1μm-to-1.7μm wavelength range according to Hubble's Law. In addition, analysis of this wavelength range can also help us understand many other cosmic phenomena such as quasars, Gamma-ray bursts, etc. Therefore, a good spectrometer is needed to achieve this.

Here we present an echelle grating which is based on an on-chip spectrometer that covers the near infrared wavelength range from 1.45um to 1.7um. To begin with, we use optical waveguides as the input and output channels. We have successfully achieved a reliable fabrication process to make the on-chip echelle-grating spectrometer. We have also achieved high fiber-waveguide coupling efficiency (94% per facet at 1550nm) and low propagation loss (-0.975dB/cm at 1550nm) for the input and output waveguides. In addition, we have characterized the bending loss of the waveguide. Finally, we have successfully measured the output spectrum of the echelle grating we designed and found it to be in good agreement with our simulation.

5.11 Brief History of Astronomy

Astronomy is a natural science that studies celestial objects and phenomena. Human beings have started to discover the universe thousands of years ago. For example, the earliest known star catalogues were compiled by the ancient Babylonians of Mesopotamia in the late 2nd millennium BC, and a Chinese astronomer recorded the first supernova in "Houhanshu" in 185 AD.

Until about 500 years ago, astronomy entered its modern age because of the invention of new techniques and equipment. Telescopes were invented around 1600, and Galileo Galilei (1561 - 1642), an Italian astronomer and physicist, was the first to use a telescope to discover the universe. He constructed a telescope that consisted of a convex objective and a concave eyepiece lens. With this instrument, Galileo discovered the four bright satellites of Jupiter, the phases of Venus, mountains on the Moon, spots on the Sun, the rings of Saturn, and the nebulous Praesepe (also known as Beehive cluster or M44). After that, many great discoveries were made by using the telescopes such as the first diffuse nebula, Orion Nebula M42, discovered by Peiresc in 1610 and the first supernova remnant, Crab Nebula M1, discovered by John Bevis in 1731.

Since 19th century, more significant developments were made in astronomy due to the rise of interest in astrophysics such as in astronomical spectroscopy, astrophotography, better and larger telescopes, and so on. Astronomers in old days could only discover the universe based on what they saw by eyes while losing a lot of other information. However, current observational astronomy has broadened its spectrum from only visible light to a much wider optical range from radio frequency to Gamma ray.

Thanks to the great development of new technology, today's astronomers can see a much bigger, deeper, clearer and more comprehensive universe than ever before.

5.12 Brief Introduction of Astronomical Spectroscopy

Spectroscopy is the study of the interaction between matter and electromagnetic radiation. While astronomical spectroscopy is the study of astronomy using the techniques of spectroscopy to measure the spectrum of electromagnetic radiation, mainly including radio, infrared light, visible light, ultraviolet light, X ray and Gamma ray. These radiations come from the stars, planets and other celestial objects. It is one of the most fundamental and important techniques used by astronomers. With the help of astronomical spectroscopy, new properties of the universe or new celestial objects can be measured such as the chemical composition, temperature, density, mass, distance, luminosity, relative motion and even the age of the universe.

As early as 1666, Isaac Newton (1643 - 1727) found that the sunlight could be dispersed into a continuous spectrum when passing through a simple prism. And in 1818, Joseph von Fraunhofer (1787 - 1826) extended this work and first got a good spectrum of the sun and observed 576 dark lines in it. The explanation of these dark lines was later proposed in the work of Gustav Kirchhoff (1824 -1887) and Robert Bunsen (1811 - 1899), which said the dark lines were due to the selective absorption of a continuous spectrum emitted by the hot interior of the sun by cooler gases at the surface. After that, many contributions were made and the spectroscopic technologies were also improved considerably.

5.13 Different Types of Optical Spectrometers

An optical spectrometer, also known as a spectrograph in astronomy, is an instrument used to measure the properties of light (over a spectral range that usually covers the UV, the visible and the IR spectra) by measuring the wavelengths and intensities of the spectral lines. According to the different working theory, optical spectrometers can be classified into various categories. The popular ones are spectrometers based on a Fabry-Perot interferometer, Fourier transform spectrometers and the dispersive spectrometers.

(1) Spectrometer based on Fabry-Perot interferometer

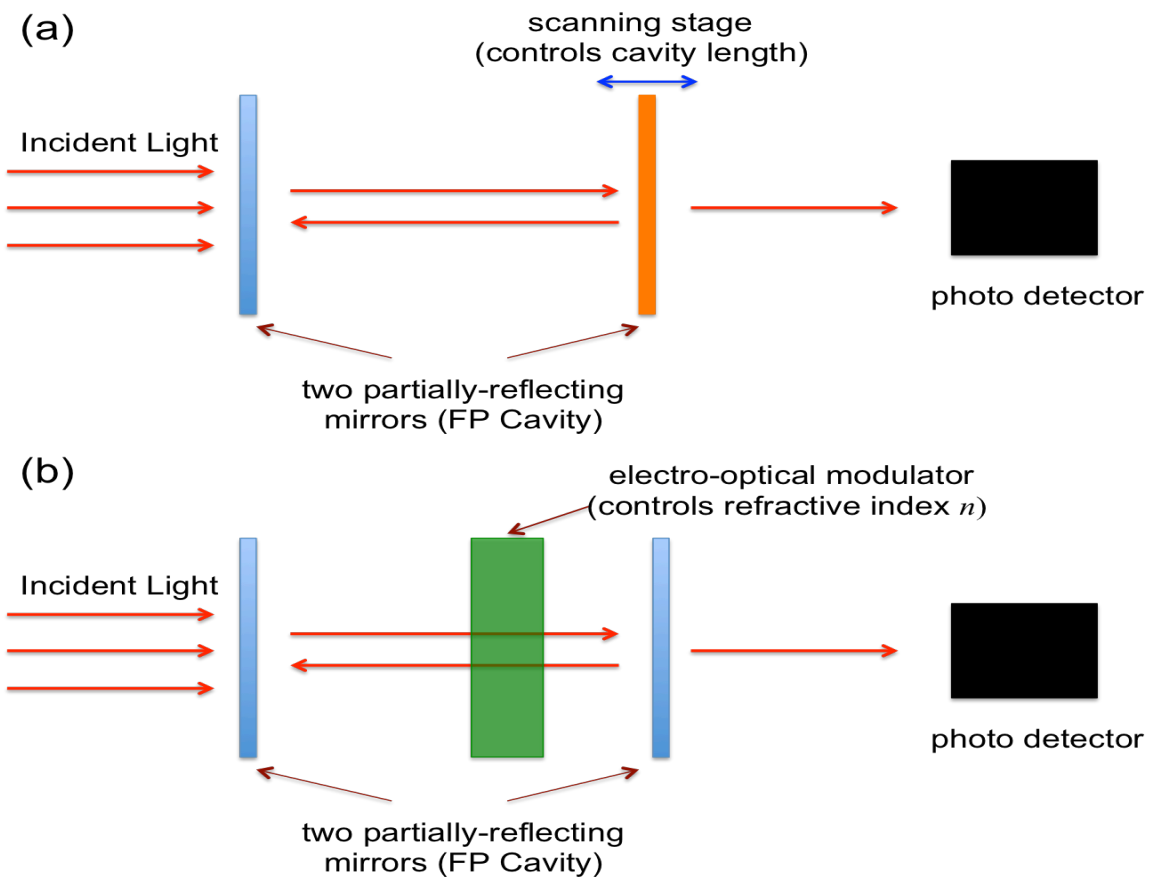

Figure 5-1：Schematic of optical spectrometer based on a Fabry-Perot interferometer by scanning one of the reflecting mirror (a) or adding an electro-optical modulator (b)

A Fabry-Perot interferometer or etalon is made of two reflecting surfaces. It is named after Charles Fabry and Alfred Perot, who developed this instrument in 1899. Its transmission spectrum is a function of wavelength and effective index. The separation between two reflective surfaces (l) and its effective refractive index (n) introduce a fixed phase offset in the wavefront between each reflection. When these reflected beams recombine, only wavelengths that satisfy certain conditions can be transmitted, and the condition is

$$m\lambda = 2nl\cos\theta$$

where m is an integer and θ is the refracted angle in the FP etalon. As we can see from the equation, the transmitted peak wavelength (λ) will change as the refractive index (n) or FP cavity length (l) changes. Therefore, a spectrometer based on a FP interferometer can be mainly achieved in two ways. Fig. 5-1 (a) shows the first method which is based on scanning one of the reflective mirrors. By controlling the cavity length (l), only the wavelength we are interested in can be transmitted through the FP cavity. We can then know the spectrum of the incident light by measuring the output power under different cavity lengths. Similarly, Fig. 5-1 (b) shows the other method realized by fixing the cavity length but adding an electro-optical modulator inside the cavity to control the refractive index (n). According to the equation, we can also control the output peak wavelength by changing the refractive index (by controlling the electro-optical modulator) to get the incident light's spectrum.

(2) Fourier transform spectrometer

A typical example of a Fourier transform spectrometer is based on a Michelson interferometer. It is basically a Michelson interferometer with a movable mirror. Using a

beam splitter, a half-silvered mirror for example, light from the source is split into two beams. One is reflected from a fixed mirror and the other is reflected from a movable mirror that introduces a time delay and an optical path difference (OPD). After reflection, the two beams are recombined at the beam splitter and sent to a detector. The beams interfere, allowing the temporal coherence of the light to be measured at each different time delay setting, effectively converting the time domain into a spatial coordinate. By making measurements of the signal at many discrete positions of the movable mirror, the spectrum can be reconstructed using a Fourier transform of the temporal coherence of the light. Fig. 5-2 shows the schematic image of a Fourier transform spectrometer based on a Michelson interferometer.

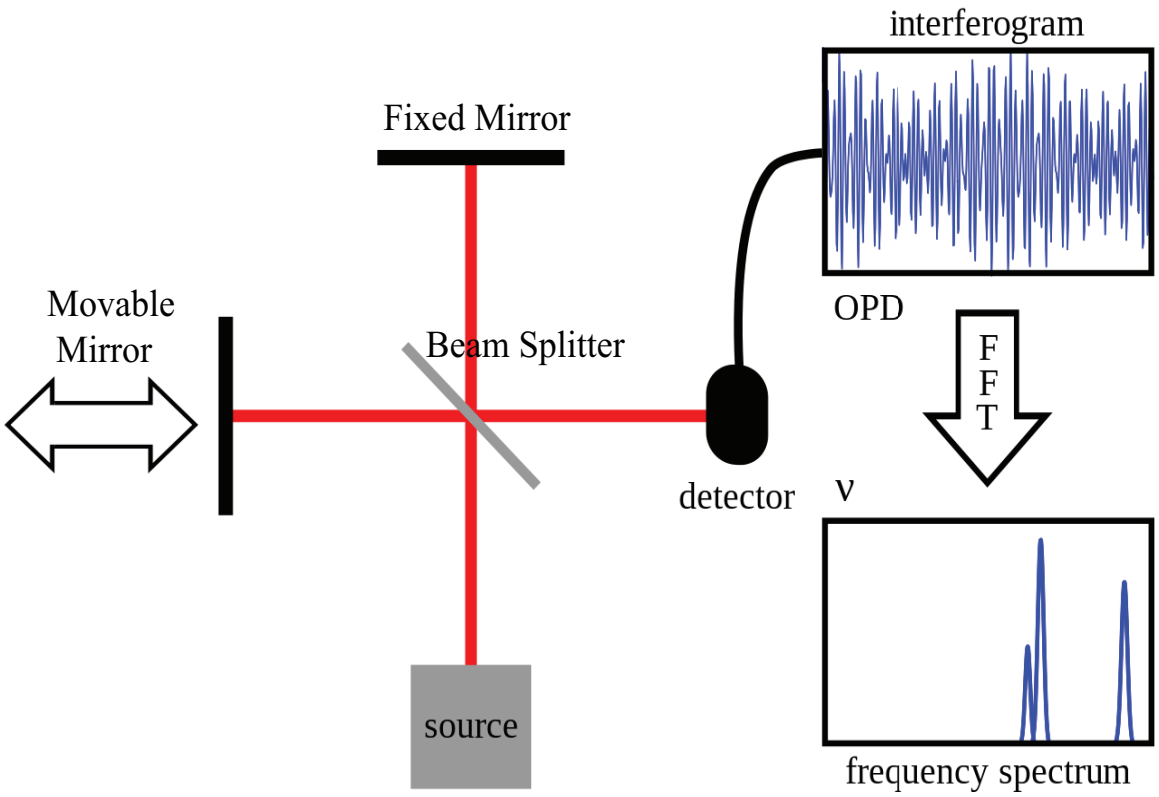

Figure 5-2: Schematic of Fourier Transform spectrometer

(3) Dispersive optical spectrometer

Among all kinds of spectrometers, dispersive spectrometers are by far the most common and important in optical (UV, visible and IR) astronomy. A dispersive spectrometer is a spectrometer that uses some dispersive elements, a prism or diffraction grating for example, to spread the light out in wavelength and get an intensity distribution as a function of wavelength.

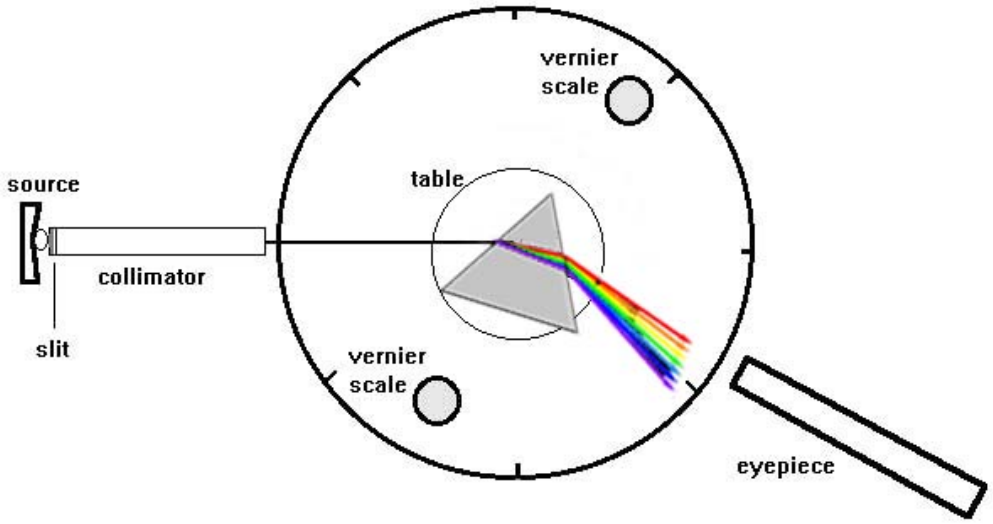

Figure 5-3: Schematic of a typical prism spectrometer

Perhaps the simplest form of a dispersive spectrometer is a prism. The prism refracts light into its different wavelengths. The dispersion occurs because the refractive index of the prism's material is wavelength dependent rather than a constant, so the angle of refraction is different for each wavelength. Fig. 5-3 shows a typical prism spectrometer. Light is emitted from a source such as a vapor lamp. A slit selects a thin strip of light that passes through the collimator. The collimated light then passes through the prism and is refracted twice (when entering and leaving). This leads to a spectrum

that is observed at different angles. The prism is placed on a rotatable stage with vernier scale, which is used to control the refraction angle.

Another type of dispersive spectrometer uses a diffraction grating, which has been in use in astronomical spectroscopy for many decades. These have typically been of the transmission or surface reflecting types and generally consist of parallel lines "ruled" on a reflecting surface or small "steps" on a reflecting or transmitting surface. Nowadays, gratings can be made with much higher accuracy than before by using photolithography or electron-beam lithography.

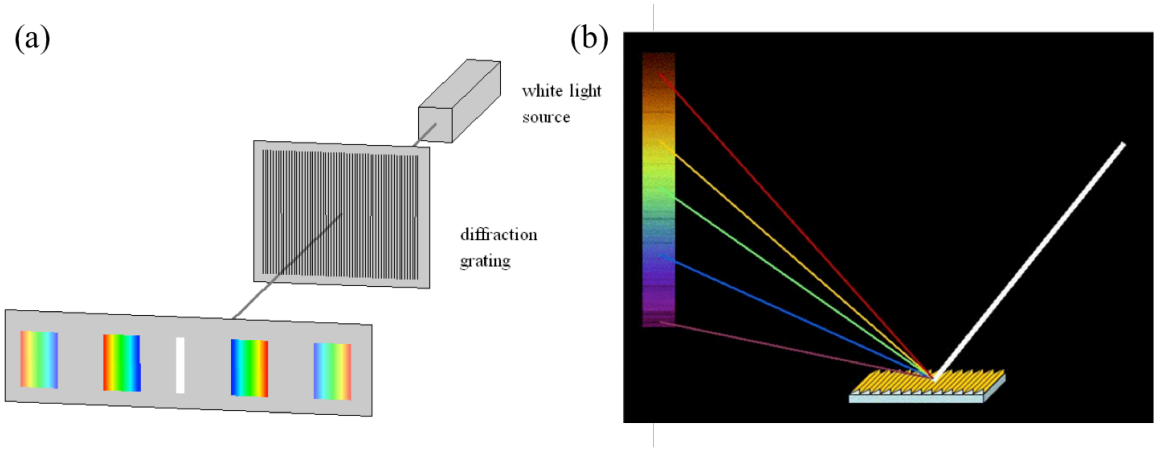

Figure 5-4: Schematic of a diffraction grating: (a) transmitting type; (b) reflecting type

Fig. 5-4 shows a brief schematic image of the two most common diffraction gratings. Fig. 5-4 (a) shows a typical transmission dispersive grating. Light from a broadband source (such as a white light) passes through a transmission grating (multiple thin slits for example) and then leads to a diffraction pattern with multiple orders on the screen. The main order in the center does not have the dispersive ability, while the higher orders on both sides of the main order show the ability for dispersion but with less light intensity. Similarly, Fig. 5-4 (b) shows a typical diffraction grating based on reflection.

Unlike using multiple transmitting slits, light will get reflected and diffracted on gratings such as blazed gratings and then a dispersive spectrum is obtained. The echelle grating that we mainly focus in this thesis is one special type of the reflecting diffraction grating, which we will discuss in more details in the later sections.

5.14 The Rise of Astrophotonics

Astrophotonics is a new area where photonics and astronomy are combined. Nowadays, both fiber and on-chip photonics have been improved quite a lot, new devices based on filters and spectrometers can achieve very high resolution, low loss and also maintain a very compact size. When applying these great new technologies of photonics to modern astronomy, a new revolution is coming.

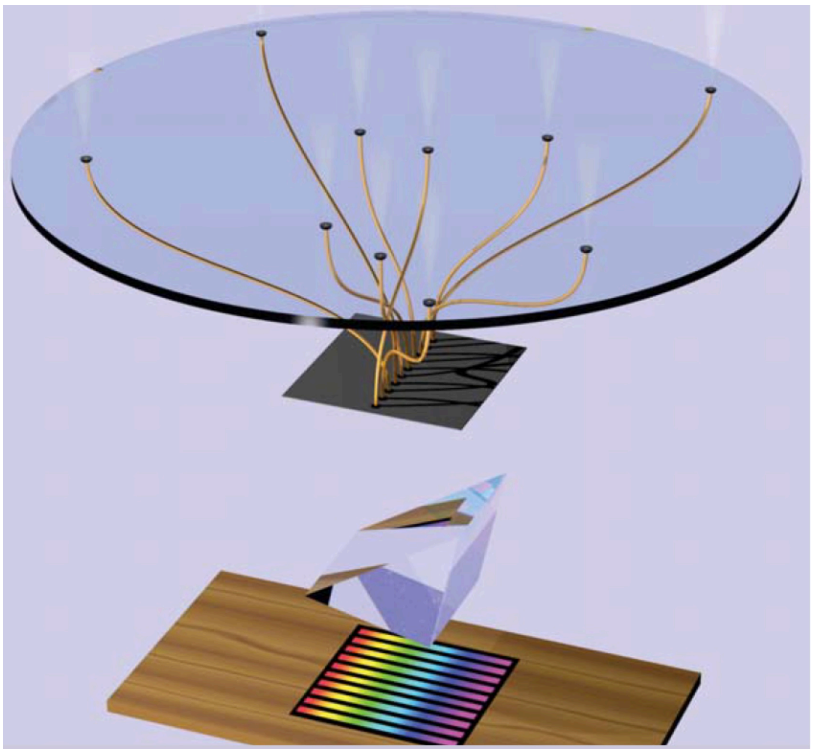

Figure 5-5: Application of optical fibers to observe multiple celestial sources [22]

Astronomical telescopes were typically used just to concentrate the light from one celestial source at a time. But after high quality fiber was made around 1970, astronomers started to realize that optical fibers could be used to observe multiple celestial sources simultaneously: one fiber for each source (see Fig. 5-5 [22]). As shown in Fig. 5-5, spectra of many stars or galaxies can be obtained simultaneously in a single field of view by aligning the entrance apertures of optical fibers with the images of individual sources in a telescope's focal plane. The fibers' downstream ends line up along an aperture in a slit for the spectrographic diffraction elements (a prism or diffraction gratings) that creates separate parallel spectra for different sources [22]. Since the 1990s multi-fiber spectrographs have had a great impact on stellar astronomy and cosmology by providing detailed spectra of more than a million stars and galaxies [23, 24]. More recently, individual fibers have been replaced by closed packed fiber bundles to obtain spatially resolved spectral information across the face of each galaxy in a survey of more than 10 thousand galaxies [25].

Multi-mode fibers (MMF) have been used in astronomy for decades. Because astronomical sources are usually faint, the larger apertures of MMF are preferred over smaller single-mode fibers (SMF) because of their greater coupling to light at the focal plane. However, the inherent modal noise and intermodal dispersion of multi-mode fibers limit their applications in some of the highest resolution spectrographs. Also, a diffraction-limited slit would have very poor throughput when simply connected with a MMF. In these cases, the use of SMF is preferred. In order to use a SMF and achieve great light coupling at the same time, the photonic lantern was introduced to solve the problem perfectly.

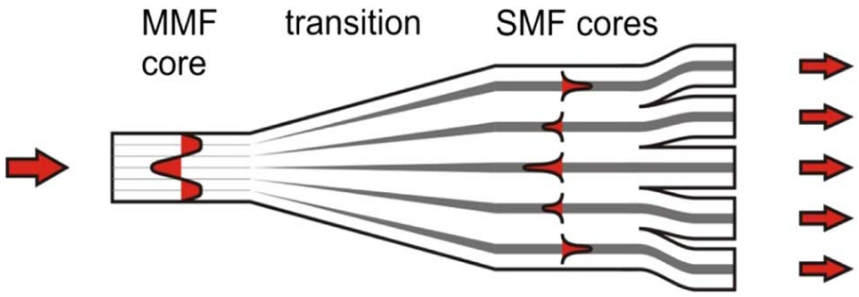

Figure 5-6: Schematic of a typical photonic lantern [26]

The photonic lantern is a low-loss optical device (can be based on both fibers or on-chip waveguides) that connects one multimode core to several cores that each supports fewer modes or only single mode. The photonic lantern comprises an array of isolated SMF cores as a degenerate multimode system, in which the near-diffraction limited spatial modes are the supermodes of the array. The number of degenerate supermodes is equal to the number of cores, and their propagation constants equal that of the mode of a single core in isolation. Light can be coupled between the array of SMFs and a MMF via a gradual taper transition. If the transition is adiabatic, then the *m* degenerated supermodes of the SMF array evolve into the *m* modes of the MMF core, and vice versa. Fig. 5-6 shows the schematic of a photonic lantern made by tapering a bundle of SMFs. Separate SMFs are fused together to form a single glass body, which simultaneously reduces in cross sectional scale to form a MMF core and is surrounded by a low-index jacket that forms a cladding [26].

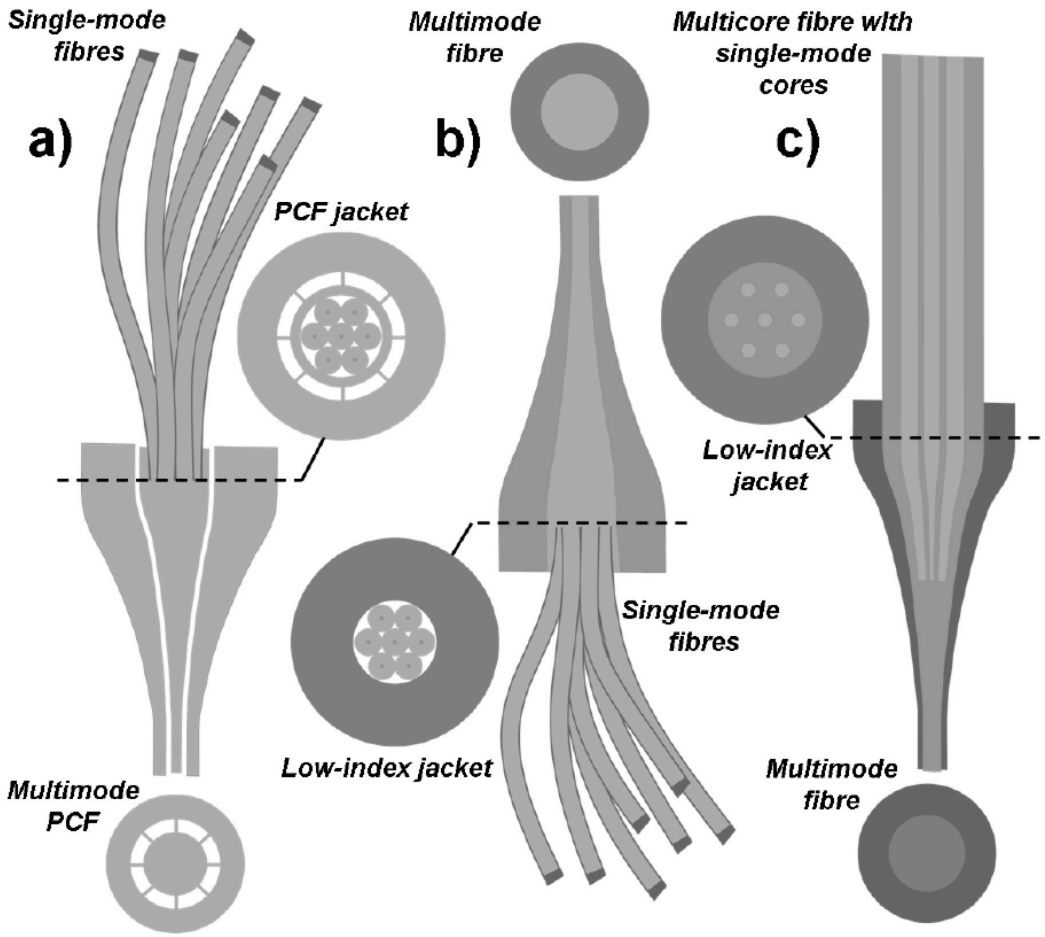

Figure 5-7: Three fabrication methods for fiber based photonic lanterns [27]

There are multiple methods to fabricate the photonic lantern. For an optical fiber based photonic lantern, usually there are three ways to fabricate them (shown in Fig. 5-7). The first method, as shown in Fig. 5-7 (a), is interfacing SMFs to photonic crystal fibers (PCFs) [28]. Fig. 5-7 (b) shows the second method, which is a solid all-glass version. A bundle of SMFs were inserted into a low index glass capillary tube which was then fused and tapered down to form a MMF at the other end [29]. These two methods are similar to some extent, in both cases the single-mode cores are reduced in size and adiabatically change to the multi-mode core which is confined by a second, outer cladding. The third method, which is shown in Fig. 5-7 (c), uses a multicore fiber with an array of identical

single-mode cores. It is made by tapering such a multi-core fiber while placing a low refractive index jacket around the fiber to form the cladding of the MMF [30].

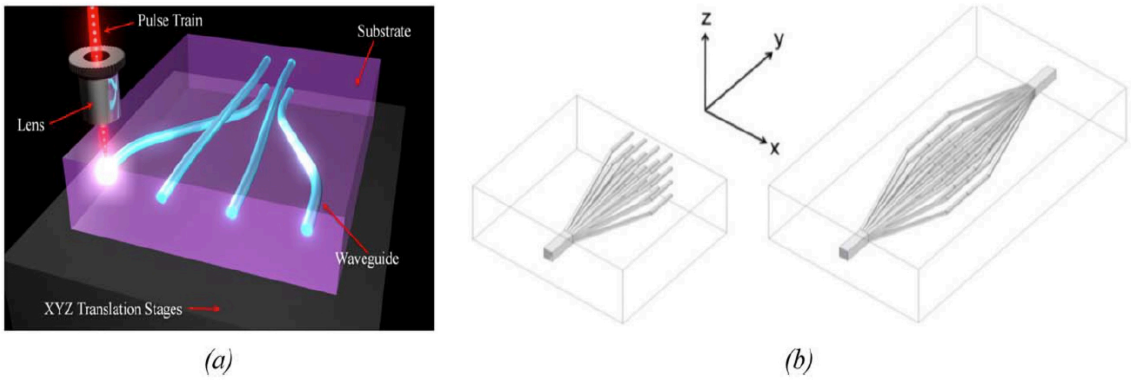

Figure 5-8: Schematics of photonic lantern based on on-chip waveguides [26, 31]

In addition to the fiber based photonic lanterns, a directly written integrated waveguide chip can also be used to make the photonic lantern. As shown in Fig. 5-8 (a), the on-chip photonic lantern is made by direct ultrafast laser inscription (ULI) of a pattern of waveguides using a focused femtosecond laser beam. Fig. 5-8 (b) shows multi mode (MM) to single mode (SM) integrated photonic lantern transition (left), and a MM to SM to MM transition by combining two photonic lanterns in a back-to-back configuration [31].

In addition to photonic lantern, many exciting successes have been achieved in astrophotonics such as [32]: (1) planar waveguides to combine signals from widely spaced telescopes in stellar interferometry; (2) frequency combs for ultra-high precision spectroscopy to detect planets around nearby stars; (3) ultra-broadband fiber Bragg gratings to suppress unwanted background; (4) planar waveguides to miniaturize astronomical spectrographs; (5) large mode area fibers to generate artificial stars in the upper atmosphere for adaptive optics correction; (6) liquid crystal polymers in optical vortex coronagraphs and adaptive optics systems.

5.2 Introduction to Echelle Grating Spectrographs

Historically, astronomy that uses the wavelength range from 0.3um to 1um has progressed more rapidly because this range has much lower intensity of background noise. However, there is much larger background noise for near infrared wavelengths in the range from 1 to 2um. Also, it is usually very expensive and difficult to send large telescopes into the universe by satellite. So very large telescopes such as the Keck telescope (a 10m telescope in Hawaii) and European Extremely Large Telescope (ELT) (39.3m in diameter) can only be built on earth. On the other hand, these large telescopes have some major problems in the near infrared wavelength range. The OH radicals in a cold layer of 6-10 km thickness at altitude of 90km in the atmosphere emit a lot of near infrared light that dominate the background noise at this wavelength range.

Recently, a new technique using ultra-broadband fiber Bragg gratings was developed to suppress this unwanted background noise. Thanks to this new development and the use of the photonic lantern, we are trying to build the world's first fully integrated photonic spectrograph, which is optimized for faint passive light sources in this near infrared wavelength region.

Fig. 5-9 shows the schematic image of a typical spectrographic system for astronomical application. A photonic lantern first collects the light from the telescope, and then the ultra-broadband Bragg gratings are used to suppress the background noise emitted by the OH radical in the atmosphere. The filtered light guided by SMFs then reflects from or passes through diffraction elements, such as a prism or diffraction gratings, and is detected by a spectrographic CCD array afterwards. The diffraction

gratings are usually arrayed waveguide gratings (AWGs) or echelle gratings. In this thesis, we are focusing in the later one, the echelle grating.

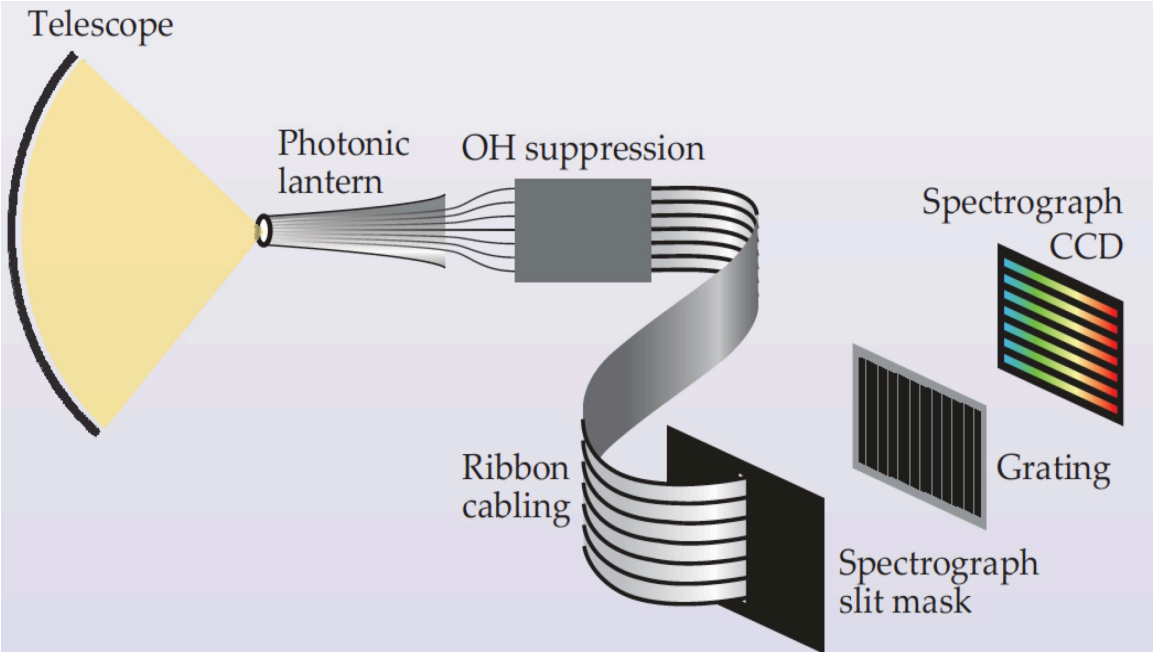

Figure 5-9: Schematic of a typical astronomical spectrographic system [22]

An echelle grating is a type of blazed grating that usually has high incidence angles and is optimized for high diffraction orders. While a blazed grating is a special type of diffraction grating, it is optimized to achieve maximum grating efficiency in a given diffraction order. As we discussed before, for conventional multi-slit diffraction grating, the main order has the maximum power but has no diffraction ability. The higher orders have the diffraction ability but with less light intensity. For a spectrograph in astronomical applications, we hope to achieve a low-loss optical system since most of the celestial objects we are interested in are very faint. Therefore, we hope that the diffraction grating can achieve high diffraction ability with high grating efficiency simultaneously. Blazed grating can solve this problem. In this case, maximum optical power is

concentrated in the desired diffraction order while the residual orders, particularly the 0^{th} order, is minimized.

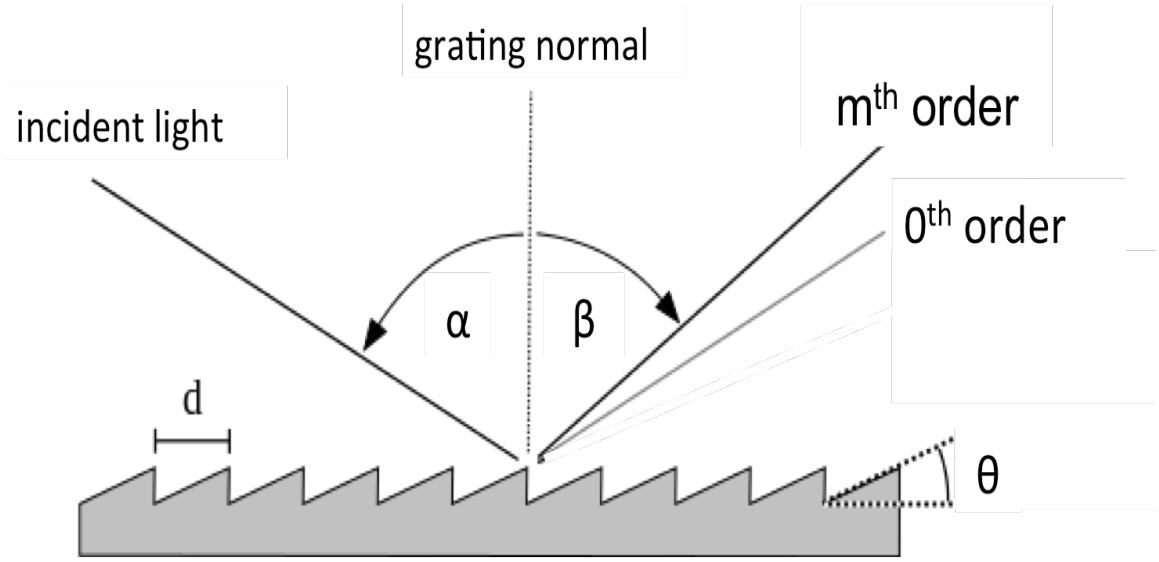

Figure 5-10: Schematic of a typical blazed grating

Fig. 5-10 shows the schematic image of a typical blazed grating. As we can see from the image, the gratings are blazed with certain angle (θ), and the incident angle (α) and the diffraction angle (β) for the m^{th} order diffraction are measured relative to the grating normal. The separation of the periodic grating lines (d) is called the grating constant. The constructive interference at wavelength λ occurs when the path difference between the incident and reflected light is equal to an integral number of wavelengths. This relationship is usually described by the grating equation:

$$m\lambda = d(\sin(\alpha) \pm \sin(\beta))$$

where m is an integer representing the diffracting order. The direction in which maximum efficiency is achieved is determined by the blaze angle (θ).

Given the grating equation shown above, and the fact that the angle of incidence, α, is a constant, then differentiating the grating equation gives the angular dispersion of the grating:

$$\frac{\Delta\beta}{\Delta\lambda} = \frac{m}{d\ \cos\beta}$$

Based on this equation, we can clearly see that the angular dispersion is proportional to the order (m) and inversely proportional to the grating period (d). Therefore, the echelle grating, a type of blazed grating with a large blaze angle that can operate on high diffraction orders, has a much higher angular dispersion than common blazed gratings.

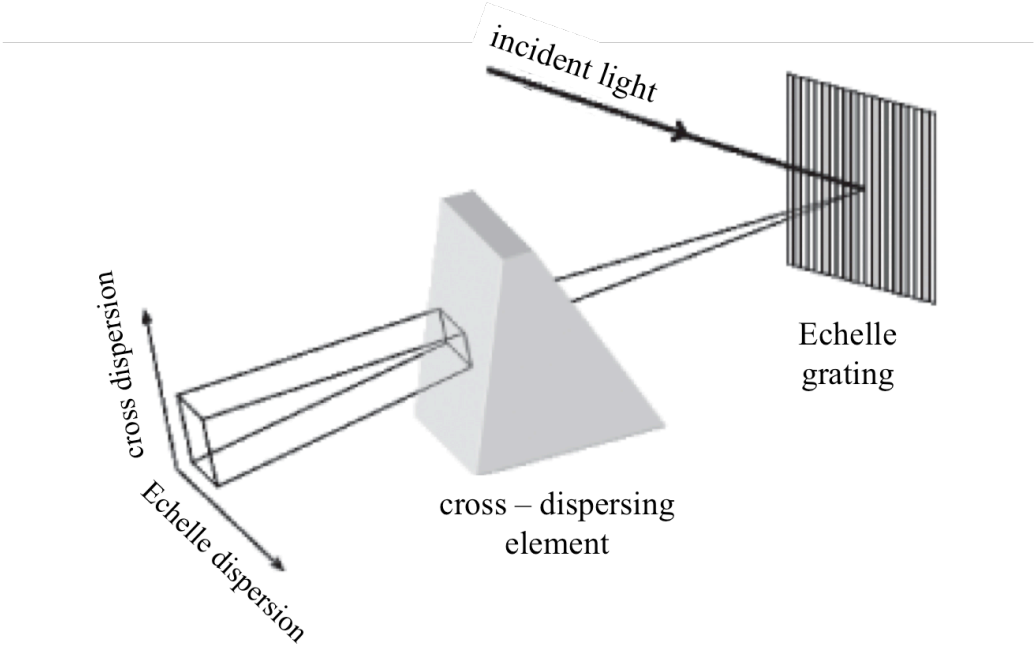

Figure 5-11: Schematic of the cross dispersion in echelle spectrograph

Although operating at higher order can achieve larger angular dispersion, the free spectral range (FSR, defined as the change in wavelength from an order m to the nearby, m ± 1, order) is getting smaller as the order goes higher. In this way, for Echlle gratings

working at very high orders, each channel may have noise signals from nearby orders. In order to separate signals from different orders in the same channel and to get a much broadband spectrum, a technique called “cross dispersion” is usually applied that will disperse the spectrum in a direction that is orthogonal to the main echelle dispersion. This second dispersive element can be a prism, a diffraction grating or a combination of them.

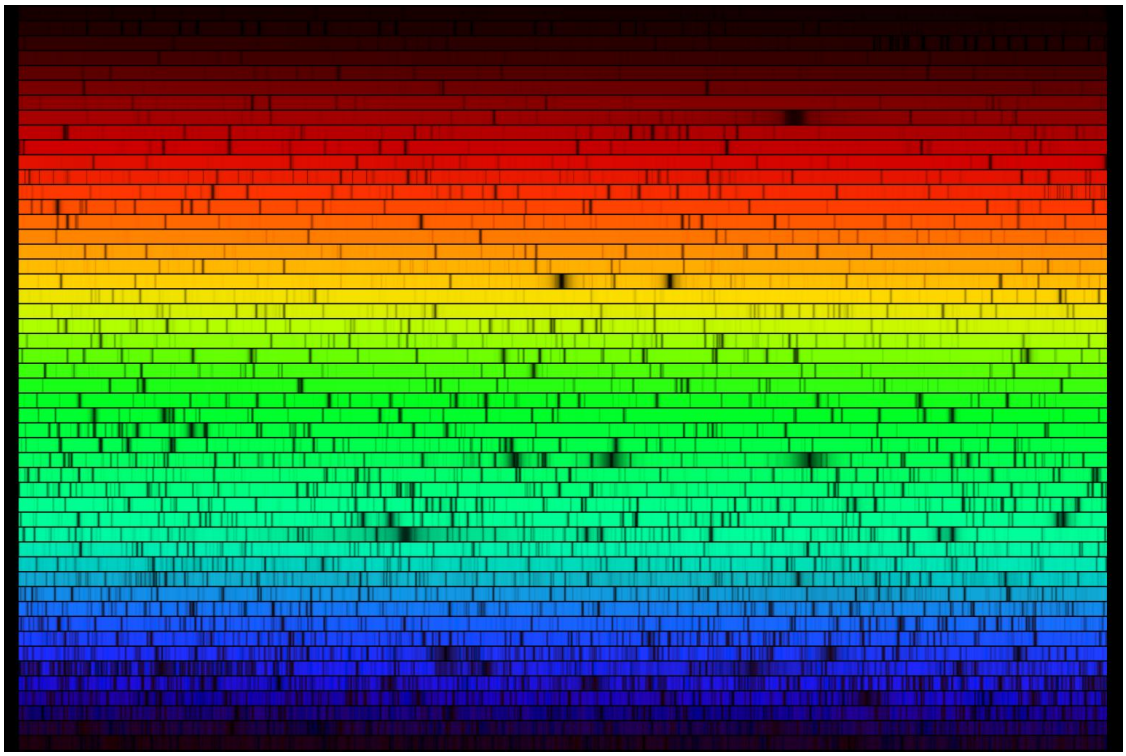

Figure 5-12: Schematic of the 2-dimentional echelle spectrum

Fig. 5-11 shows the schematic image of the cross dispersion technique used for an echelle spectrograph. A light is first diffracted from the echelle grating and gets a 1-dimentional spectrum. Then the light passes through a prism (it also can be another diffraction grating) and gets a second dispersion in the orthogonal direction. Therefore, the spectrum becomes two dimensional and is detected by a two-dimensional CCD array.

Fig. 5-12 shows this two-dimensional echelle spectrum. The echelle spectrum of each order is shown in the horizontal direction, while the vertical direction is where each order is split. Instead of using lots of channels such as fibers or waveguides to transfer the output light into different optical detectors, a two-dimensioanl CCD array is used here to detect the output spectrum. And the different pixels located at the different places on the CCD represent the different wavelengths.

Chapter 6 : Design, Simulation and Theoretical Calculation

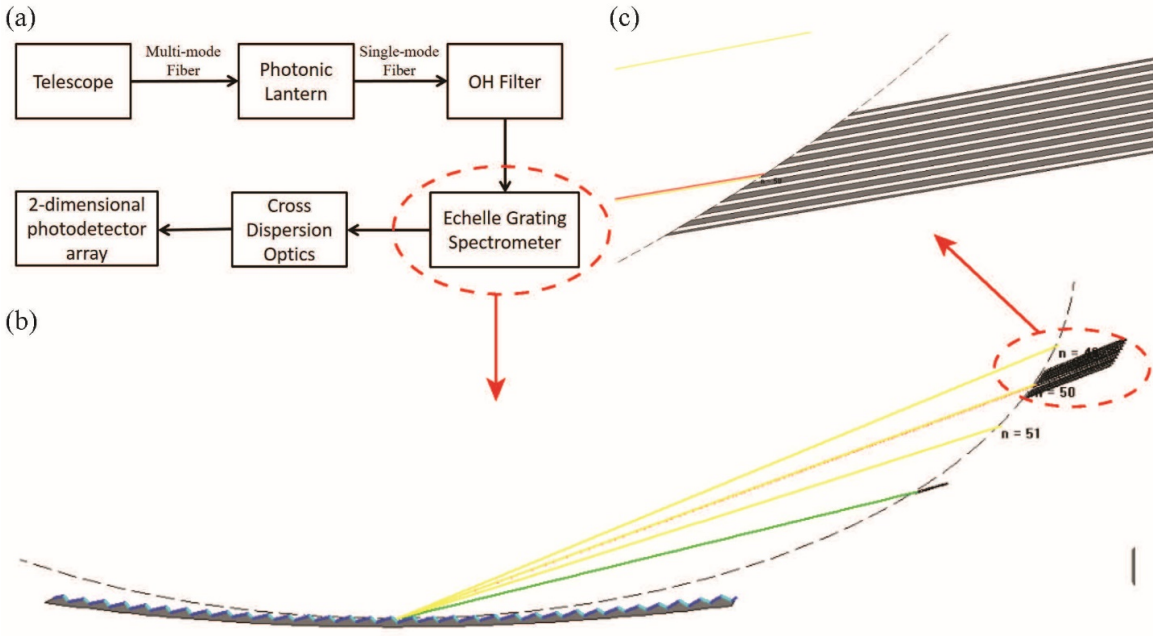

Figure 6-1: (a) schematic workflow of a typical modern astronomical spectroscopic system (b) schematic of an echelle-grating spectrometer, (c) magnified image of the output channels

Fig. 6-1 (a) shows a schematic diagram where a spectrometer is used for astronomical applications. The light collected from the telescope is first coupled into a multi-mode fiber to achieve low coupling loss. And then a photonic lantern is used to couple the light from the multi-mode fiber to a bunch of single-mode fibers. If the telescope is on earth, another filter is needed to suppress the noise wavelengths mainly emitted from the OH bonds in the atmosphere that is very strong compared to the real signal of interest. Then the filtered light is coupled into a spectrometer and we are designing an echelle grating based on-chip spectrometer to achieve this. In order to achieve higher resolution and broader spectrum, the one-dimensional spectrum are usually transferred into a two-dimensional spectrum through some kinds of cross-

dispersive optics and detected by a two-dimensional photodetector array. Here, we are focusing on implementing the echelle-grating spectrometer.

Fig. 6-1 (b) shows a schematic diagram of an echelle-grating spectrometer. The green line is the input and the yellow lines are the outputs of different orders. Fig. 6-1 (c) shows the zoomed image of the major order spectrum, it can be coupled into different output waveguides or simply freely propagates though a cross-dispersion optical component and is detected by a two-dimensional photodetector array.

In the first part of this thesis, we have successfully made an on-chip photonic waveguide for atom light interaction, and we have achieved a high fiber-to-waveguide coupling efficiency for a wide range of wavelengths from 750nm to 1100nm. Here, the echelle grating we are going to build needs to be optimized for the near infrared wavelength range from 1 um to 1.7 um for astronomical applications. Therefore, in order to make a low loss spectrographic system, the first thing we need to do is to design a waveguide (for input and output waveguides of the echelle grating) with high coupling efficiency, low propagation loss, and low bending loss within this wavelength range.

6.1 Input and Output Waveguide Mode Simulation

The wavelength range we are interested is from 1um to 1.7 um. It is a very wide range and we are going to divide it into several separate parts. To begin with, we first design the optical waveguide for a wide wavelength range from 1.45 um to 1.7 um.

The waveguide is made with a silicon nitride core (Si_3N_4, $n_{core} = 2$) and a silicon oxide cladding (SiO_2, $n_{clad} = 1.46$). The substrate is 500 μm p-type {100} single crystal silicon coated with 5μm thermal silicon dioxide. This thick oxide layer works as the lower cladding of the waveguide and also prevents the optical waveguide mode leaking

into the Si substrate underneath. The waveguide core is made with 300nm LPCVD Si_3N_4 and another layer of PECVD SiO_2 makes the upper cladding.

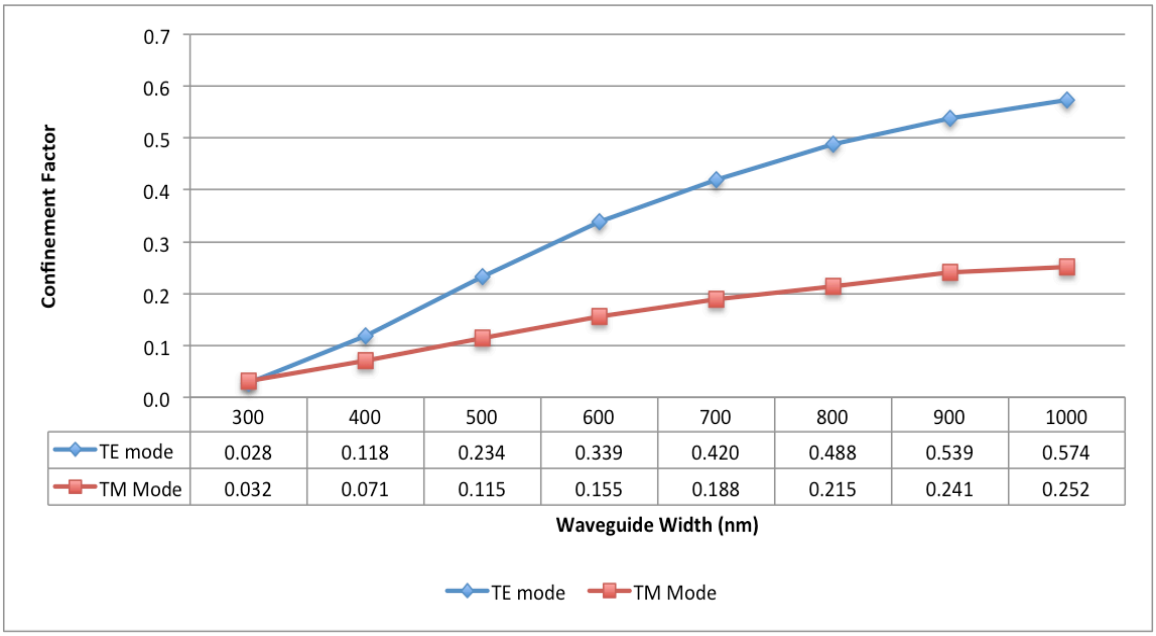

	300	400	500	600	700	800	900	1000
TE mode	0.028	0.118	0.234	0.339	0.420	0.488	0.539	0.574
TM Mode	0.032	0.071	0.115	0.155	0.188	0.215	0.241	0.252

Figure 6-2: Confinement factor of optical waveguide with different widths

In order to design the waveguide with the right size, we simulate the waveguide modes under different widths. For waveguide with thickness of 300nm, we found that the second-order TE mode starts to exist when the width of the waveguide is equal to or larger than 1.1um for 1550nm wavelength. Since we need single mode for all the waveguides, the width of the waveguide should be under 1.1um. Besides, since the echelle grating will potentially be integrated with other on-chip devices such as a Bragg-grating filter, there might be several bending waveguides on the chip. So the waveguide should also be designed with low bending loss. In this way, a comparatively larger confinement factor of the waveguide is preferred.

Fig. 6-2 shows the simulation result for the confinement factors of the 300nm-thick waveguide with different widths at 1550nm wavelength. As can be seen from the plot, the

confinement factor goes higher as the waveguide becomes wider, and the TE modes usually have a larger confinement factor than its corresponding TM mode. In order to get lower bending loss, the wider waveguide is preferred. However, since the 1um * 300nm waveguide has a higher order TE mode at 1450nm wavelength and we are interested in a broad range of wavelength from around 1.45um to 1.7um rather than a single wavelength at 1550nm, 900nm is the largest waveguide width we can choose.

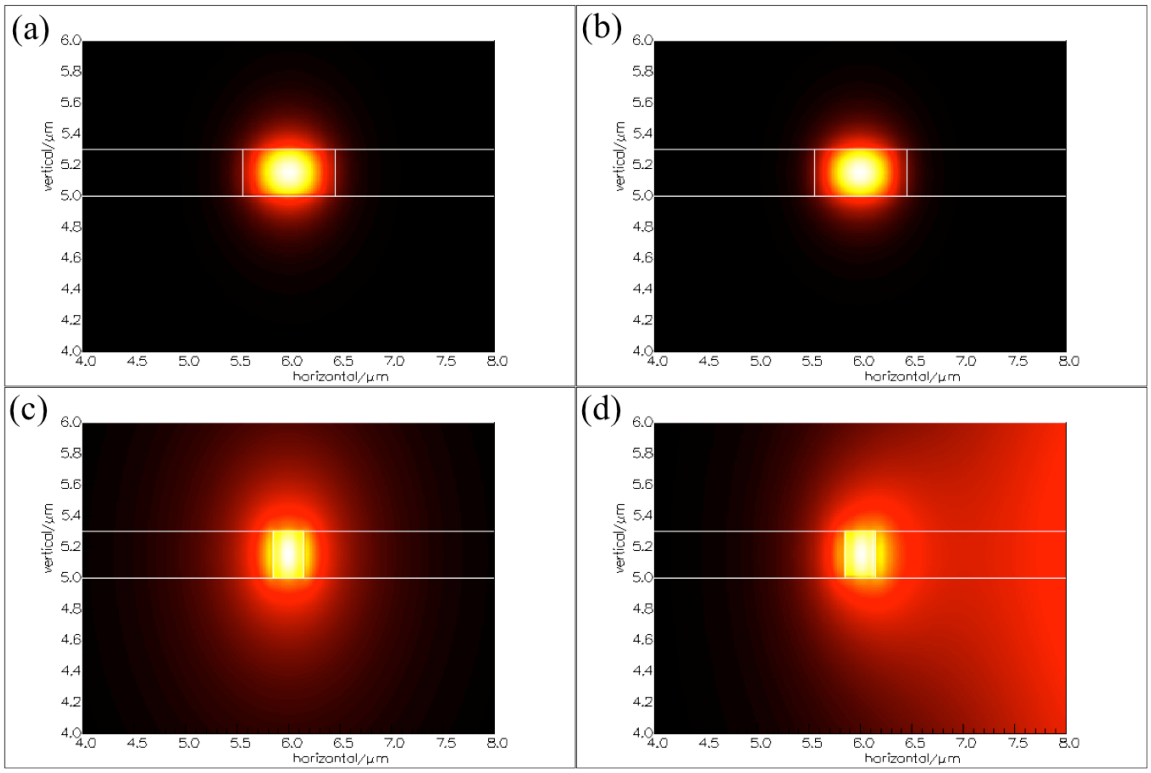

Figure 6-3: (a) TE mode profile of 900nm * 300nm straight waveguide; (b) TE mode profile of 900nm * 300nm bending (r = 200um) waveguide; (c) TE mode profile of 300nm * 300nm straight waveguide; (d) TE mode profile of 300nm * 300nm bending (r = 200um) waveguide

Fig. 6-3 shows the simulated mode profiles for waveguides of different confinement factors with and without bending. Fig. 6-3 (a) shows the TE mode profile for a 900nm wide and 300nm thick waveguide, which is strongly guided mode with a confinement

factor of 0.54. As can be seen from the figure, most of the mode intensity is confined inside the waveguide core. Fig. 6-3 (c) is the TE mode profile for a 300nm wide and 300nm thick waveguide, which is more weakly guided with a confinement factor of 0.028. As we can see from the image, the mode is partially squeezed outside the waveguide core. Usually, a weakly guided mode has larger bending losses under the same bending condition, because a weakly guided mode will be shifted more to the side causing more radiation loss and scattering loss from the waveguide sidewall. Fig. 6-3 (b) and (d) shows the TE mode profiles for these two waveguides under the same bending condition (bending radius = 200 um). The bending mode of the strongly guided waveguide almost does not shift as shown in Fig. 6-3 (b). While the bending mode of the weakly guided mode shift quite a lot towards to the side and most of the light intensity has moved outside the core as shown in Fig. 6-3 (d), which will potentially cause higher bending loss.

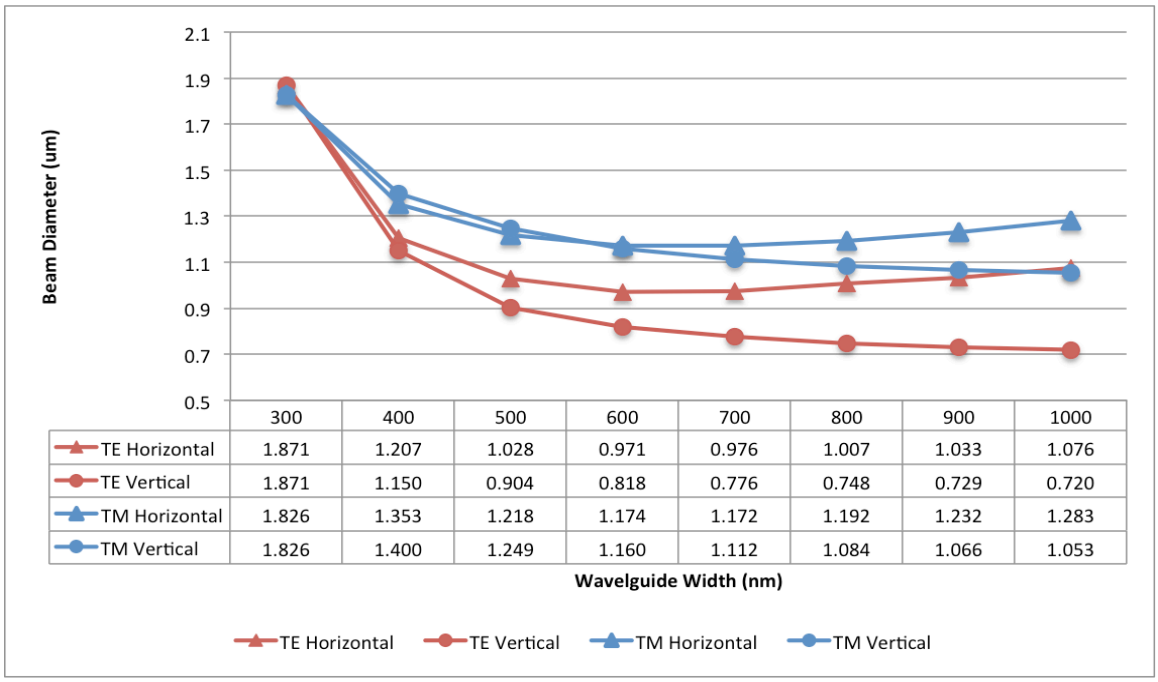

	300	400	500	600	700	800	900	1000
TE Horizontal	1.871	1.207	1.028	0.971	0.976	1.007	1.033	1.076
TE Vertical	1.871	1.150	0.904	0.818	0.776	0.748	0.729	0.720
TM Horizontal	1.826	1.353	1.218	1.174	1.172	1.192	1.232	1.283
TM Vertical	1.826	1.400	1.249	1.160	1.112	1.084	1.066	1.053

Figure 6-4: Beam sizes of optical waveguide with different sizes

Fig. 6-4 shows the simulation results for the beam sizes, where the diameter is measured at the 1/e^2 of the maximum intensity, for the 300nm thick optical waveguide with different widths (from 300nm to 1000nm). As we can see, the beam size is very large when the mode is very weakly guided and the TM mode is usually larger than its corresponding TE mode. For example, the TE mode's beam size for a 300nm wide and 300nm thick waveguide is a circle with diameter of 1.871um, which is much larger than its physical size and its confinement factor is only 0.028. While for a strongly guided mode, the mode size is slowly getting bigger as the waveguide gets bigger. Considering the etching depth to make the echelle grooves is proportional to the beam size of waveguide mode, a large mode size is not preferred since it is difficult to etch a very deep and vertical sidewall. The smallest beam size of the TE mode happens around a width of 700nm, but its confinement factor is only 0.42. As for the 900nm wide waveguide, the mode is similarly small but the confinement factor is much larger. Therefore, we finally choose a width of 900nm and a thickness of 300nm to be our waveguide size.

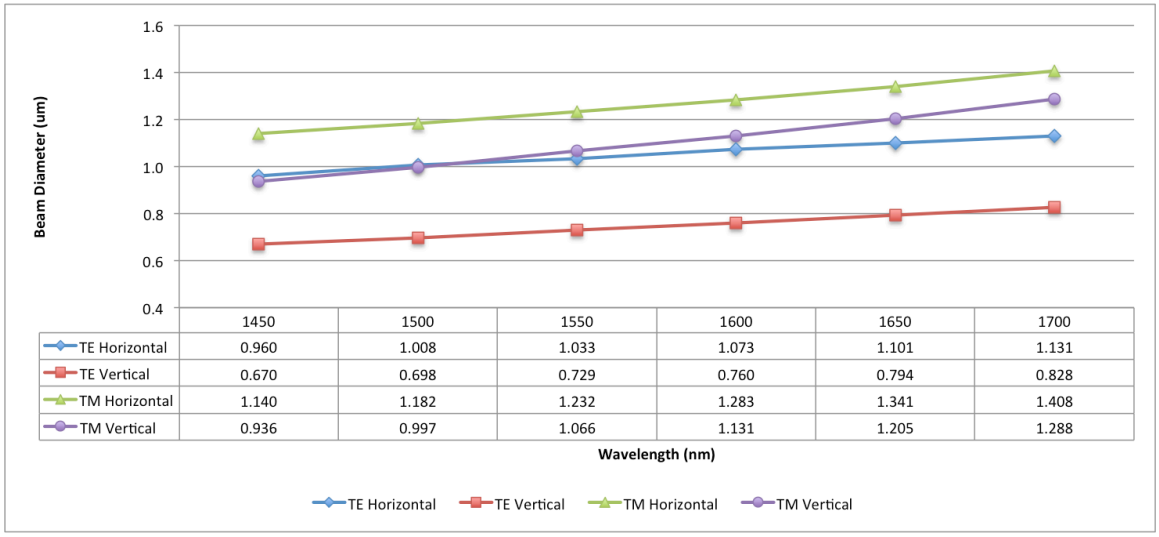

	1450	1500	1550	1600	1650	1700
TE Horizontal	0.960	1.008	1.033	1.073	1.101	1.131
TE Vertical	0.670	0.698	0.729	0.760	0.794	0.828
TM Horizontal	1.140	1.182	1.232	1.283	1.341	1.408
TM Vertical	0.936	0.997	1.066	1.131	1.205	1.288

Figure 6-5: Beam sizes for wavelength range from 1.45um to 1.7um

Since the waveguide is designed for a broad wavelength range from 1.45um to 1.7um, the confinement factor and beam size at other wavelengths should also be considered. Fig. 6-5 shows the simulation results for the beam sizes for a 900nm wide and 300nm thick optical waveguide under wavelength range from 1.45um to 1.7um. As we can see from the plot, the beam size slowly goes larger as the wavelength increases but still remains similar to each other. And Fig. 6-6 is the simulation result for the confinement factors of this waveguide under this wavelength range, which shows that this waveguide is strongly guided for all the wavelengths in this range.

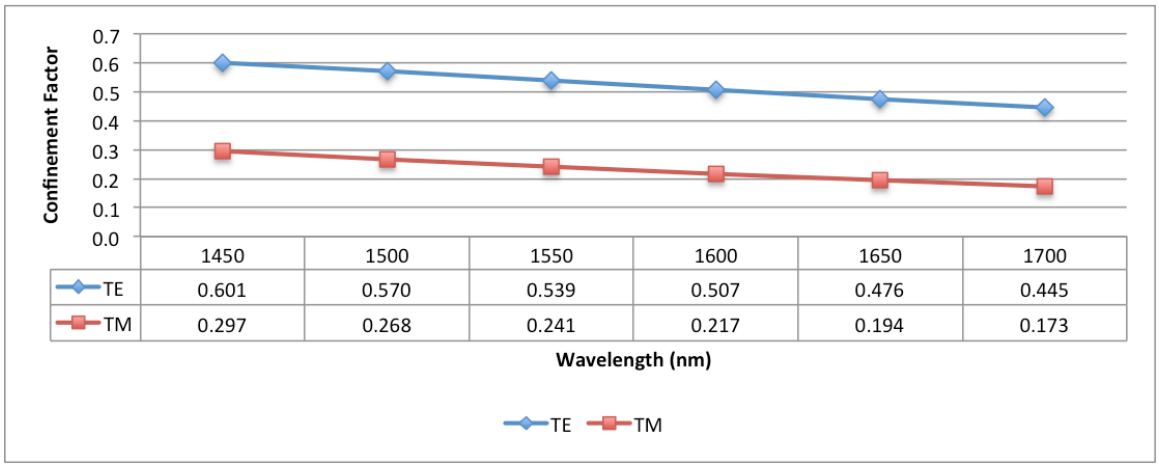

	1450	1500	1550	1600	1650	1700
TE	0.601	0.570	0.539	0.507	0.476	0.445
TM	0.297	0.268	0.241	0.217	0.194	0.173

Figure 6-6: Confinement factors for wavelength range from 1.45um to 1.7um

6.2 Inversed Taper Simulation for high Coupling Efficiency

According to the waveguide mode simulation shown above. The TE mode diameter at 1550nm wavelength is 1.033um in the horizontal direction and 0.729 um in the vertical direction, and the TM mode diameter at 1550nm wavelength is 1.232um in the horizontal direction and 1.066um in the vertical direction. However, this mode size is usually much smaller than the mode size of a commercial single mode fiber. For example, the most commonly used single mode fiber at 1550nm wavelength is Corning SMF-28, this fiber

has a mode-field diameter of 10.4um that is almost 100 times larger than the mode area of our waveguide. According to the mode coupling theory that we discussed in the early chapters, the direct coupling between these two modes will be very low efficient and the coupling efficiency will be only a few percent. Therefore, an inversed taper structure is designed to achieve better fiber-waveguide coupling efficiency.

We choose to use two different fibers to do the fiber-waveguide coupling. The first one is UHNA3 single mode fiber from Thorlabs (designed for wavelength range from 960nm to 1600nm). This fiber has a smaller core size and higher numerical aperture than common single mode fibers, which means a smaller mode size can be achieved. Its core size is 1.8um in diameter with a refractive index of 1.4874, and the refractive index of its cladding is 1.4454. Based on simulation, its mode size is 3.18um in diameter. Compared to the 10.4um mode size of Corning SMF-28, it is much smaller but still larger than our waveguide mode size. Therefore, we designed an inversed taper to improve the fiber-waveguide coupling efficiency.

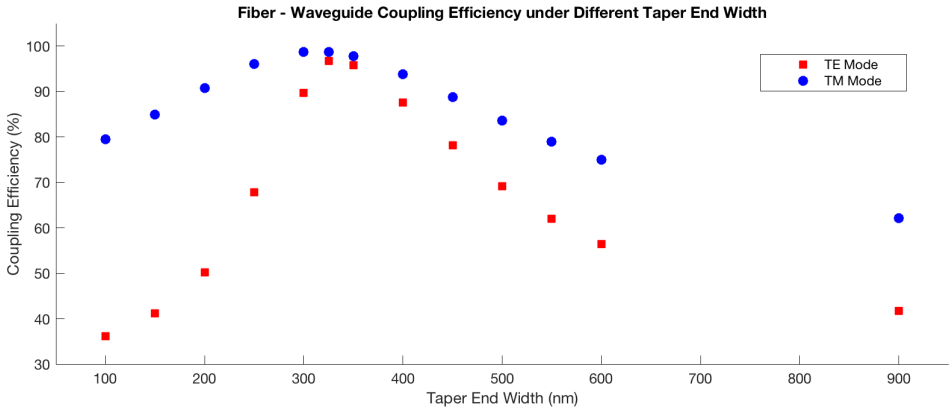

Taper Width (nm)	100	150	200	250	300	325	350	400	450	500	550	600	900
TE Mode (%)	36.21	41.17	50.25	67.86	89.67	96.66	95.74	87.53	78.16	69.22	61.99	56.45	41.78
TM mode (%)	79.47	84.86	90.80	96.05	98.72	98.67	97.73	93.87	88.76	83.64	79.01	75.04	62.13

Figure 6-7: Fiber-waveguide coupling efficiencies under different taper end widths

Fig. 6-7 shows the simulation result of the fiber-waveguide coupling efficiency (per facet) under different taper end widths for 1550nm wavelength. The waveguide is 900nm wide and 300nm thick, and the taper region is 500um long and also has a 300nm thick waveguide core. The taper end width changes from 100nm to 900nm. As we can see from the plot, the maximum coupling efficiency happens at a taper end width of 325nm, which is 96.66% for TE mode and 98.67% for TM mode. This means that at this taper end width, we will get the best mode matching between the fiber mode and the taper mode. We can also tell from the plot that the coupling efficiency for TM mode is usually larger than that for the corresponding TE mode, it is because the TM mode size is usually larger than the TE mode as our previous simulation result shows, which makes the taper's TM mode closer to the fiber mode and will lead to higher coupling efficiency. Since our echelle grating will be designed for a central wavelength at 1550nm, so we choose 325nm as our taper end width because of its best coupling efficiency.

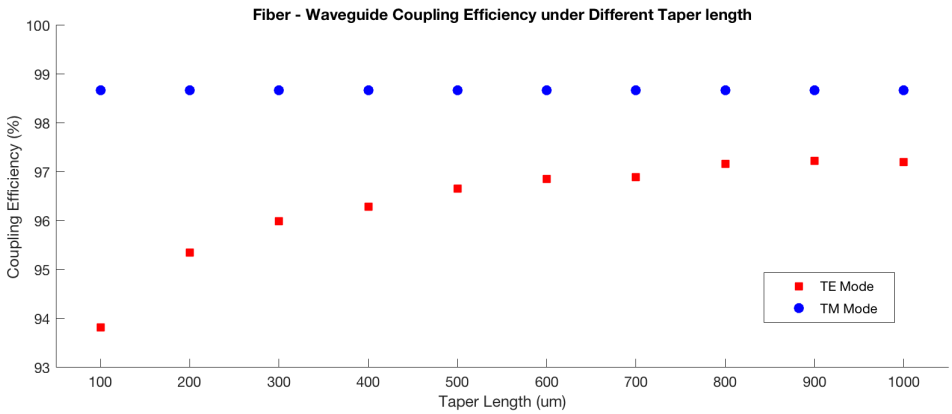

Taper Length (um)	100	200	300	400	500	600	700	800	900	1000
TE Mode (%)	93.82	95.36	96.00	96.28	96.66	96.86	96.90	97.17	97.23	97.21
TM Mode (%)	98.67	98.67	98.67	98.67	98.67	98.67	98.67	98.67	98.67	98.67

Figure 6-8: Fiber-waveguide coupling efficiencies under different taper lengths

In order to reduce the optical loss in the tapered region, the waveguide width in this region should change slowly to achieve the adiabatic condition. Fig. 6-8 shows the simulated fiber – waveguide coupling efficiency (per facet) under different taper length varying from 100um to 1000um. The waveguide width in this region changes from 325nm to 900nm linearly. As we can see from the plot, the coupling efficiency goes higher as the taper becomes longer for both TE and TM mode. The coupling efficiency for TM mode does not change much, while the coupling efficiency for TE mode decrease a little bit more quickly when the taper length goes below 500um. Considering the potential stitching error in EBL and the extra propagation loss of the inversed tapers, the taper length should not be too long. Therefore, we choose 500um as our taper length.

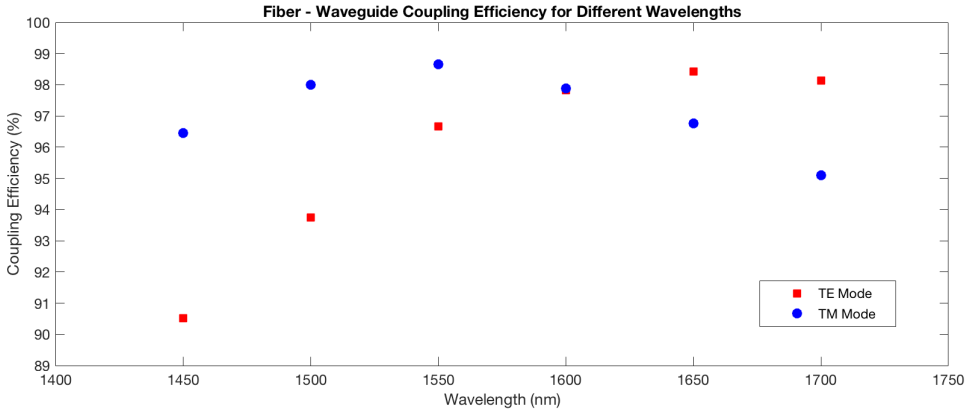

Wavelength (nm)	1450	1500	1550	1600	1650	1700
TE Mode (%)	90.51	93.74	96.66	97.82	98.42	98.13
TM Mode (%)	96.46	97.99	98.66	97.89	96.76	95.09

Figure 6-9: Fiber -waveguide coupling efficiencies for different wavelengths

Since we are interested in a broad wavelength range from 1450nm to 1700nm. We also simulated the coupling efficiency for some typical wavelengths within this range with the inversed taper structure we designed above. Fig. 6-9 shows the simulated fiber – waveguide coupling efficiency for wavelengths (per facet) at 1450nm, 1500nm, 1550nm,

1600nm, 1650nm and 1700nm. As we can see from the plot, for all these wavelengths the coupling efficiency is above 90% for both TE and TM mode, which is very good. This means the inversed taper we designed can achieve very high coupling efficiency for a wide wavelength range from 1450nm to 1700nm.

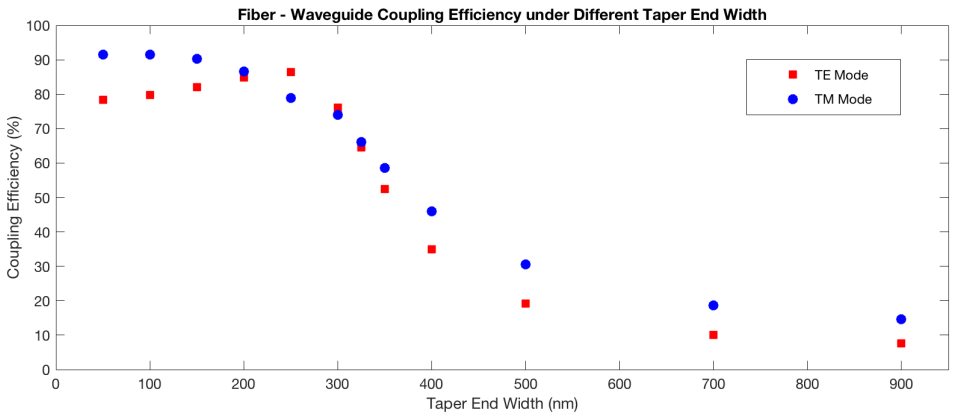

Taper Width (nm)	50	100	150	200	250	300	325	350	400	500	700	900
TE Mode (%)	78.29	79.84	82.05	84.91	86.44	76.07	64.51	52.46	34.99	19.18	10.01	7.55
TM Mode (%)	91.52	91.56	90.34	86.61	78.96	73.94	66.15	58.62	45.97	30.58	18.70	14.68

Figure 6-10: PM fiber-waveguide coupling efficiencies under different taper end widths

The second fiber we may use for the fiber – waveguide coupling is a polarization maintaining single mode fiber (PM fiber) designed for this wavelength range. Since we sometimes measure the polarization dependent information from the echelle grating and the waveguides, it is easier to use a PM single mode fiber. The core size of this PM fiber is 8.5um in diameter with a refractive index of 1.449393, and the refractive index of its cladding is 1.444023. The simulation shows the beam size for this PM fiber is 9.6um in diameter. Compared to the UHNA3 single mode fiber, this PM fiber has a much lower numerical aperture, but with a much larger beam size and core size. Therefore, the direct coupling between this PM fiber and the waveguide is very low, which is 7.55% for the TE mode and 14.68% for the TM mode (simulation result as shown in Fig. 6-10)

Fig. 6-10 shows the simulated coupling efficiency between this PM fiber and the optical waveguide with an inversed taper under different taper end width at 1550nm wavelength. Since the fiber mode size is much larger than UHNA3 single mode fiber, so when the taper end width equals to 325nm (the optimized taper end width for UHNA3) the coupling efficiency is only 64.51% for the TE mode and 66.15% for TM mode. For this PM fiber, the optimized taper end width for the TE mode is 250nm, the optimized taper end width for the TM mode is 100nm, and the optimized taper end width for both TE and TM mode is 200nm.

6.3 Echelle Grating Simulation

We are going to fabricate echelle gratings to build our on-chip spectrometer. To start with, we first focused on small wavelength range with a central wavelength at 1550nm. A simulation software named Epipprop from Photon Design was used to simulate the echelle Grating structure.

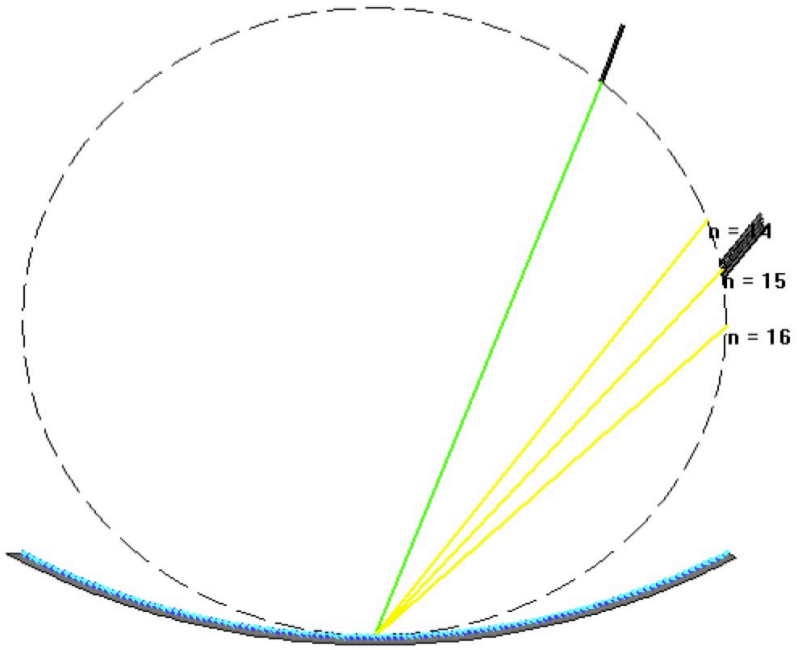

Figure 6-11: Simulation layout of echelle grating in Epipprop

Fig. 6-11 shows the schematic diagram of the simulation layout for echelle Grating in the software. This simulation is based on a template called "Rowland Circle", the inner circle which is shown as the dash line circle is where the input and output waveguides start, its radius is R. The blue arc underneath which is tangential with the inner circle is where the echelle grating is located, and the radius of the arc is 2*R. The green line is the schematic incident light which come from the input channel. The light shines on the gratings and diffracted into different diffraction orders as shown by the yellow lines (here we only show 3 orders of them). The maximum intensity of the diffracted light is designed at the 15^{th} order in this case, which is shown at the output channels (here we only start with five output channels).

We first recall the grating equation:

$$m\lambda = d\,(\sin(\alpha) \pm \sin(\beta)),$$

and its angular dispersion equation:

$$\frac{\Delta\beta}{\Delta\lambda} = \frac{m}{d\,\cos\beta}.$$

We can tell from these equations that the grating's dispersive ability is proportional to its designed order and inversely proportional to its grating period. Also, since we are using the "Rowland Circle" template to simulate the echelle gratings, the radius of the Rowland circle also plays an important role in the design. Therefore, we are going to simulate how echelle gratings are dependent on its designed order, grating period, radius of the "Rowland Circle", and the total length of the gratings.

(I) The effect of the total length of grating

As we can see from the simulation layout, both the input and output waveguides start at the edge of the "Rowland Circle", and inside the circle the light will propagate "freely" without being guided by waveguides. Therefore, unlike a single line shown as the green line in Fig. 6-11, the light will greatly disperse in the horizontal direction and shine almost everywhere on the gratings. In this way, if the total length of the gratings is too small, we will lose part of the light since the incident light cannot "see" the gratings. So the grating region must be long enough to diffract as much light as possible. However, considering the fabrication cost, we usually consider the total length of the gratings to be large enough when it is larger than the horizontal wavefront diameter (1/e^2 of the maximum intensity) of the before-grating wavefront (the wavefront of incident light after free propagation right before touching the gratings).

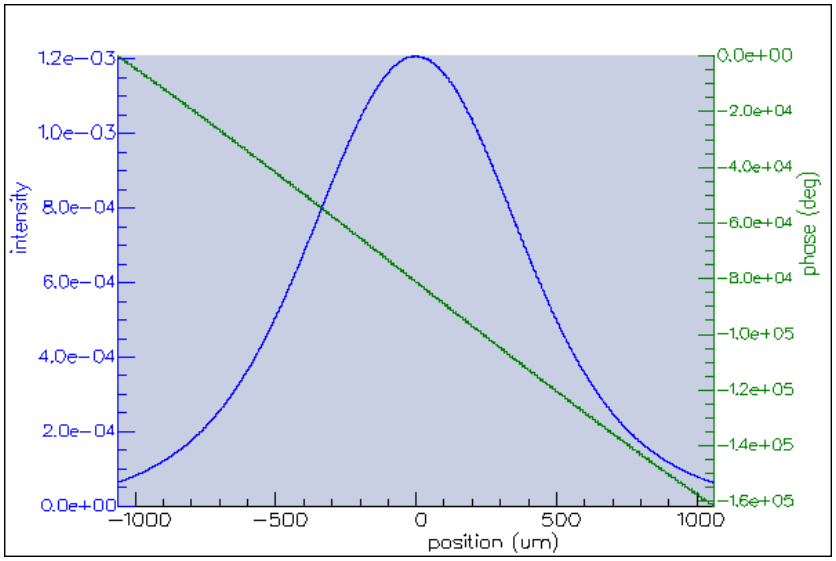

Figure 6-12: Before-grating wavefront profile, the light intensity at different positions of the grating grooves when the incident light reaches the grooves

Fig. 6-12 shows the simulated before-grating wavefront profile for an echelle grating with the Rowland-circle radius of 800um. The 1/e^2 of the maximum intensity is 1.6e-04, as shown in this plot the length of the gratings should be larger than 1600um.

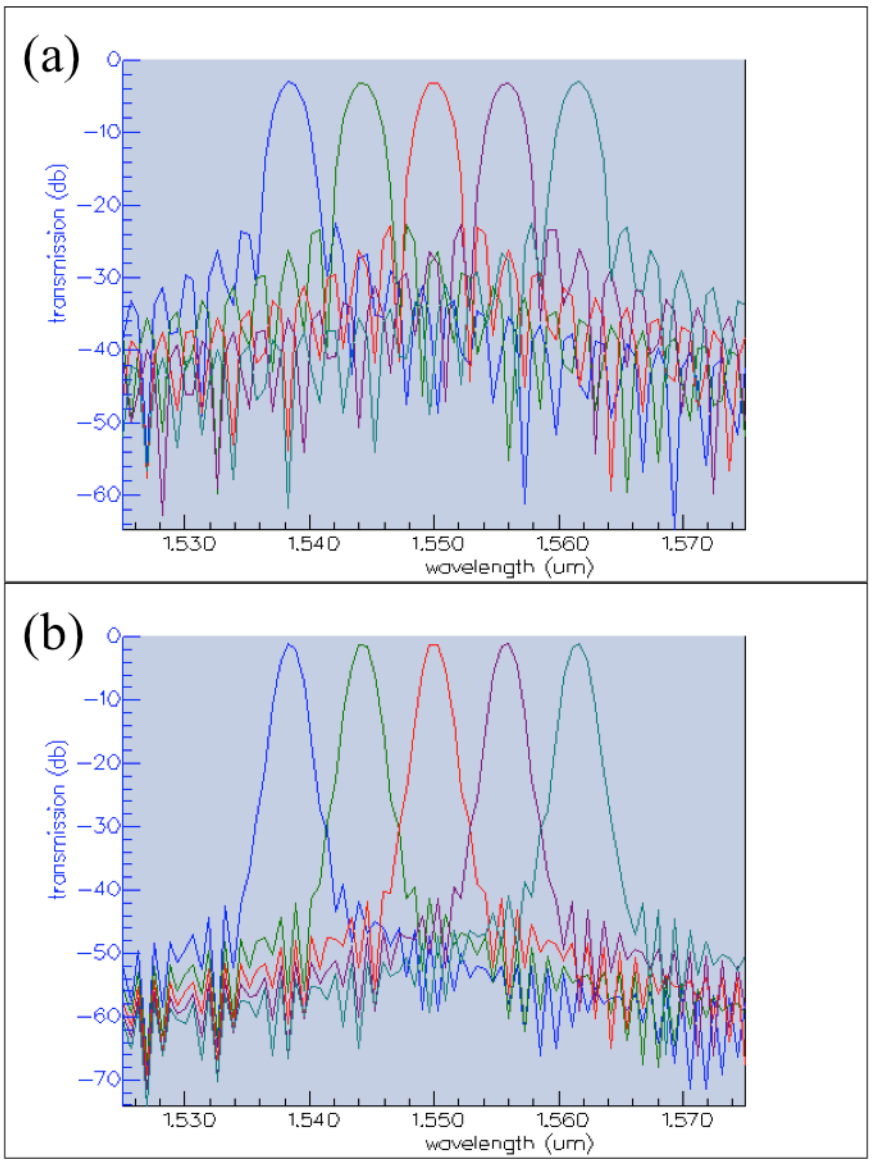

Figure 6-13: Output spectra of echelle gratings under different grating lengths, (a) has the grating length of 800 um, and (b) has grating length of 1600 um

Fig. 6-13 shows the output spectrum for two different echelle gratings. These two echelle gratings have the same grating period, blazed angle, incidence angle, designed order and the same radius of the "Rowland Circle" (R = 800um). The only difference is the total grating length is 800um for Fig. 6-13 (a) and 1600um for Fig. 6-13 (b). We have 5 output channels, and the distance between two nearby output waveguides is 5um. The

central wavelength is designed to be 1550nm. As we can see from Fig. 6-13, the wavelength spacing between nearby channels is the same for both designs and is around 6nm. However, the echelle grating with longer grating length has a much better cross talk than that of the shorter one, which means a long enough grating length is very important.

(II) The effect of the radius of the "Rowland Circle"

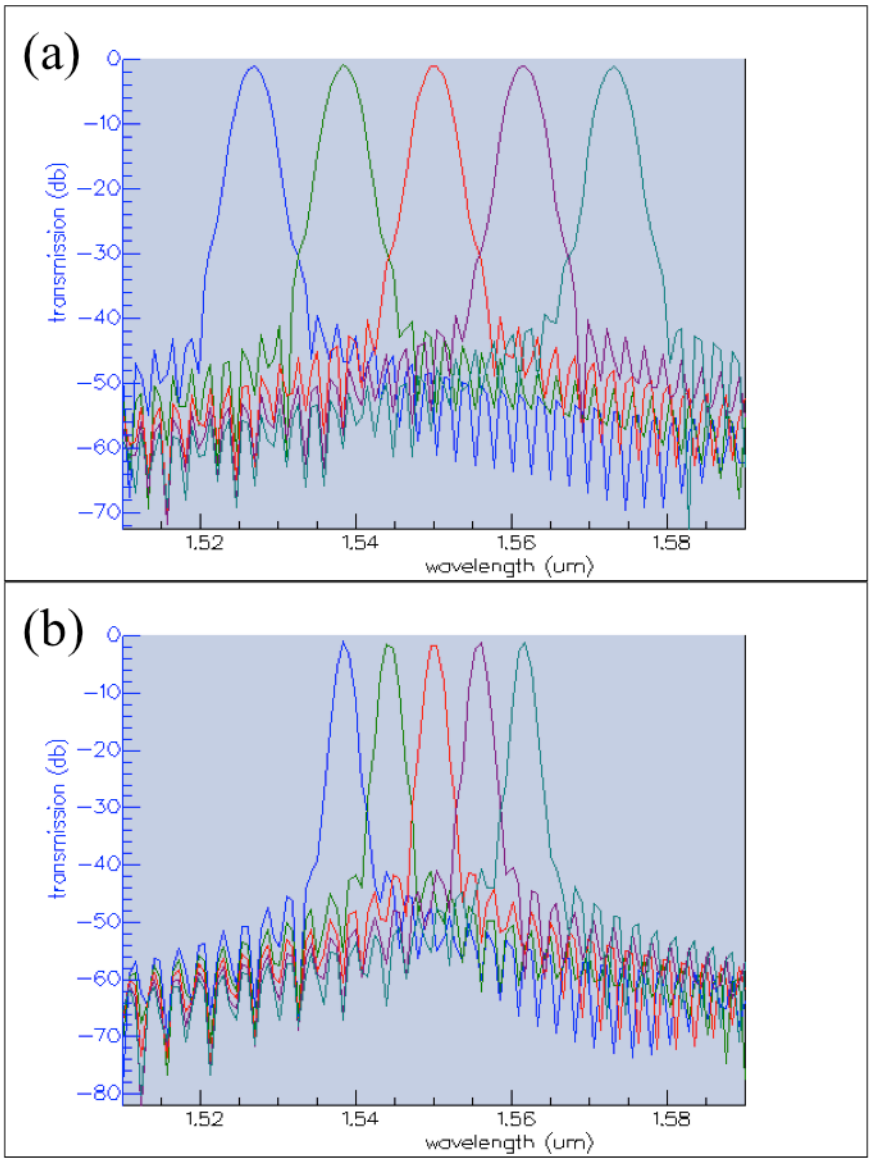

Figure 6-14: Output spectra of echelle gratings under different Rowland-Circle radiuses: (a) has a radius of 400 um, and (b) has a radius of 800 um

A bigger Rowland circle means a longer diffraction length, which will give better resolution of the spectrum. We designed two echelle gratings with different Rowland – Circle radius. Fig. 6-14 (a) shows the simulated output spectrum of an echelle grating with a radius of 400um, while Fig. 6-14 (b) shows the simulated output spectrum of an echelle grating with a radius of 800um. Both of the echelle gratings have a "long enough" grating length, which is 800um for (a) and 1600um for (b). We still have five output channels centered at 1550nm wavelength and the distance between two nearby waveguides is 5um. As we can see from the plots, the echelle grating with a bigger Rowland circle (Fig. 6-14 (b)) has a much higher resolution than the other one as expected.

(III) The Effect of the designed diffraction order

The echelle grating is basically a kind of blazed grating designed to use its high order diffraction. As shown in the grating angular dispersion equation, the larger order has a better angular dispersion. To prove this, we simulate two different echelle grating designed for different orders.

Fig. 6-15 shows the simulation result of the output spectra for these two echelle grating. The echelle grating in Fig. 6-15 (a) is designed for the 6^{th} diffraction order, while the echelle grating in Fig. 6-15 (b) is designed for the 13^{th} diffraction order. The different designed diffraction orders means different blazed angles. The other parameters for these two echelle gratings are the same. They have the same incident angle, same grating period of 8.25um, same Rowland – Circle radius of 800um and the same grating length of 1600um. We still have 5 output channels centered at 1550nm wavelength, and the distance between each waveguide is 5um. As we can see from the image, the higher order

diffraction shown in Fig. 6-15 (b) has a much better angular dispersion and higher resolution than the lower order diffraction shown in Fig. 6-15 (a) as expected.

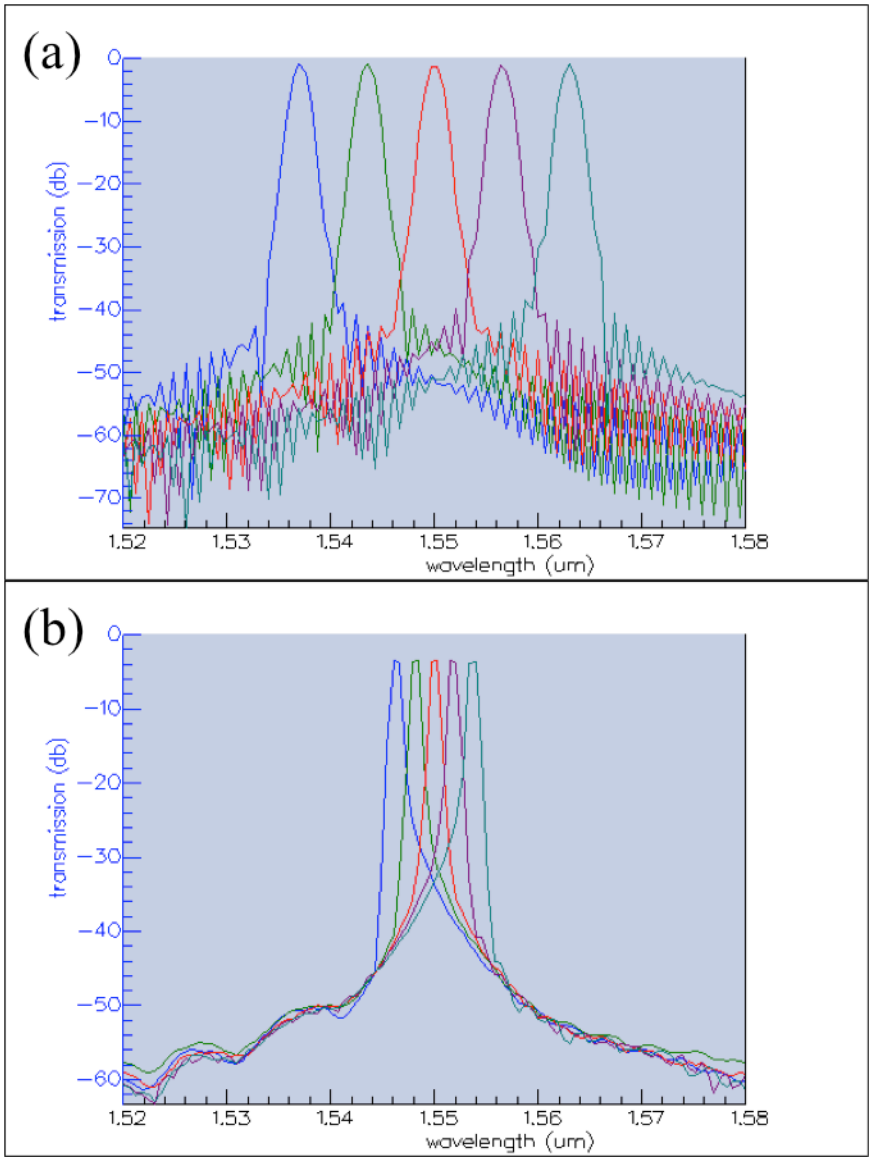

Figure 6-15: Output spectra of echelle gratings under different diffraction orders, (a) is designed for the 6th order, and (b) is designed for the 13th order

(IV) The effect of the grating period

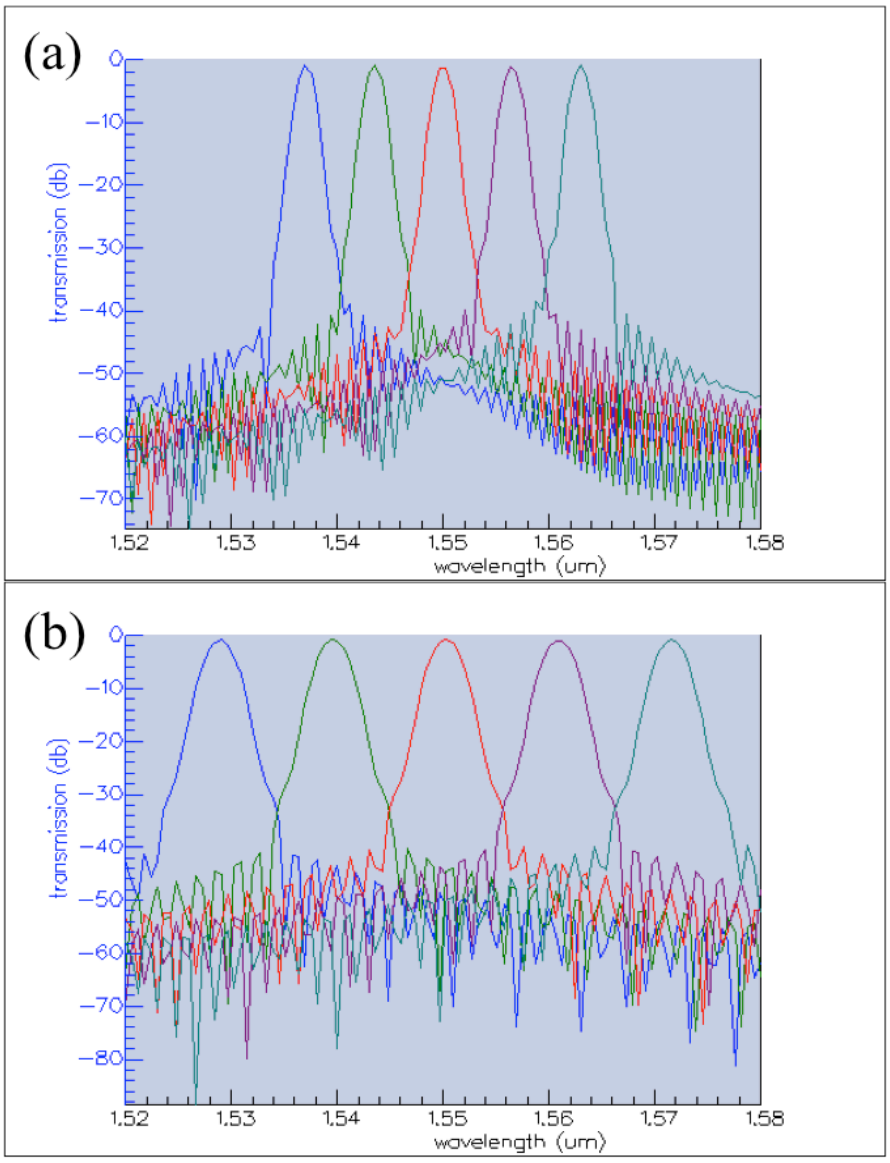

Figure 6-16: Output spectra of echelle gratings under different grating periods, (a) has a grating period of 8.25 um, and (b) has a grating period of 14um

As also can be seen from the angular dispersion equation, a larger grating period will lead to a lower angular dispersion. Fig. 6-16 shows the simulated output spectra for echelle gratings with different grating periods. The grating in Fig. 6-16 (a) has a grating period of 8.25um, while the grating in Fig. 6-16 (b) has a grating period of 14um. Both of

the gratings are designed for the 6th diffraction order and all the other parameters are the same. The 5 output channels have a center wavelength of 1550nm and the distance between two nearby waveguide is also 5um. As we can see from the image, the echelle grating with the longer grating period (b) has a much lower angular dispersion or resolution as expected.

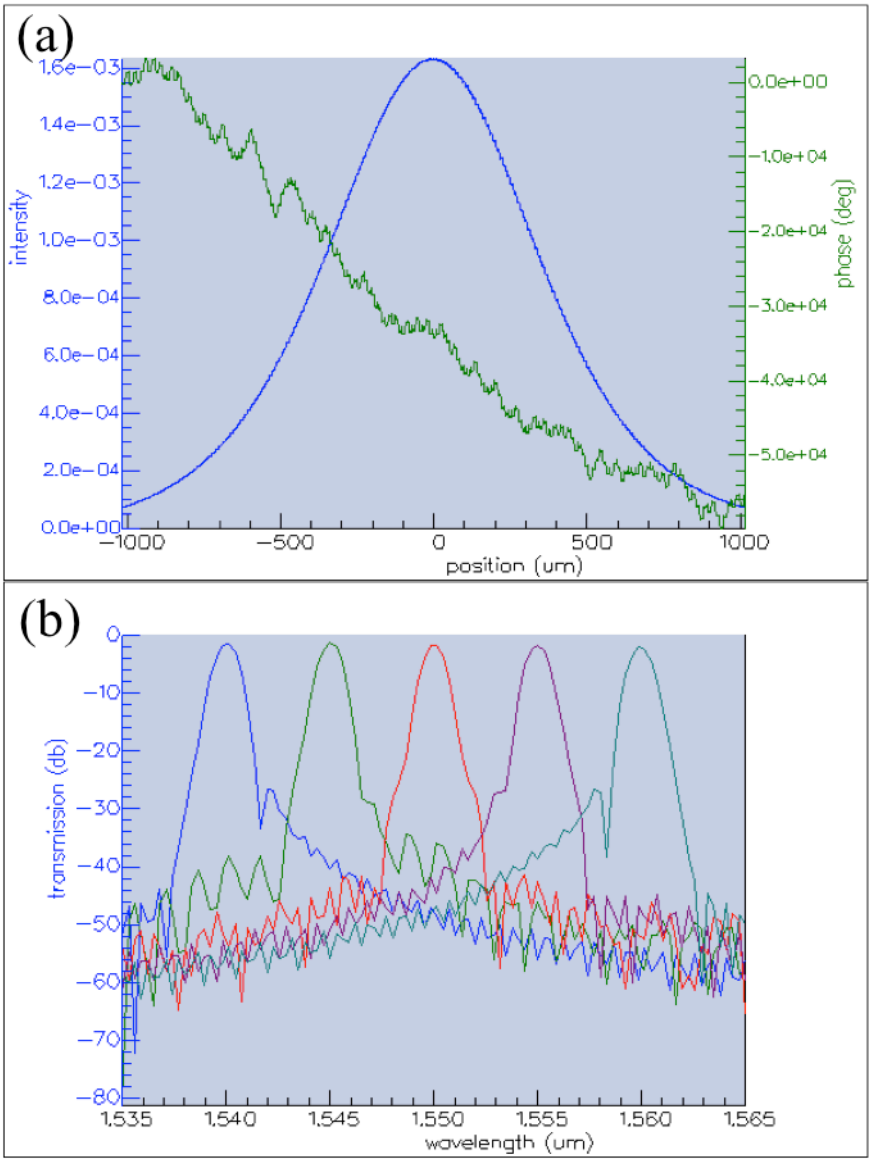

Figure 6-17: Our first design for an echelle grating spectrometer, (a) before-grating wavefront of this design, (b) output spectrum of this design

As a result, in order to have a better angular dispersion and resolution, we need to have long enough total grating length, larger radius of Rowland circle, smaller grating period, and a design that uses higher diffraction order. However, considering that we first need to find a successful fabrication process, we start with an echelle grating with 5 output channels centered at 1550nm. The spacing between each channel is 5nm in wavelength. The radius of the Rowland circle is 700um, and the total length of the gratings is 1400um which is long enough. The grating period is 8um and the echelle grating is designed for its 10^{th} diffraction order.

The Fig. 6-17 shows the simulation result of this first design. Fig. 6-17 (a) shows the before - grating wavefront of this design, which means that a total grating length of 1400um is long enough to diffract most of the incident light. Fig. 6-17 (b) shows the spectrum of the 5 output channels. The adjacent channel crosstalk is about -35dB to -40dB. This echelle grating is not very big which is comparatively easy to fabricate, and it also have a reasonably good performance that makes this design a good one to start with. This design is optimized for TE mode.

Chapter 7 : Experiments and Results

7.1 Fabrication

7.11 Fabrication Process Design

As discussed in the simulation section above, we use Epipprop to simulate the echelle grating based on the Rowland-Circle template. Instead of drawing the complicated lithography pattern by using other GDS-II editing softwares, the Epipprop software can generate the GDS-II file of the echelle grating structure that we designed with very high resolution, including the input and output waveguide. However, the automatically generated GDS-II file draws the cladding of the waveguide rather than the core. Considering the cladding size is much wider than the core size for a 900nm wide waveguide, it takes a much longer time to write the claddings if there are many output waveguides when using the E-beam lithography. Therefore, we reverse the pattern and let the E-beam lithography write the waveguide cores and extend the waveguides to the edge of the chip as we designed for chip cleaving and fiber coupling.

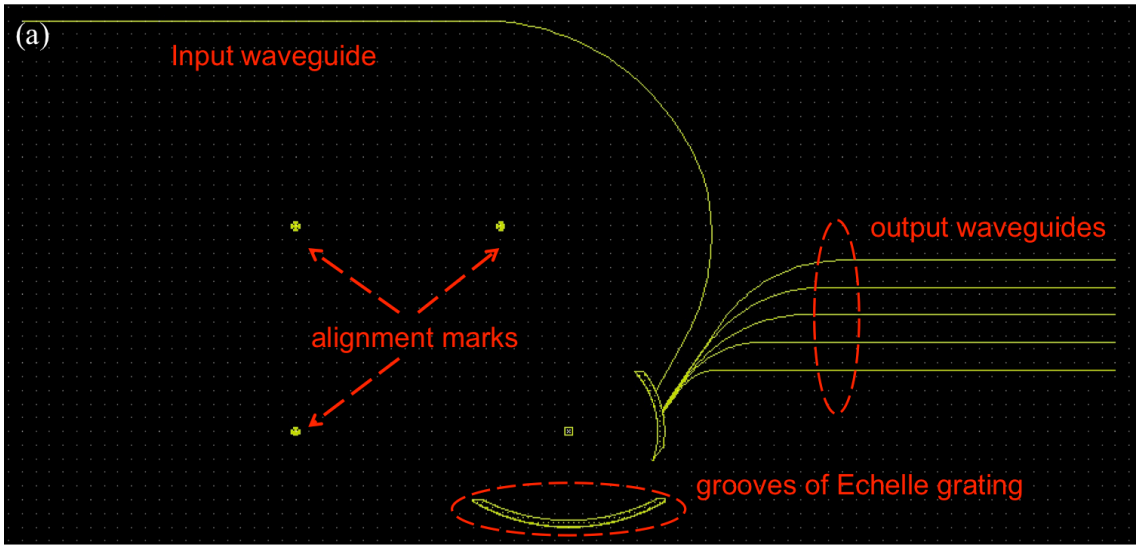

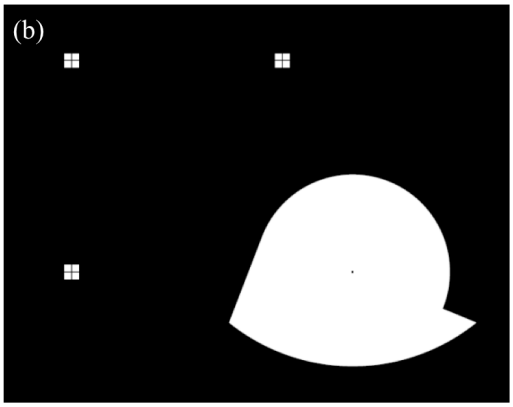

Figure 7-1: GDS-II pattern of echelle grating for E-beam lithography, shown as (a), and photolithography, shown as (b)

Fig. 7-1 (a) shows the GDS-II file of our designed echelle grating after reversing the pattern and extending the waveguides. As we can see from the image, there is an empty place between the waveguides and the grooves of echelle grating, which is the "free propagation" region for the input and diffracted light. If we write this area by E-beam lithography it will take a very long time. So we decided to use the photolithography to write the center "free propagation" region, which is shown in Fig. 7-1 (b). The three alignment marks shown in both Fig. 7-1 (a) and (b) are used to align this two lithography patterns together.

Fig. 7-2 shows the process flow we designed for fabricating the echelle grating. First we deposit 300nm LPCVD Si_3N_4 on 5um thermal oxide, and a 1.5um-thick SiO_2 layer is deposited on the top by PECVD (the mode diameter is 0.729um for TE mode and 1.066um for TM mode at 1550nm in the vertical direction, so 1.5um thick SiO_2 layer is thick enough to be the top cladding). Then we use E-beam lithography to write the pattern shown in Fig. 7-1 (a) and deposit 70nm Cr as the hard mask for ICP etching by E-beam deposition. Afterwards, we use photolithography to write the pattern shown in Fig. 7-1 (b) and deposit another 70nm Cr as the hard mask for ICP etching. With the Cr hard

mask we use ICP fluorine etcher to etch 1.5um PECVD SiO_2, 300nm LPCVD Si_3N_4, and another 1.5um thermal oxide. After this, we use Cr etchant to remove the remaining Cr hard mask and deposit 100nm silver (Ag) on the sidewall of the echelle grating's grooves as the reflecting mirrors for the incident light. At last, we deposit another layer of 4um PECVD SiO_2 on the top.

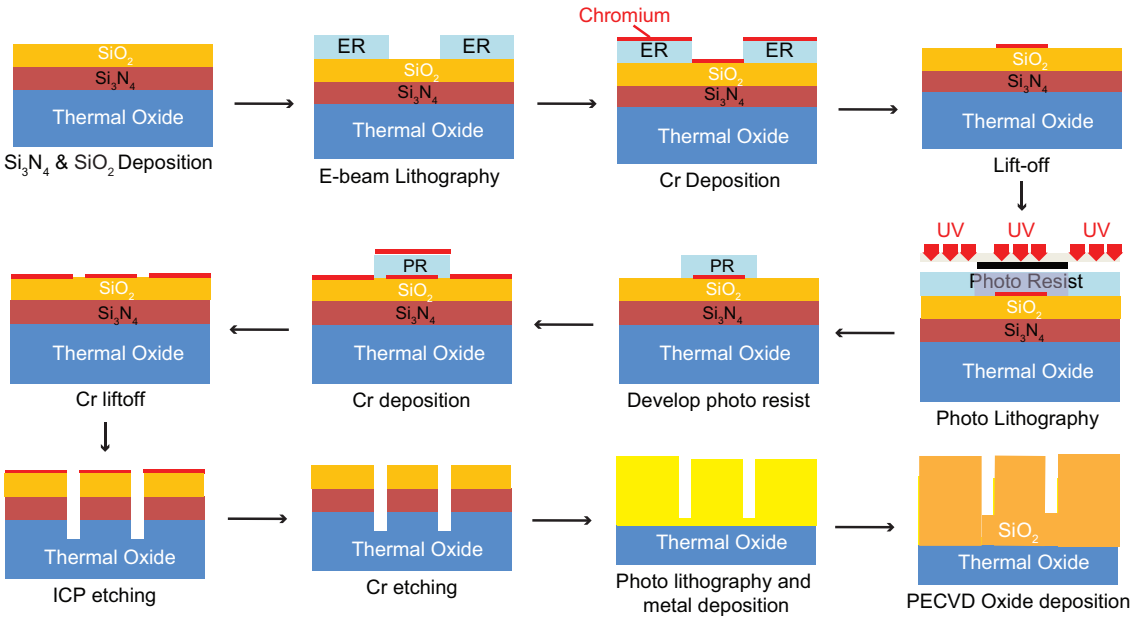

Figure 7-2: Schematic of fabrication process flow

7.12 Waveguide, Inversed Taper and Grating Fabrication

Fig. 7-3 (a) and (b) show the optical microscopic images of the patterns after the E-beam lithography, the first Cr deposition and the first Cr liftoff. This pattern is mainly generated from the simulation software (Epipprop) as shown in Fig. 7-1 (a), which requires high writing resolution such as the grooves of echelle Grating, 325nm wide taper structure and 900nm wide waveguides. So we write this pattern by E-beam lithography. Fig. 7-3 (a) shows the input and output waveguides part and Fig. 7-3 (b) shows the

grooves part. The wide white arcs shown in both these two images are the overlapping regions for the second photolithography.

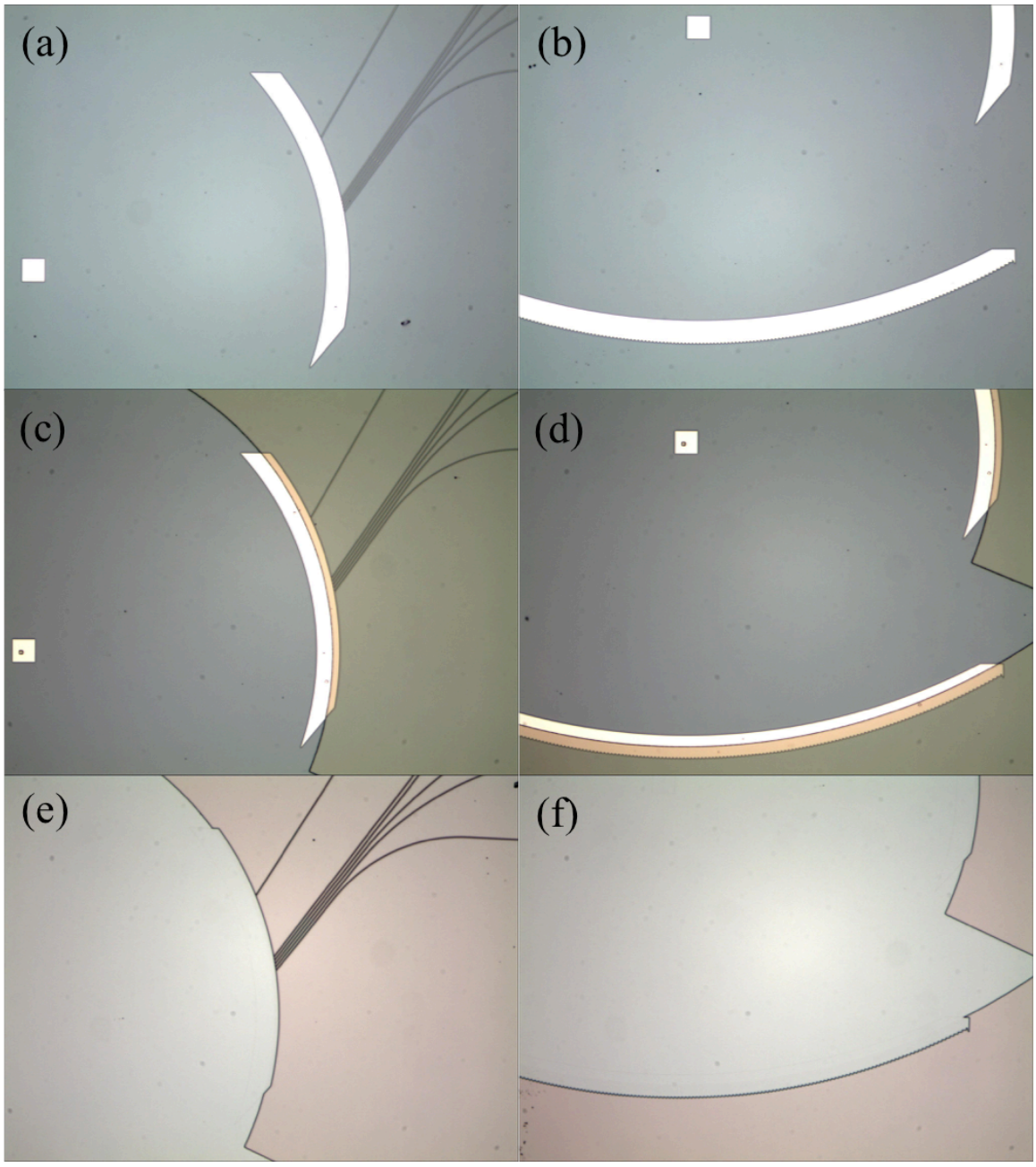

Figure 7-3: Optical microscopic images of echelle gratings: waveguide part (a) and grating part (b) after E-beam lithography and the 1st Cr liftoff, waveguide part (c) and grating part (d) after photolithography for the center free-propagation region, waveguide part (e) and grating part (f) after 3.3 um deep ICP etching and Cr removal

Fig. 7-3 (c) and (d) shows the optical microscopic images of the patterns after the photolithography. The light brown transparent regions in these two figures are the remaining photo resist after developing. This photo resist is overlapping with the patterns shown in Fig. 7-3 (a) and (b) and leave the central part open for the second Cr deposition and liftoff. This photolithography pattern is designed for the large "free propagation" region of the echelle grating shown in Fig. 7-1 (b). This pattern does not need high resolution and would take a very long time to write if we here to use E-beam lithography. Fig. 7-3 (e) and (f) shows the optical microscopic images of the patterns after the second Cr deposition and the 3.3um deep ICP etching for SiO_2 and Si_3N_4. After combining the E-beam lithography and the photolithography, we can see the whole pattern of the echelle grating from these two figures.

Fig. 7-4 (a) shows the SEM image of the whole pattern of the echelle grating, we can also see the similar patterns that are part of the echelle grating in Fig. 7-3 (e) & (f). As we can see from the Fig. 7-4 (a), there is one input waveguide, 5 output waveguides, the grooves of the echelle grating are at the bottom and the three alignment marks are at the upper left part of the image. Fig. 7-4 (b) shows the output waveguide part and Fig. 7-4 (c) shows the grooves part of the echelle grating. Fig. 7-4 (d) shows the taper end after 3.3um deep ICP etching. As we can see from the image, the taper end is still 308nm wide (325nm as designed) after such a deep etching, and the aspect ratio is as high as 10.

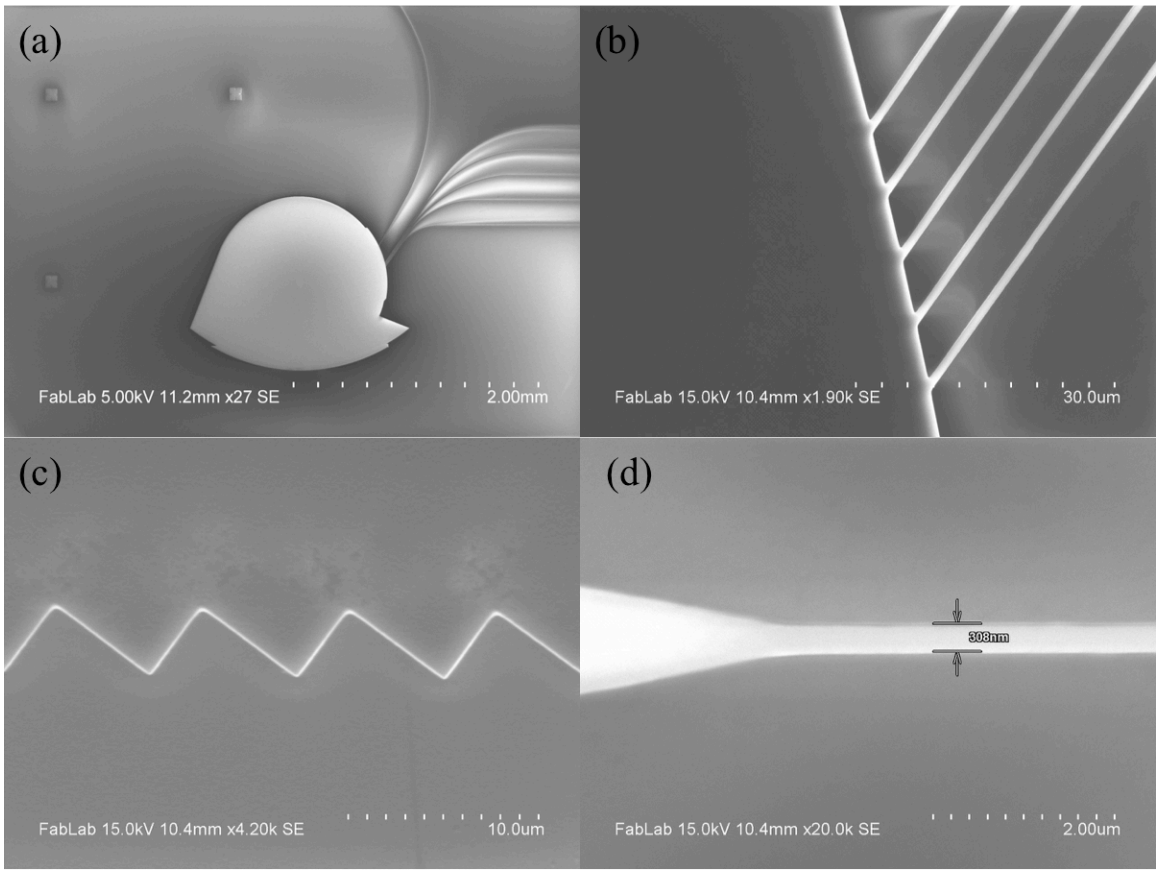

Figure 7-4: SEM images of the echelle Grating we fabricated: (a) whole pattern of the echelle grating, (b) 5 output waveguides after deep ICP etching, (c) grooves of the echelle grating after deep ICP etching, (d) end of inversed taper after deep ICP etching

7.13 Deep and Vertical SiO_2, Si_3N_4 Etching

The grooves of the echelle grating shown in Fig. 7-4 (c) is used as a reflector for the incident light and let it diffract into different order directions. To make it as a good reflector, we deposit Ag on the facet of these grooves. One important thing to achieve this is to make sure the facet is vertical enough. If the groove facet is tilted at a large angle, the incident light will not be reflected horizontally back and we will lose part of the light power. In addition, since the Si_3N_4 waveguide core is buried under the 1.5um thick SiO_2 top cladding and the total etch depth is 3.3um, the aspect ratio of this ridge is

very high. If the etching sidewall is not vertical enough, the real width of the waveguide core especially at the inversed taper part will be largely different than the design, and then affect the waveguide mode and the coupling efficiency. Therefore, a deep and vertical ICP etching for Si_3N_4 and SiO_2 should be achieved.

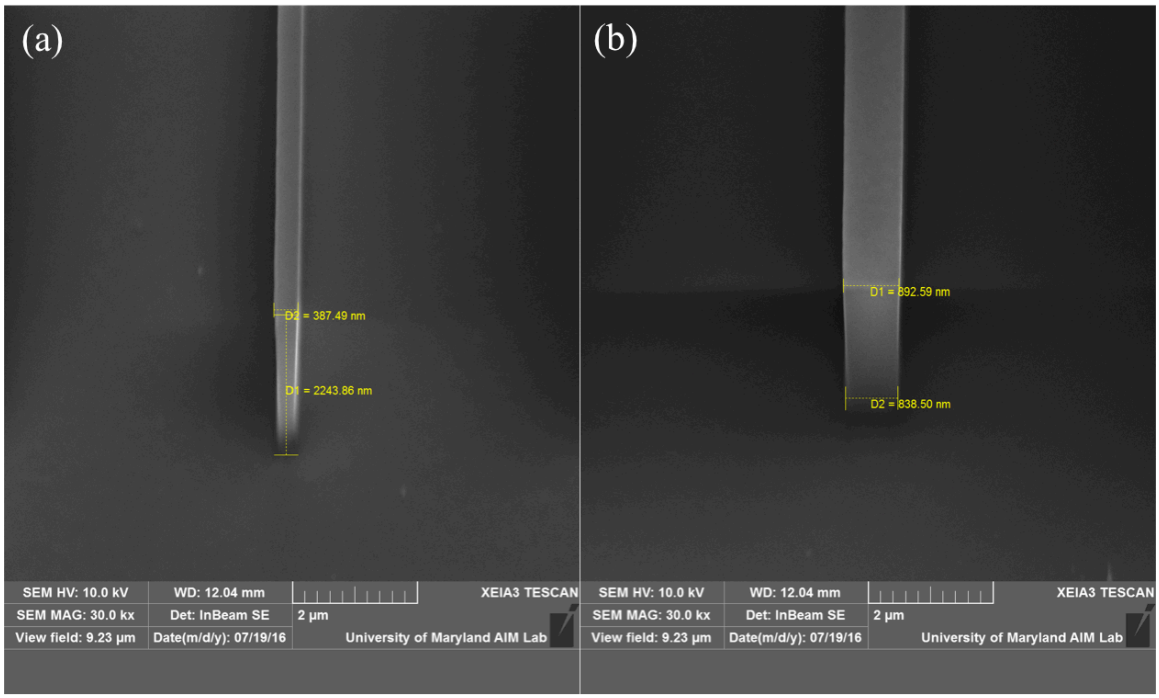

Figure 7-5: SEM images of the deep ICP etching profile: (a) a 387nm wide and 2243.9nm deep etched SiO_2 ridge, (b) a 892nm wide and 2243.9nm deep etched SiO_2 ridge

Fig. 7-5 (a) shows a 387.5nm wide and 2243.9nm deep SiO_2 ridge. Fig. 7-5 (b) shows a wider SiO_2 ridge but with the same depth. As we measured under the SEM, the upper width of the ridge in Fig. 7-5 (b) is 892.6nm and the lower width is 838.5nm. As a result, the angle of the sidewall is 89.31°, which is vertical enough for deep etching and making the grooves to be good reflectors. We fabricated many waveguides and repeated this measurement multiple times, and we can achieve a sidewall angle of around 89° for them.

7.14 Grating's Reflection Mirror Fabrication

As almost the final step in our fabrication process, we need to deposit 100nm Ag on the sidewalls of the grating grooves. We first do a photolithography to cover the waveguides area with photo resist preventing them from being deposited by Ag. Since the waveguide is etched down very deep and its aspect ratio is very high especially at the inversed taper part (0.325um wide and 3.3um deep), the spinning of photo resist should be comparatively slow to prevent the waveguide from being broken. Then we deposit Ag on the sample with a close-to-90° tilted angle by E-beam deposition. Then, we put the sample in the "Remover PG" to remove all the photo resist and the unwanted Ag, and deposit another layer of 4um PECVD SiO_2 to protect everything.

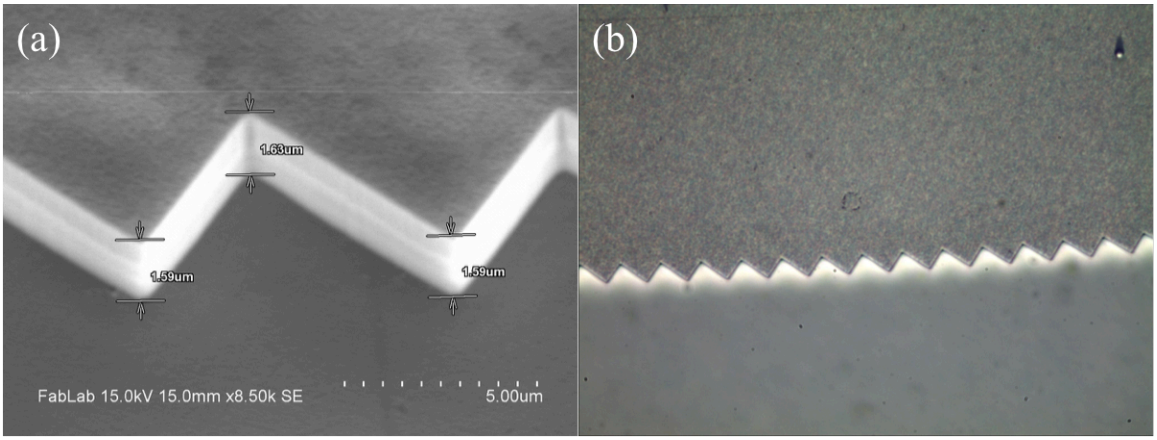

Figure 7-6: (a) SEM image of the deep etched grating grooves; (b) optical microscopic image of grating grooves after 100nm Ag deposition on the sidewalls

Fig. 7-6 (a) shows the SEM image of the deep etched grating grooves (before Ag deposition). This image is taken when the sample is tilted by 30° to see the groove facet. As we can see from the image, the etching depth of the groove is about 3.2um (direct measure shows 1.6um in the image, considering the 30° tilted degree, the real depth is 1.6 * 2 = 3.2um). Fig. 7-6 (b) shows the optical microscopic image of the grooves after

100nm Ag deposition on the sidewall. Since the etching depth is as deep as 3.2um, as we can see from the image the focus is on the top surface of the grooves and the bottom looks blurry. The white shining part at the edge of these grooves is the deposited Ag although they also look blurry.

7.2 Coupling Efficiency and Propagation Loss Measurement

Fig. 7-7 shows the experimental result for the propagation loss and fiber-waveguide coupling efficiency measurement for 1550nm wavelength. The waveguide is 900nm wide and 300nm thick as we designed, and we add a 500um long inversed taper at each end of the waveguide with a taper end width of 325nm as designed. The fiber we are using for this measurement is UHNA3 single mode fiber from Thorlabs. According to the simulation, the fiber-waveguide coupling efficiency should be around 96% to 98%.

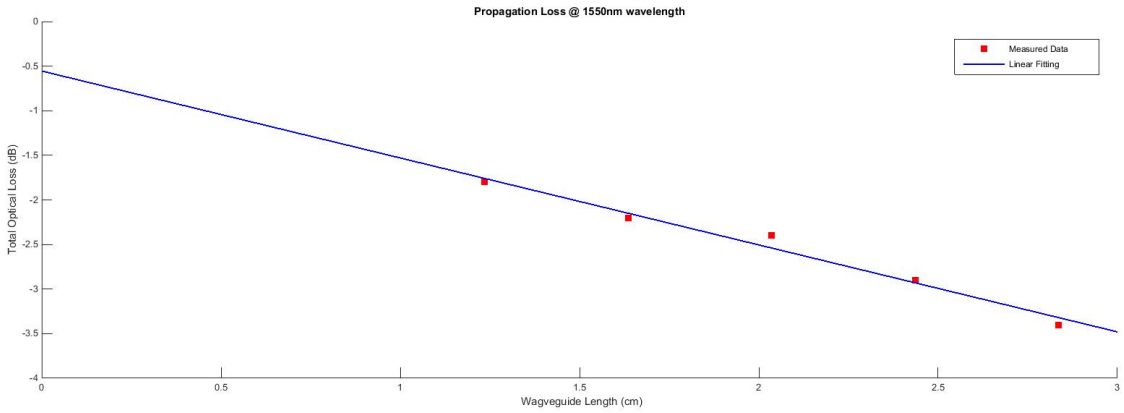

Figure 7-7: Experimental result for propagation loss and coupling loss measurement

In this measurement, we write five waveguides with different waveguide lengths in the same sample (similar pattern is shown in Fig. 3-8 (a)). This method is much more precise than the traditional cut-back technique when measuring the propagation loss of short and low-loss waveguide. By measuring the total insertion loss of these five

waveguides (shown as the red squares shown in Fig. 7-7), we can make a linear fit to these data (shown as the blue line in Fig. 7-7). The lengths of these five waveguides are 1.2457, 1.6457, 2.0457, 2.4457 and 2.8457 in cm. The total insertion loss consists of the propagation loss and the coupling loss for both coupling facets. Considering we have the same inversed taper structure on both ends of the waveguides, the coupling loss should also be the same for both facets. Therefore, the slope of the blue line is the propagation loss of the waveguides, and the crossing point of the blue line at the y-axis is the total coupling loss for the two facets. As a result, the measured propagation loss is -0.975dB/cm and the fiber-waveguide coupling efficiency is about 94% per facet (total coupling loss for two facets is -0.54dB) as shown in Fig. 7-7. The coupling efficiency is very close to our simulation result and the propagation loss is also relatively low.

7.3 Bending Loss Measurement

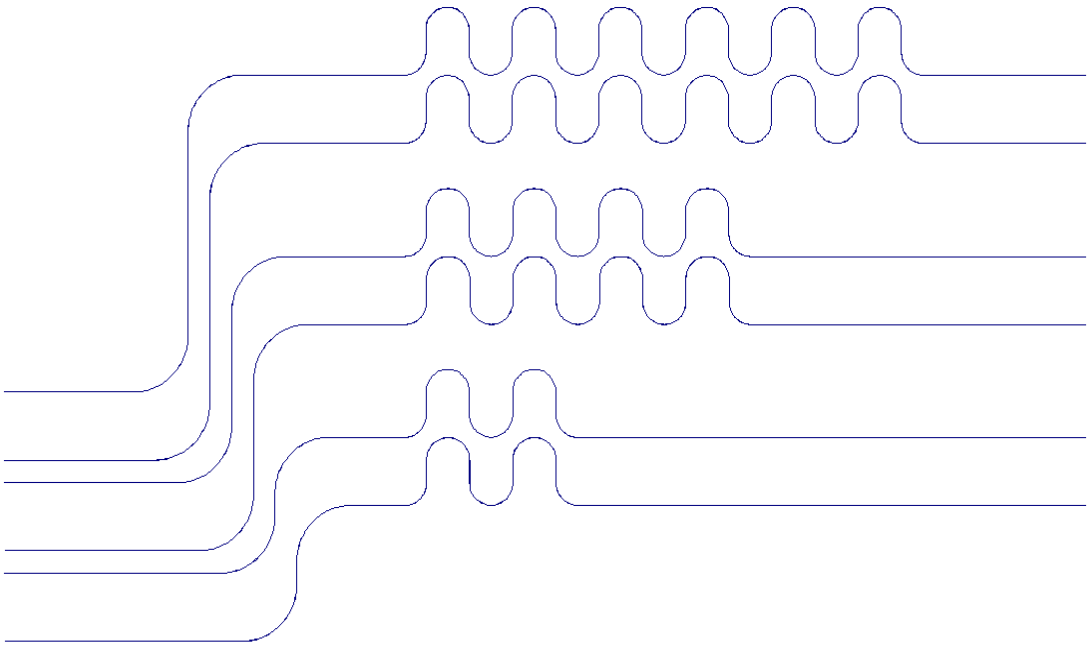

Figure 7-8: E-beam lithography pattern for bending loss measurement

In this on-chip photonic circuit we have many bending parts in the input and output waveguides, and we may have more bending areas later when integrated with other on-chip optic devices such as Bragg-grating filters. Therefore, it is important to measure the bending loss of the waveguide we design. We first measure the bending loss of a 900nm wide and 300nm thick Si_3N_4 waveguide with a 200um bending radius.

Fig. 7-8 shows the E-beam lithography pattern for the bending loss measurement. As we can see from the image, we have 6 waveguides with different bending lengths. Among the 6 waveguides, two of them have 4 half circles (total bending length is 0.251cm), another two have 8 half circles (total bending length is 0.503cm), and the last two waveguides have 12 half circles (total bending length 0.754cm). Except for the different bending lengths, the six waveguides have the same length of straight waveguide parts, and all the half circles have the same radius of 200um. There is another 200um long straight line connecting the nearby half circles, making the bending mode transfer adiabatically from the left bend to the right bend.

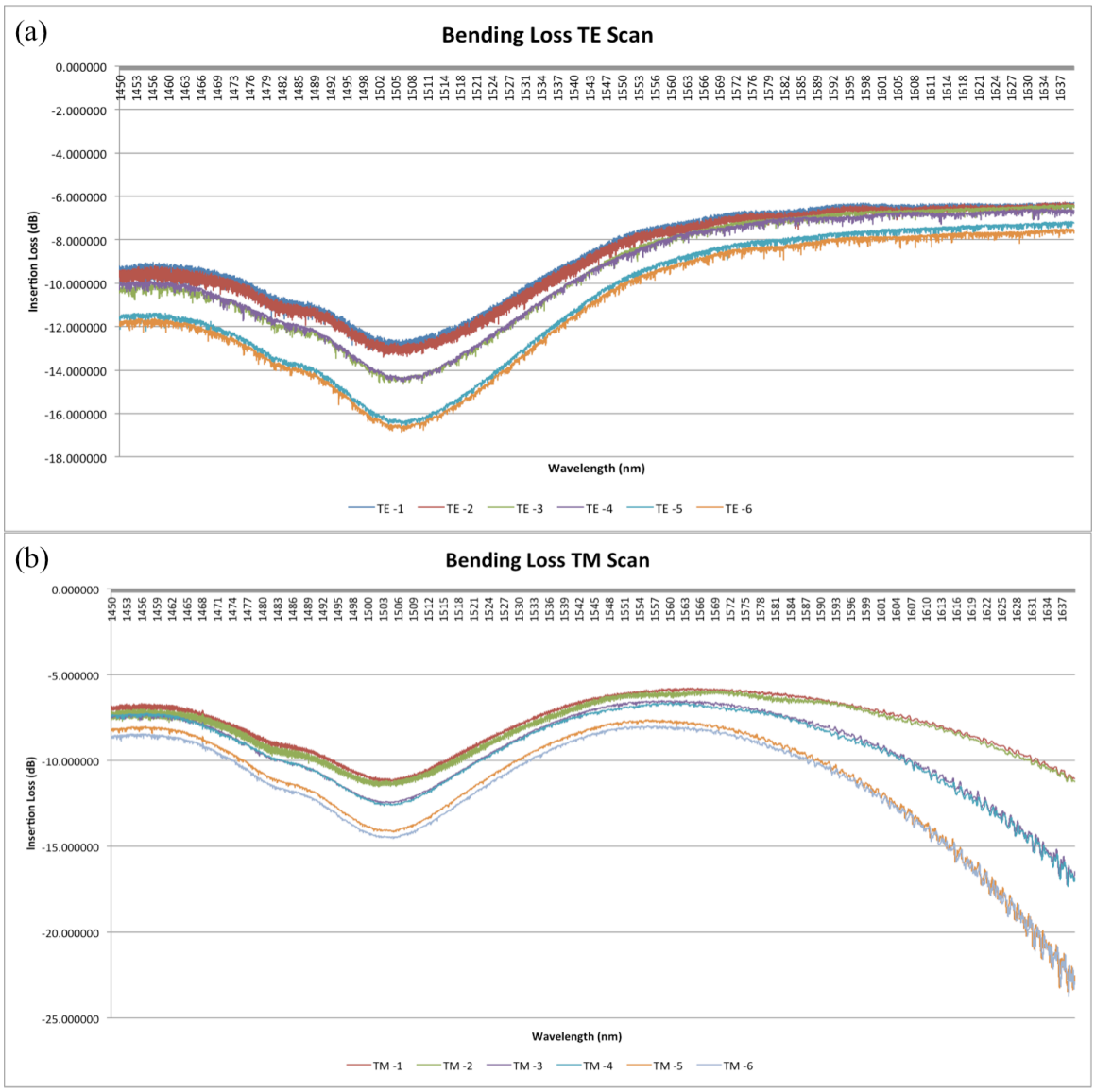

Figure 7-9: Bending loss measurement for waveguide with 200um bending radius, wavelength scanned from 1450nm to 1640nm for TE mode (a) and TM mode (b)

Fig. 7-9 shows the insertion loss for these 6 bending waveguides for its TE (Fig. 7-9 (a)) and TM (Fig. 7-9 (b)) mode for a wide wavelength range from 1450nm to 1640nm. We can see there is a dip around 1505nm wavelength for both TE and TM modes, which is because the Si_3N_4 deposition will have some residual N-H and Si-H bonds in the Si_3N_4 film. The N-H bond has the peak absorption at around 3350cm^{-1} (2985.1nm) and the Si-H

bond has the peak absorption at around 2200cm^{-1} (4545.5nm), which means the first overtone of N-H bond's absorption peak is 1492.6nm and the second overtone of Si-H bond's absorption peak is 1515.2nm. These absorptions around 1505nm contribute to the dip as shown in the images. Besides, as we can see from Fig. 7-9 (b), there is an increase of the insertion loss and bending loss when the wavelength is larger than 1580nm only for the TM mode. This is because when the wavelength becomes larger the TM mode becomes much larger and more weakly guided than the TE mode, which result in a much larger bending loss.

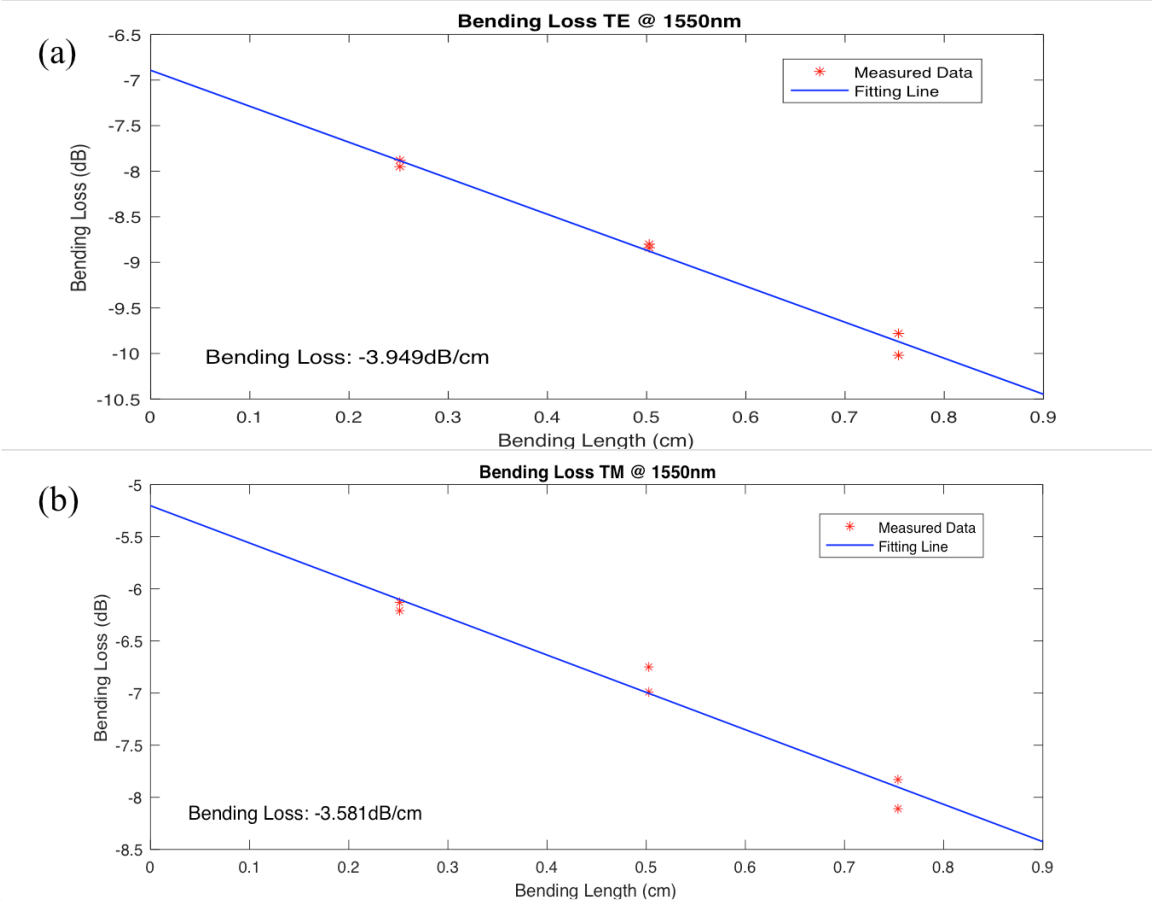

Figure 7-10: Bending loss results for TE (a) and TM (b) modes at 1550nm wavelength for a bending radius of 200 um

Fig. 7-10 shows the experimental bending loss results ((a) for TE mode and (b) for TM mode) for the waveguide we designed with a bending radius of 200um at 1550nm wavelength. The red points shows the experimentally measured data for each waveguide and the blue line shows the linear fitting of these red points. The slope of this blue line shows the bending loss. As a result, the bending loss of the waveguide with a bending radius of 200um is -3.949dB/cm for its TE mode and -3.581dB/cm for its TM mode, which is relatively low and similar because both of these modes are strongly guided and of similar mode sizes.

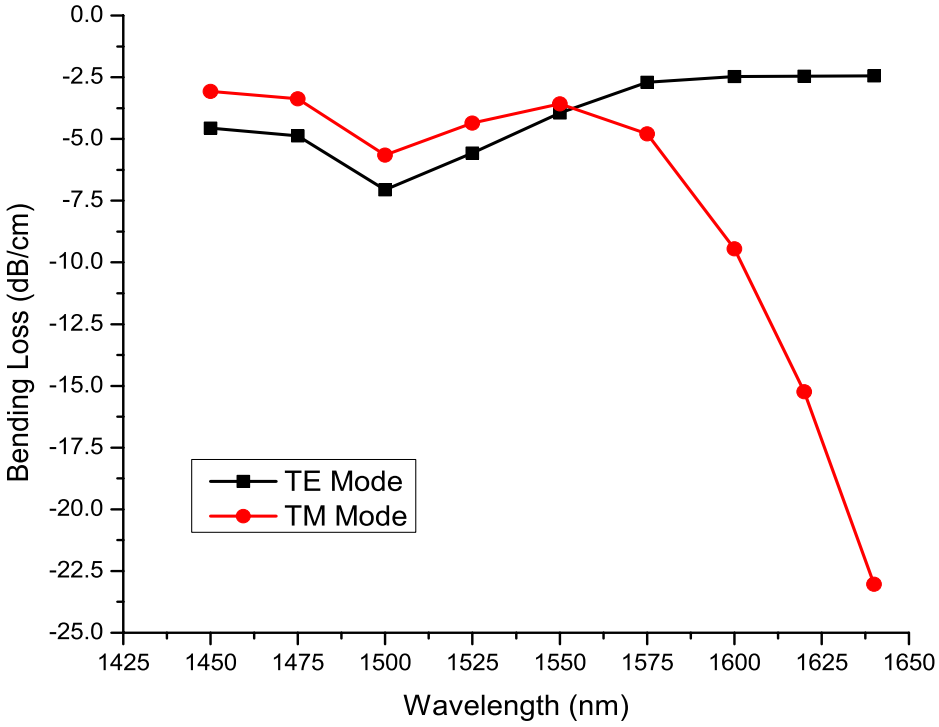

Wavelength (nm)	1450	1475	1500	1525	1550	1575	1600	1620	1640
Bending Loss, TE (dB/cm)	-4.56	-4.88	-7.06	-5.58	-3.95	-2.70	-2.47	-2.54	-2.44
Bending Loss, TM (dB/cm)	-3.07	-3.38	-5.65	-4.36	-3.58	-4.79	-9.45	-15.24	-23.03

Figure 7-11: Waveguide bending losses at different wavelengths

Fig. 7-11 shows the experimentally measured bending loss of the waveguide we designed with a bending radius of 200um under different wavelengths for both TE and TM modes. As we can see from the plots, when the wavelength is smaller than 1500nm, the bending loss increases as the wavelength goes larger for both TE and TM modes. It is because a larger wavelength has a larger mode size and lower mode confinement factor (shown in Fig. 6-5), which contributes to the larger bending loss. Besides, the big dip around 1500nm also results from the absorption from Si-H and N-H bonds remained in the Si_3N_4 film.

From the plots we can also see that the bending loss decreases as the wavelength increases when the wavelength is larger than 1500nm for the TE mode. This is because the majority of the bending loss comes from the scattering loss when the light propagates through the imperfectly smooth sidewall, and this scattering loss is inversely proportional to the wavelength. Although a larger wavelength has a larger mode size and a smaller confinement factor which usually contribute larger bending loss, the bending-loss contribution from the wavelength dependent scattering loss may play an more important role at this wavelength range than that from the confinement factor. However, the TM shows the opposite trend when the wavelength is larger than 1550nm. This is because the TM mode is much larger than its corresponding TE mode. When the wavelength is larger than 1550nm the TM mode size becomes too big and the mode confinement factor becomes more important than the wavelength dependent scattering loss again.

7.4 Echelle Grating Spectrometer Measurement

We have already achieved high fiber-waveguide coupling efficiency, low propagation loss and a reasonably low bending loss for the input and output waveguides

of the echelle-grating spectrometer. Here, we present the output spectrum of the echelle grating we designed and fabricated. The input and output waveguides are coupled with the PM fibers.

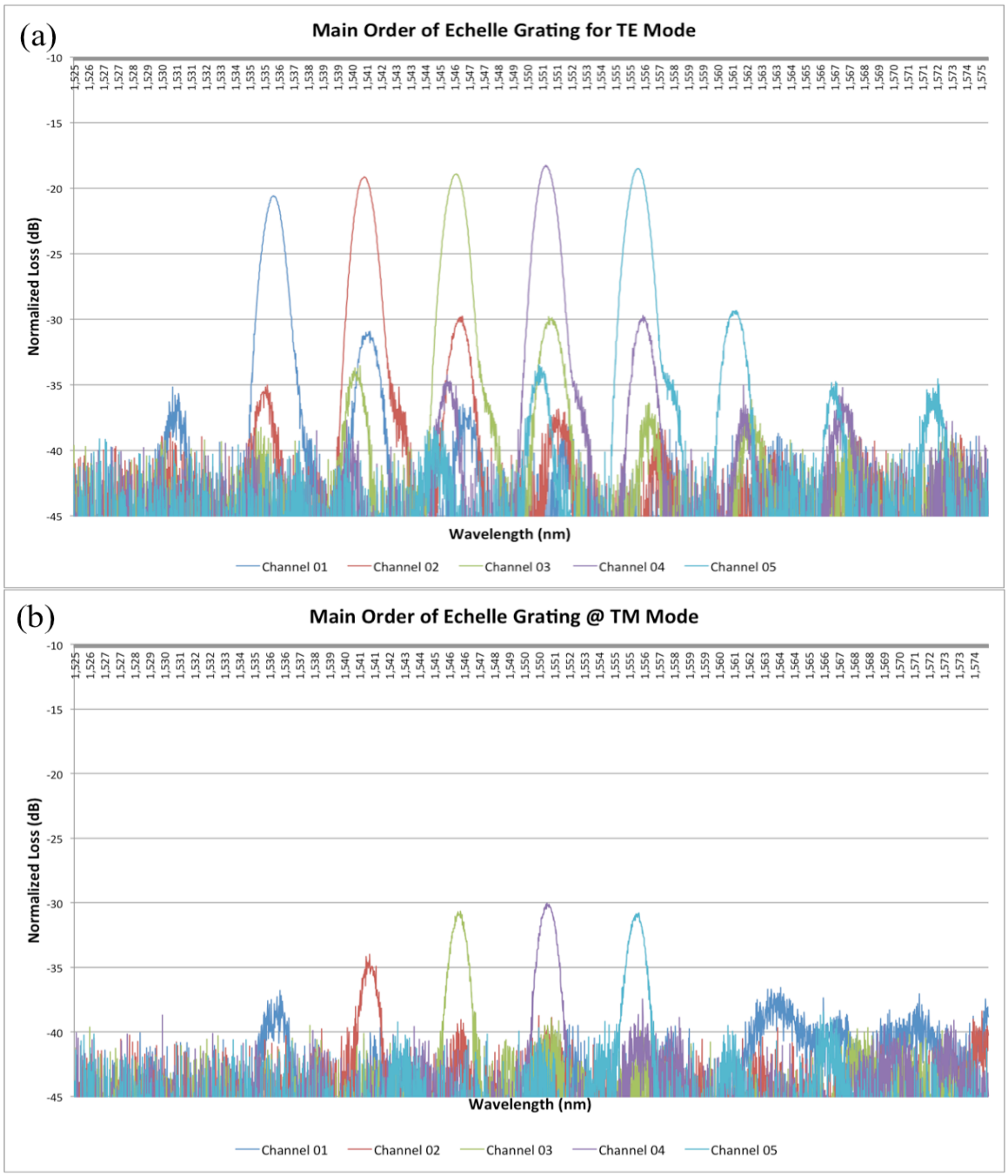

Figure 7-12: Experimentally measured output spectrum for the TE (a) and TM (b) modes of the echelle grating we designed and fabricated

As discussed in the simulation section, this echelle grating is designed to use the 10^{th} order and optimized for its TE mode. The simulated centered wavelength is at 1550nm and the channel spacing is 5nm in wavelength. Fig. 7-12 shows the experimentally measured output spectrum of this echelle grating. Fig. 7-12 (a) shows the output spectrum of its TE mode. The experimentally measured centered wavelength is 1545.8nm that is 4.2nm shifted to the left compared to the simulation. We think this shift in central wavelength may come from the imperfect fabrication such as the small shift of pattern position or tiny change of the pattern size and so on, which can be solved with more accurate fabrication. Since the 4^{th} channel has peak wavelength at 1550.8nm and the 3^{rd} channel has its peak wavelength at 1545.8nm, the channel spacing is exactly 5nm which is in agreement with our simulation.

Taking the 4^{th} channel as an example (channel closest to 1550nm), the full width half maximum (FWHM) of this channel is 0.74nm as measured. According to the resolution equation, $R = \frac{\lambda}{\Delta\lambda}$, where R is the spectral resolution (also called resolving power), λ is the wavelength of interest, and $\Delta\lambda$ is the smallest wavelength interval that can be resolved (here we can treat it as the FWHM of the channel), the spectral resolution of the echelle grating we fabricated is 2096. According to the simulation result, the spectral resolution is around 1200, and we believe this difference may be due to the imperfect fabrication or the simulation error. There are many ways to increase the spectral resolution as we discussed in the simulation section such as making the Rowland-circle radius larger, using a higher grating order, using smaller grating period and so on, which we will apply in our later design and fabrication to optimize our echelle grating.

As can been seen from Fig. 7-12 (a), the total insertion loss for this echelle grating is about -18dB, which is much higher than the result of our previous coupling loss and propagation loss measurement. This is because that we are using PM fiber here rather than UHNA3 fiber, and the taper size is not optimized for PM fiber for this sample. If we reduce the taper end width from current 325nm to 200nm as our simulation predicts, we may get smaller insertion loss. Also, when we characterized the coupling loss and the propagation loss, we did not need to etch very deeply to make the reflecting grooves while we only etched 300nm Si_3N_4 with a very slow and mild etching recipe. But for this echelle grating sample, we etched 3.3um deep (1.5um upper PECVD SiO_2 + 300nm LPCVD Si_3N_4 waveguide core + 1.5um thermal oxide underneath) that is much deeper than the previous etching. In this way, the etching recipe we used here is optimized for SiO_2 etching and is much more aggressive with a much higher etching rate (more than two times higher than the previous one). Therefore, we believe this strong etch might be too fast and make the etching sidewall not as smooth as before, which leads to a higher insertion loss. To solve this problem, we will divide the deep etching process into three parts: using the deep SiO_2 etching recipe for the upper 1.5um PECVD SiO_2 and the 1.5um thermal oxide underneath, and using the mild Si_3N_4 etching recipe for the middle 300nm LPCVD Si3N4 layer. We believe this will also reduce the insertion loss a lot.

Also, the experimental measured adjacent-channel cross talk of the echelle Grating we fabricated at its TE mode is about -12dB (because of the secondary peaks), which is also not as good as the simulation result. Actually, the GDS-II file generated by the simulation software has a slightly curved pattern for the grooves of the echelle grating.

However, after we reversed the pattern from a waveguide-cladding pattern to a waveguide-core pattern, the resolution of the curved grooves decreased. Therefore, the optimized structure calculated by the software could not be achieved by the real fabrication this time, which will also explain why there is not perfect match between the simulation and experimental results.

Fig. 7-12 (b) shows the experimentally measured output spectrum of the echelle grating for its TM mode. Since this echelle grating is designed and optimized for its TE mode, as we can see from the plot, the peak is much smaller and the insertion loss is much larger for the TM mode. However, the channel spacing is also 5nm and the spectral resolution is 2154 which is also very similar to the TE mode. The 4th channel has the peak wavelength at 1550.86nm, which is almost the same as the TE mode. This is because the mode is strongly guided at this wavelength and the mode sizes for TE and TM modes are very similar.

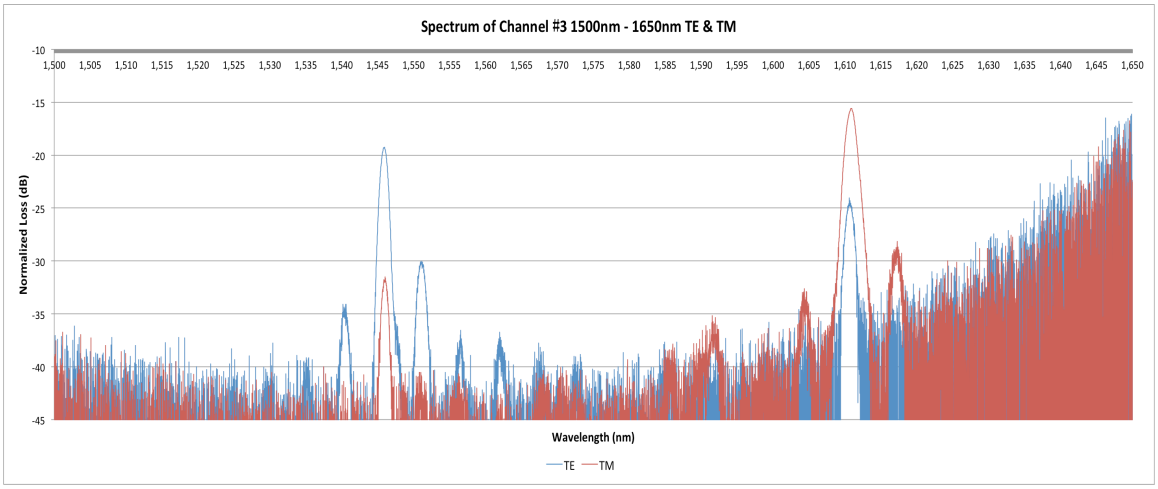

Figure 7-13: Experimentally measured free spectrum range for the TE & TM modes of the echelle grating we designed and fabricated

Fig. 7-13 shows the output spectrum of the 3rd channel for a wide wavelength range from 1500nm to 1650nm. The blue line represents the TE mode and the red line represents the TM mode. As we can see from the plots, the peaks of TE and TM modes are almost at the same position, and the free spectrum range is about 65nm for both TE and TM modes.

Chapter 8 : Conclusions

In this work, we have designed, fabricated and demonstrated an on-chip spectrometer based on an echelle grating for applications in astrophotonics. This spectrometer is designed for the near-infrared wavelength range from 1um to 1.7um.

Since most astronomical observation is light starving, it is very important to make the spectrometer with very low optical loss. We have successfully achieved a very high fiber-waveguide coupling efficiency that is more around 94% per facet at 1550nm wavelength experimentally by adding inversed tapers at both ends of the waveguides. These inversed tapers adiabatically transfer the large fiber mode into the much smaller waveguide mode to achieve a much better coupling efficiency. We also have achieved a very low propagation that is around 0.975dB/cm at 1550nm wavelength. In addition, since the on-chip spectrometer has many bending waveguide areas especially when integrated with other on-chip photonic devices such the Bragg-grating filter in the future, we have also characterized the bending loss of the waveguide. The bending loss of this waveguide with a bending radius of 200um is lower than 4dB/cm for both its TE and TM modes, which is comparatively low.

We have successfully developed a reliable and efficient fabrication process for on-chip echelle grating fabrication. We combined E-beam lithography and photolithography to reduce the writing time while also achieving very high writing resolution. We have also developed an ICP etching recipe for SiO_2 and Si_3N_4 etching when using Cr as the mask. Based on this etching recipe, we can achieve a very high etching selective ratio that is more than 60 and a very deep and vertical sidewall with an angle around 89.31°.

At the inversed taper part, we successfully etched a deep and vertical ridge with aspect ratio as high as 11.6 (300nm wide and 3500nm thick).

We have successfully deposited 100nm Ag on the sidewall of the echelle-grating grooves working as the reflecting mirrors for the incident light by using the E-beam deposition. Compared to other methods to fabricate the reflecting mirror such as making another Bragg grating at the end of each groove, this direct metal deposition is more efficient and works for a much wider wavelength range, which is preferred.

Finally, we have measured the output spectrum of the echelle grating we designed. The result is very similar as what the simulation predicted. Based on this first result, the spectral resolution of the echelle grating is around 2100, the adjacent-channel cross talk is about -12dB, and the free spectrum range is about 65nm. This result is very important and promising, it demonstrates that our fabrication process is right and reliable. Since it is the first echelle grating we have ever fabricated and measured, it is a very good start for optimization in the future.

According to our analysis in the simulation chapter, we have many ways to improve the spectral resolution and the cross talk such as using a higher diffraction order, smaller grating period or a larger Rowland-circle radius. We will also optimize our fabrication to achieve better experimental results, including improving the throughput.

We believe the majority of this insertion loss comes from the propagation loss. Unlike the propagation loss of -0.975dB/cm achieved before, the input and output waveguides of the echelle grating is etched 3.3um in depth (1.5um SiO_2 upper cladding, 0.3um Si_3N_4 core and 1.5um lower SiO_2 cladding) by a much more aggressive ICP

etching recipe rather than 0.3um in depth (only 0.3um Si_3N_4 core) by a much milder ICP etching recipe. There are mainly two ways to solve this problem. The first one is optimized the ICP etching recipe to get a smoother etching profile. And the second one is change the fabrication process by writing the grooves of echelle grating and the waveguides separately by EBL. In reality, the grooves of the echelle grating are the only part that needs to be etched deeply. By separating the writing, the waveguides can be etched only 300nm in depth as before, which will offers low propagation loss as demonstrated. These are the two methods that we will try to test to realize a high throughput in the near future.

In addition, as mentioned above the pattern of curved grooves will decrease its resolution during the pattern reversion. We also need to maintain the high resolution when editing the pattern in our future experiments.

Reference:

[1] J. V. Porto, S. Rolston, B. Laburthe-Tolra, C. J. Williams, and W. D. Phillips, "Quantum information with neutral atoms as qubits" Philos. T. Roy. Soc. A 361, 1808, 14171427 (2003).

[2] A. M. Marino, R. C. Pooser, V. Boyer, and P. D. Lett, "Tunable delay of Einstein-Podolsky-Rosen entanglement," Nature 457, 859862 (2009).

[3] A. I. Lvovsky, B. C. Sanders, and W. Tittel, "Optical quantum memory," Nat. Photon. 3, 706714 (2009).

[4] G. K. Brennen, I. H. Deutsch, and P. S. Jessen, "Quantum logic gates in optical lattices,"Phys. Rev. Lett. 82, 1060 (1999).

[5] I. K. Kominis, T. W. Kornack, J. C. Allred, and M. V. Romalis, "A subfemtotesla multichannel atomic magnetometer," Nature 422, 596599 (2003).

[6] A. D. Slepkov, A. R. Bhagwat, V. Venkataraman, P. Londero, and A. L. Gaeta, "Spectroscopy of Rb atoms in hollow-core fibers," Phys. Rev. A **81**, 053825 (2010).

[7] K. Saha, V. Venkataraman, P. Londero, and A. L. Gaeta, "Enhanced two-photon absorption in a hollow- core photonic-band-gap fiber," Phys. Rev. A 83, 033833 (2011).

[8] W. Yang, D. B. Conkey, B. Wu, D. Yin, A. R. Hawkins, and H. Schmidt, "Atomic spectroscopy on a chip," Nat. Photon. 1, 331335 (2007).

[9] B. Wu, J. F. Hulbert, E. J. Lunt, K. Hurd, A. R. Hawkins, and H. Schmidt, "Slow light on a chip via atomic quantum state control," Nat. Photon. 4, 776779 (2010).

[10] S. M. Spillane, G. S. Pati, K. Salit, M. Hall, P. Kumar, R.G. Beausoleil, and M. S. Shahriar, "Observation of nonlinear optical interactions of ultralow levels of light in a

tapered optical nanofiber embedded in a hot ru- bidium vapor," Phys. Rev. Lett. 100, 233602 (2008).

[11] S. Hendrickson, M. Lai, T. Pittman, and J. Franson, "Observation of two-photon absorption at low power levels using tapered optical fibers in rubidium vapor," Phys. Rev. Lett. 105, 173602 (2010).

[12] L. Stern, B. Desiatov, I. Goykhman, and U. Levy, "Nanoscale light-matter interactions in atomic cladding waveguides," Nature Communications 4, 1548 (2013).

[13]M. Kohnen, M. Succo, P. G. Petrov, R. A. Nyman, M. Trupke, and E. A. Hinds "An array of integrated atom- photon junctions," Nature Photonics 5, 3538 (2011)

[14] M. Bajcsy, S. Hofferberth, V. Balic, T. Peyronel, M. Hafezi, A. S. Zibrov, V. Vuletic, and M. D. Lukin. "Efficient all-optical switching using slow light within a hollow fiber," Phys. Rev. Lett. **102**, 203902 (2009)

[15] E. Vetsch, D. Reitz, G Sagúe, R. Schmidt, S. T. Dawkins, and A. Rauschenbeutel, "Optical Inter- face Created by Laser-Cooled Atoms Trapped in the Evanescent Field Surrounding an Optical Nanofiber," Phys. Rev. Lett. **104**, 203603 (2010).

[16] J. Lee, J. A. Grover, J. E. Hoffman, L. A. Orozco, and R.L. Rolston, "Inhomogeneous broadening of optical transitions of ^{87}Rb atoms in an optical nanofiber trap," J. Phys. B: At. Mol. Opt. Phys. **48** 165004 (2015).

[17] J. D. Thompson, T. G. Tiecke, N. P. de Leon, J. Feist, A. V. Akimov, M. Gullans, A. S. Zibrov, V. Vuletić, and M. D. Lukin, "Coupling a Single Trapped Atom to a Nanoscale Optical Cavity," Science **340**, no. 6137, pp. 1202-1205 (2013).

[18] A. Goban, C.-L. Hung, S.-P. Yu, J. D. Hood, J. A. Muniz, J.H. Lee, M. J. Martin, A. C. McClung, K. S. Choi, D. E. Chang, O. Painter, and H. J. Kimble, "Atom- light

interactions in photonic crystals," Nat. Commun. **5**:3808 doi: 10.1038/ncomms4808 (2014).

[19] V. R. Almeida, R. R. Panepucci, and M. Lipson, "Nanotaper for compact mode conversion", Opt. Lett. 28, 15 (2003)

[20] Christopher J. Foot, Atomic Physics, Oxford University Press

[21] Y. Meng, J. Lee, M. Dagenais, and S. L. Rolston, "A nanowaveguide platform for collective atom-light interaction", Applied Physics Letters 107, 091110 (2015)

[22] J. Bland-Hawthorn, P. Kern, "Molding the flow of light: Photonics in astronomy", Physics Today, 65, 5, 31 (2012)

[23] M. Colless et al., "The 2dF Galaxy Redshift Survey: spectra and redshifts", Mon. Not. R. Astron. Soc. 328, 1039 (2001)

[24] D. J. Eisenstein et al., "Detection of the Baryon Acoustic Peak in the Large-Scale Correlation Function of SDSS Luminous Red Galaxies", Astrophys. J. 633, 560 (2005)

[25] S. M. Croom et al., "The Sydney-AAO multi-object integral field spectrograph" Mon. Not. R. Astron. Soc. 421, 872 (2012)

[26] T. A. Birks, I. Gris-Sanchez, et al., "The photonic lantern", Advances in Optics and Photonics 7, 107-167 (2015)

[27] S. G. Leon-Saval, A. Argyros, J. Bland-Hawthorn, "Photonic Lantern: a strudy of light propagation in multimode to single-mode converters", Optics Express 18, 8, 8430 – 8439 (2010)

[28] S. G. Leon-Saval, T. A. Birks, et al., "Splice-free interfacing of photonic crystal fibers", Optics Letters 30, 13, 1629 - 1631 (2005)

[29] D. Noordegraaf, P. M. W. Skovgaard, M. D. Nielsen, and J. Bland-Hawthorn, "Efficient multi-mode to singlemode coupling in a photonic lantern," Opt. Express 17(3), 1988–1994 (2009)

[30] S. G. Leon-Saval, T. A. Birks, J. Bland-Hawthorn, and M. Englund, "Multimode fiber devices with single-mode performance," Opt. Lett. 30(19), 2545–2547 (2005)

[31] R. R. Thomson, T. A. Birks, S. G. Leon-Saval, A. A. Kar, and J. Bland-Hawthorn, "Ultrafast laser inscription of an integrated photonic lantern", Optics Express 19, 6, 5698 – 5705 (2011)

[32] J. Bland-Hawthorn, P. Kern, "Astrophotonics: a new era for astronomical instruments", Optics Express 17, 3, 1880 – 1884 (2009)